ABSTRACT

Title of dissertation: COMPUTATIONAL AND ANALYTICAL INVESTIGATIONS OF DISORDERED AND INTERACTING SYSTEMS

John C. Biddle, Doctor of Philosophy, 2013

Dissertation directed by: Professor Sankar Das Sarma
Department of Physics

Localization of particle wavefunctions in quasi-disordered one dimensional incommensurate lattices is studied both numerically and analytically. Through exact diagonalization, we show that energy dependent mobility edges can appear in the case of shallow lattices. We also show that these mobility edges can be studied with a tight-binding model (an extension of the Aubry-André model) that has energy dependent mobility edges that can be determined analytically.

Topological aspects of the Aubry-André/Harper model are also studied by numerically calculating the Chern number. We first verify arguments by numerical calculations that variations in the Chern density decrease with increasing system size when the potential is incommensurate with the lattice. Next we introduce random disorder into the model and study the Chern number and the Chern density as a function of disorder strength by using the non-commutative Brillouin zone. We show that variations of the Chern density take on the same trends for both commensurate and incommensurate potentials after some critical disorder strength is reached.

Strongly correlated quantum Hall states are also examined. We numerically examine the entanglement entropy and the entanglement spectrum of fractional quantum hall states as a function of the finite layer thickness d of the quasi-two-dimensional system for a number of filling fractions ν in the lowest and the second Landau levels: $\nu = 1/3$, $7/3$, $1/2$, and $5/2$. We observe that the entanglement measures are dependent on which Landau level the electrons fractionally occupy and are completely consistent with the results based on wavefunction overlap calculations. We also compare the ground state energies by variational Monte Carlo of the spin unpolarized Halperin 331 and the spin polarized Moore-Read (MR) Pfaffian fractional quantum Hall states at half filling of the lowest Landau level (LLL) and the second Landau level (SLL) as a function of small deviations around the Coulomb point. Our results suggest that even under moderate deviations in the interaction potential the MR Pfaffian description is more energetically favorable than the Halperin 331 state in the half filled SLL (i.e. $\nu = 5/2$), consistent with recent experimental investigations.

COMPUTATIONAL AND ANALYTICAL INVESTIGATIONS OF DISORDERED AND INTERACTING SYSTEMS

by

John C. Biddle

Dissertation submitted to the Faculty of the Graduate School of the
University of Maryland, College Park in partial fulfillment
of the requirements for the degree of
Doctor of Philosophy
2013

Advisory Committee:
Professor Sankar Das Sarma, Chair/Advisor
Professor Christopher Jarzynski,
Professor Sylvester J. Gates Jr.,
Assistant Professor Michael Levin,
Professor Steven Rolston.

Dedication

To my mother, Jacqueline.

Acknowledgments

First and foremost I'd like to thank my advisor, Professor Sankar Das Sarma for his guidance and support, and for allowing me the opportunity to work with him and his impressive group. Also I especially want to thank my collaborators, Michael R. Peterson, Donald J. Priour Jr., and Bin Wang for sharing their knowledge and for their contributions to this work. I am also gracious to the members of the CMTC group for their help and advise in my time here as a student. I would also like to thank Janet Das Sarma and Jane Hessing for their administrative support.

Thanks are due to Professor Jim Gates, Professor Steven Rolston, Professor Christopher Jarzynski, and Assistant Professor Michael Levin for agreeing to serve on my thesis committee and for helping me review the manuscript.

I would also like to recognize the Kavli Institute for Theoretical Physics for inviting me to their campus as a graduate fellow in 2010 where I learned a great deal from the experience.

I am very grateful to many friends, family and coworkers for their support. I want to especially thank Bohdan Balko, David Heberlein, Melanie Stegman, Larissa Jennings, Kendrick Sadler, Isaac Chappell II, Shelley Cazares, and Rebecca Grier for their advise and encouragement in my time at Maryland as a graduate student.

I also would like to acknowledge financial support from the Institute for Defense Analyses.

Table of Contents

List of Tables

List of Figures

Chapter 1

Introduction

If the effects of disorder and electron-electron interactions can be neglected, then the transport of electrons through various media is well described by the framework introduced by Bloch almost a century ago [1]. The "Bloch wave" as it's commonly referred to[2, 3], is an extensive state (i.e. covering the entire span of the sample in question) that describes the wavefunction of an electron in a periodic potential as the product of a plane wave and a periodic function (i.e. $\psi_{n\boldsymbol{k}}(\boldsymbol{r}) = \exp(i\boldsymbol{k}\cdot\boldsymbol{r})u_{n\boldsymbol{k}}(\boldsymbol{r})$ where $u_{n\boldsymbol{k}}(\boldsymbol{r})$ reflects the periodicity of the medium). Additionally, Bloch waves associate each state with a "crystal momentum," $\boldsymbol{p}_k = \hbar\boldsymbol{k}$, and a "band index", n, that parametrize the single particle eigenspectrum, allowing the system to be studied in the context of "energy bands" where the energy is a continuous function of $\boldsymbol{k}$ within the bands. This framework has proven to be very powerful in describing the electronic properties of materials and provides the foundation of the vast majority of studies in solid-state physics[2, 3].

Of course, the effects of disorder and electron-electron interactions complicates the relatively simple picture provided by Bloch theory[4, 5, 2, 3]. In some cases, these effects can be appropriately handled within the framework of perturbation theory (e.g. Fermi liquid theory is a notable example[6]). However there are several interesting cases where Bloch theory fails or must be altered in remarkable ways. In a one

dimensional system, for example, the presence of *any* random disorder, no matter how small, has been shown to "localize" *all* electronic wavefunctions[7, 8, 9]. Coherent backscattering from impurities effectively trap electrons into small, localized regions in the medium, leading to suppressed transport. This effect is a particular example of "Anderson localization" and is one of the key mechanisms behind metal-insulator transitions[7]. Another remarkable deviation from Bloch theory occurs when a two dimensional gas of electrons are subjected to a perpendicular magnetic field. In some cases, the introduction of the magnetic field leads to non-trivial topological structure in the Bloch bands that can be described by topological invariants called "Chern" numbers[10, 11]. Since these Chern numbers are necessarily integers that lead to the quantization of the conductance for completely filled bands, this effect is often referred to as the integer quantum Hall effect (IQHE). Also for strong enough magnetic fields in systems near absolute zero, the electronic kinetic energy is effectively frozen and the dynamics are fully determined by electron-electron interactions. Thus the system is strongly correlated and as a result, Bloch theory can not provide a suitable starting point since we can not turn off the interaction. This problem is often referred to as the fractional quantum Hall effect and has very remarkable properties such as quasi-particle excitations with fractional charges and anyonic braiding statistics[12, 13, 14, 15, 16].

In this thesis, we focus on the effects of disorder and electron-electron interactions on electronic wavefunctions. In particular we study problems in Anderson localization and the quantum Hall effect. For the former, our studies are largely motivated by recent advances in manipulating cold atoms in optical lattices[17, 18, 19].

Although Anderson localization was introduced decades ago, it has been difficult to directly observe experimentally due to the lack of controllable parameters for disorder in typical solid state systems. But cold atoms provide a potential "quantum simulator" that will allow us to examine many interesting aspects of Anderson localization directly. In the quantum Hall effect, the exotic topological order that electrons arrange in may result in quasi-particle excitations with non-Abelian anyonic excitations [20, 21, 22] that may prove to be the building blocks of a so-called "topological" quantum computer[23, 24]. In this chapter, we provide some basic background on these two phenomena and outline the studies presented in this thesis.

1.1 Anderson Localization

Before Anderson's seminal work in 1958[7], the effect of disorder on electronic wavefunctions in periodic crystals was often treated as a perturbation about extended Bloch waves. Prior to this work, impurity scattering and its effect on dissipation was not well understood where it was expected that the electronic wavefunctions would still extend across the whole sample for any finite amount of disorder. Anderson, however, in his seminal work showed that for disorder strength above a critical value, particles become trapped in small, localized regions within the crystal. The envelope of such localized electronic wavefunction, $\psi(r)$, fell off exponentially with distance, (i.e. $|\psi(r)| \sim \exp(|r - r_0| / \xi)$ where ξ is the localization length). This localization of particle wavefunctions significantly suppresses transport through the

crystal, resulting in a insulating phase. This phenomena is commonly referred to as "Anderson localization" and is one of the key mechanisms behind metal-insulator transitions in weakly interacting systems. In this section, we provide a brief introduction to Anderson localization. More thorough reviews can be found in Refs. [25, 26, 27].

A qualitative understanding of Anderson's original argument for localized wavefunctions can be obtained by considering the limit of very strong disorder where the potential can be approximated by a series of potential wells with random depths. If we consider an initial bound state within one of the potential wells, tunneling to other wells is suppressed since the adjoining bound states differ considerably in energy due to the randomness. Thus, we can argue that transport (i.e. quantum diffusion) is suppressed in this limit and the eigenstates are exponentially localized. An alternative argument can be made by considering the sum of all paths for a particle propagating through a disordered medium. In the case of zero magnetic field and no magnetic impurities (i.e. time reversal invariant), paths that begin and end in the same place constructively interfere with their time reversed counterparts. Thus the particle can be effectively localized due to coherent backscattering where the probability the particle returns to where it started is enhanced.

1.1.1 Scaling Theory

A theory of localization and metal-insulator transitions in disordered systems was introduced in 1979 by Abrahams, Anderson, Licciardello, and Ramakrishnan

(the so-called "gang of four"). Their "scaling theory of localization"[28] expands on work by Thouless, Mott, Wegner, and others[29, 30, 31, 32] concerning the conductance of a system and how it changes with system size. In particular, Thouless introduced the dimensionless conductance, $g = G/(e^2/\hbar)$ and argued that at some characteristic length scale (i.e. the mean free path, l, for an extended system or the localization length, ξ, for a localized system), the conductance, g_0, is a microscopic measure of disorder. Thouless also argued that the conductance, g, of a hypercube sample of size $(2L)^d$ is a function of the conductance for a smaller L^d sample. Thus the scaling of g with L^d is a function of g_0. To complete these arguments, the gang of four introduced a universal scaling function, $\beta(g)$, that, they argue, is a function of g only:

$$\beta(g) = \frac{d\ln(g)}{d\ln(L)}. \tag{1.1}$$

The β function describes how g scales with system size, L, so negative values for β imply that the system is localized.

A qualitative understanding of how $\beta(g)$ behaves with g can be obtained by studying the expected asymptotic forms in the limit of strong and weak disorder. In the limit of no disorder, the conductance is expected to scale according to Ohm's law for $L \gg l$:

$$g(L) \sim \sigma L^{(d-2)}, \tag{1.2}$$

where σ is the conductivity. Thus, $\beta(g)$ is a constant:

$$\beta(g) = (d-2). \tag{1.3}$$

When the effect of weak disorder is included, it can be shown through diagrammatic

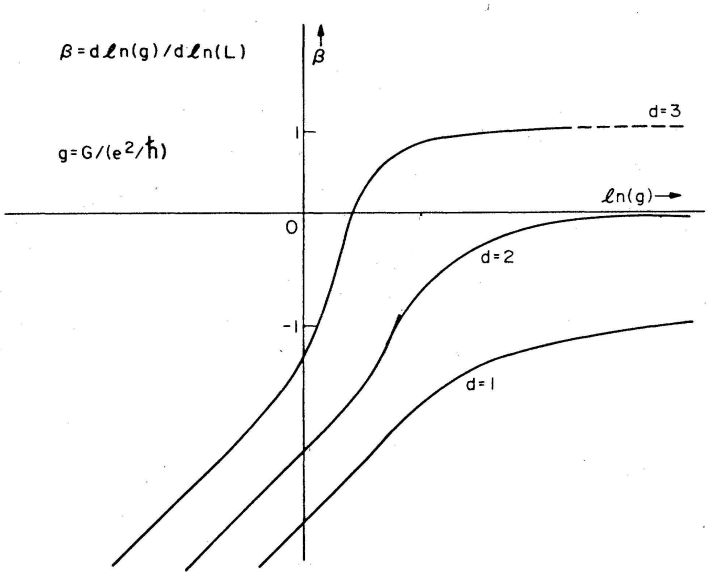

Figure 1.1: Schematic drawing of $\beta(g)$ as a function of system size ($\ln(L)$) for 1,2 and 3 dimensions. From Ref. [25].

perturbation theory that there is a $1/g$ correction in $\beta(g)$[25]. In other words, $\beta(g)$ in weak (but finite) disorder with large g behaves as

$$\beta(g) = (d-2) - a/g. \tag{1.4}$$

where $a = \pi^{-2}$ for an electron gas. Therefore, $\beta(g)$ is always less than what is expected from Ohm's law. In the limit of strong disorder, we expect the states to be localized and the conductance to fall exponentially with $L \gg \xi$:

$$g(L) \propto \exp(-L/\xi). \tag{1.5}$$

In this case, $\beta(g)$ is given by

$$\beta(g) \sim \ln(g/g_c), \tag{1.6}$$

where $g_c \gg g$ is a characteristic conductance that, generally, divides the two regimes. Assuming that $\beta(g)$ is continuous and monotonic, a qualitative interpolation between the two forms above is shown in Fig. 1.1. From the figure, we can draw

several conclusions about localization in disordered systems. 1) In one-dimensional systems, $\beta(g)$ is always negative. Therefore, all 1D systems are localized for any non-zero amount of disorder. This conclusion was also reached in earlier studies by Mott and Towse [8] and Borland [9]. 2) In three dimensions, a system can be either localized or extended. Thus there is a metal-insulator transition between the limits of small and large disorder. 3) In the case of two dimensions, all states are localized at but, in practice, the localization length is exponentially large in inverse disorder strength, so finite systems would appear to be metallic even at $T = 0$ if the disorder is weak since the localization length would be larger than the system size. In general when interactions are included, the situation is unclear in any dimensionality (except in one dimension), but most believe that the noninteracting conclusions still apply whether or not a metal-insulator transition exist in this case.

1.1.2 Quasi-Disordered Systems

Up to this point, we have assumed that the disordered potentials are purely random (i.e. uncorrelated at all relevant length scales). But similar arguments can be made for any "quasi-disordered" potential that 1) breaks (discrete) translational symmetry and 2) has a finite average. A deterministic example of such is the "almost periodic" incommensurate lattice potential in one dimension. A representative tight binding model of this potential (also called the Aubry-André model[33]) is given by

$$Eu_n = t(u_{n-1} + u_{n+1}) + v\cos(2\pi\alpha n + \psi)u_n, \tag{1.7}$$

where α is an irrational number. Similar to the case of random disorder, this potential can lead to localized eigenstates, but a notable difference is that there is a metal-insulator transition. In particular, all eigenstates are localized for $v > 2t$ and extended for $v < 2t$. This model is discussed in more detail in Chapter 2. There are also other quasi-disordered potentials with 1D metal-insulator transitions[33, 34, 35, 36]. Thus, these potentials can be thought of as an intermediate case between random and periodic potentials [37].

1.2 Cold Atoms in Optical Lattices: A Test-bed for Observing Anderson Localization

One of the main difficulties in studying condensed matter systems is that there are, in general, very few controllable parameters in typical condensed matter experiments. Direct observation of metal-insulator transitions in disordered media, for example, requires some control of the disorder strength which can be difficult to do in solid state systems (although the dimensionless strength of disorder can be varied by varying the Fermi energy in doped semiconductors by changing the density). But new, robust tools are now available to physicists that allow us to shed new light on old insights such as Anderson localization and, more generally, to explore many-body regimes that are otherwise inaccessible in solid state systems. These tools are provided to us by ultra-cold atomic systems where recent advances in their manipulation essentially provide us with "quantum simulators" that offer unprecedented control over the many-body Hamiltonian[17, 18, 19, 38]. Such systems have

allowed us to directly observe the localization of wavefunctions due to Anderson localization [39, 40], although questions remain whether what is being observed is true Anderson localization due to quantum interference induced by random disorder or just semiclassical localization (i.e. bound state formation) of the system in local potential wells.. In this section, we briefly discuss ultra-cold atomic systems and highlight recent cold atom experiments on Anderson localization.

The current capability in manipulating cold-atoms in optical lattices is thanks in large part to earlier advances in laser cooling and trapping of atoms that earned Chu, Cohen-Tannoudji, and Phillips the Nobel prize in physics in 1997[41, 42, 43]. Laser cooling via magneto-optical traps combined with evaporative cooling can lead to temperatures as low as a few nano-Kelvin[44]. At such low temperatures, the atoms can condense to form a Bose-Einstein condensate (BEC) where a large portion of atoms occupy the lowest quantum level in the system[45]. A BEC of cold atoms was first achieved by Cornell and Wieman in 1995 for which they, along with Ketterle, were awarded the Nobel prize in 2001[46, 47]. Also the spatial interference pattern of cross-propagating light fields combined with the ac Stark effect can create periodic potentials with tunable periods and depths. Thus a large class of single particle potentials can be explored by adding more laser fields[48]. Moreover, the interparticle interactions can typically be tuned using "Feshbach" resonances[49, 50]. The effect of the potential on the BEC is typically probed by irradiating the atoms with a resonant light field and imaging the fluorescent response[45].

In order to investigate Anderson localization in cold-atomic systems, several methods have been proposed to introduce disorder into the system[51]. A relatively

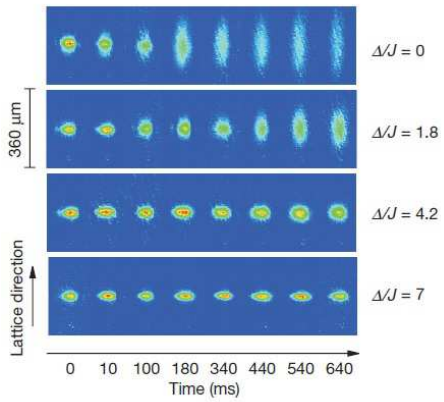

Figure 1.2: Absorption images at different moments in time of a BEC diffusing through a 1D optical incommensurate lattice after the trapping potential along that dimension is released. The degree of incommensuration is given by the ratio Δ/J. From Ref. [40].

simple method in a 1D system is to shine additional laser beams on the system to produce an incommensurate lattice, which is a realization of the Aubry-André model. This is the method implemented in a study by Roati *et al.* that is reported in Ref. [40]. A brief snapshot of their results can be seen in Fig. 1.2 which shows time of flight images of the BEC at different time intervals after the trap is released. In incommensurate potentials, all states are expected to localize when the perturbing potential strength is above a critical value. In the figure, we see that for small disorder, (i.e. Δ/J small), the BEC spreads over the length of the lattice as time progresses. For large disorder, ($\Delta/J > 7$), the BEC remains confined, signifying localization. The results by Roati *et al.* are interpreted to be the first to directly observe Anderson localization within the Aubry-André model.

1.3 The Quantum Hall Effect

The discoveries of the integer and fractional quantum Hall effect have proven to be two of the most significant findings in physics in recent years[10, 12]. In the integer quantum Hall effect, Bloch bands of single (non-interacting) electrons confined to two-dimensions in the presence of a magnetic field exhibit non-trivial topological properties with experimentally measurable consequences (i.e. the integer quantization of the Hall conductance). This effect can even be seen at room temperature in graphene[52]. In the fractional quantum Hall effect (FQHE), the unique quantum fluid that manifest in a cold two dimensional electron gas (2DEG) subjected to a perpendicular magnetic field can not be described by the well-known Landau theory of phase transitions[53]. As a result, the discovery of FQHE and the large body of research that followed helped expand our understanding of collective phenomena beyond the theory of order parameters and helped establish the concept of "topological" order. In this section, we provide a brief review of the quantum Hall effect. For a more comprehensive review, the reader is encouraged to examine Refs. [54, 55, 56]

1.3.1 Integer Quantum Hall Effect

In the classical Hall effect, the introduction of a magnetic field to a current carrying solid results in a current contribution that is perpendicular to the electric and magnetic field due to the Lorentz Force (see Fig. 1.3). This current contribution is often characterized by the Hall resistance, $R_H = R_{xy} = B/\rho e$ where ρ is the (3D)

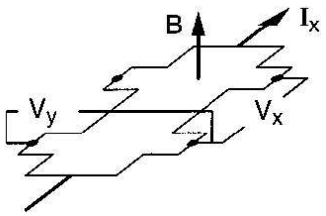

Figure 1.3: Simple schematic of a 2D "Hall" bar showing the longitudinal current, I_x, longitudinal voltage, V_x, and the Hall voltage, V_y . The longitudinal resistance is obtained from the ratio, $R_{xx} = V_x/I_x$. Similarly for the Hall resistance, $R_{xy} = V_y/I_x$.

particle density. If the current is restricted to only two dimensions (e.g. a 2DEG found in a AlAs-GaAs heterostructure or within a AlGaAs-GaAs-AlGaAs quantum well), at very low temperatures, quantum effects can dramatically change this simple picture. Some of these effects were first discovered by von Klitzing *et al.* [10] in 1980 where, for high magnetic fields ($B \sim 18T$) and low temperatures (< 2 Kelvin), the Hall resistance was found to plateau as a function of B at very precise, quantized values, regardless of the details of the sample (i.e. the quantization is universal). In particular, the Hall resistance took on the values $R_H = h/ne^2$ where n is an integer, or alternatively, the Hall conductance $\sigma_{x,y} = e^2n/h$. These plateaus would occur in the vicinity of integer values for $\nu = \rho h/Be = N_e/N_\psi$ where ρ is the (2D) particle density, N_e is the particle number, and N_ϕ is the number of magnetic flux quanta ($\phi_0 = h/e$). Also, the longitudinal resistance, R_{xx}, vanished in the $T \to 0$ limit, suggesting dissipation-less transport. This effect is commonly referred to as the integer quantum Hall effect (IQHE).

The theory behind the IQHE can be understood in the limit of free electrons and the inherent topology of Landau levels. In the presence of a magnetic field, the kinetic energy of free electrons quantizes into equally spaced (in energy) levels that

are often referred to as Landau levels. Each Landau level has a degeneracy per unit area, $G = B/\phi_0$, so given the Fermi exclusion principle, the number of filled Landau levels (ignoring spin) is $\nu = \rho\phi_0/B = N_e/N_{phi}$. Using the Kubo formula (a result of linear response theory) to calculate the Hall conductance (σ_{xy}) of filled Landau levels in the presence of a weak periodic potential, Thouless, Kohmoto, Nightingale, and den Nijs (TKNN) discovered that the Hall conductance is proportional to a topological invariant that is often referred to as the TKNN invariant[11]. The TKNN invariant is always an integer as long as the Fermi energy is within an energy gap between bands. Afterwards, it has been shown that the TKNN invariant is actually the first Chern number in the theory of fiber bundles[57] and relates to the non trivial Berry curvature in the magnetic Brillouin zone[58, 59].

1.3.2 Fractional Quantum Hall Effect

In 1982, Tsui, Stormer and Gossard repeated the von Klitzing experiment but with higher mobility 2DEG's at lower temperatures and higher magnetic fields and discovered a quantum Hall plateau corresponding to a filling fraction of $\nu = 1/3$ [12]. Subsequent experiments revealed many other fractions[60, 61, 62, 63, 64, 65, 66] (see Fig. 1.4) and the effect is often referred to as the fractional quantum Hall effect (FQHE). Unlike the integer quantum Hall effect, a free electron description of these states fails immediately because 1) the ground state of a partially filled Landau level is highly degenerate in the non-interacting limit and 2) Landau quantization freezes the kinetic energy and, as a result, the ground state is completely determined by

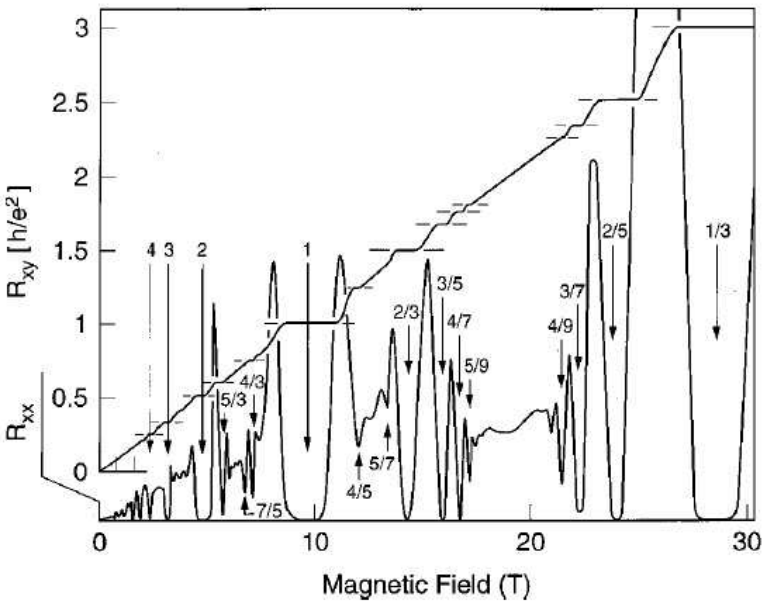

Figure 1.4: Overview of plateaus observed in the quantum Hall effect. From Refs. [67, 68]

the mutual Coulomb interactions between particles. Thus FQHE states are strongly correlated with no "small parameter."

One of the first major breakthroughs in understanding the FQHE was made by Laughlin[53] who introduced an ansatz to describe ground states observed at filling fractions $\nu = 1/m$ where m is odd. This wavefunction, which is often referred to as (not surprisingly) the "Laughlin wavefunction," is given by

$$\Psi_{\text{Laughlin}} = \prod_{j<k}^{N} (z_j - z_k)^m e^{-\sum_j |z_j|^2/4} \tag{1.8}$$

where $z = x - iy$ is the electron coordinate in the complex plane. This wavefunction has proven to be quite accurate in its description of $\nu = 1/m$ states (called the Laughlin series) and earned Laughlin the Nobel prize in 1998 (along with Tsui and Stormer)[69, 70, 71]. One of the more intriguing aspects of Laughlin's description is that the quasi-particle/quasi-hole excitations are topological entities that have

fractional local charge ($q = e/m$) and fractional braiding statistics[13]. Braiding statistics in this context refers to the theoretical concept introduced by Leinass, Myrheim and Wilczek that treats the exchange of two particles as a continuous process where the two particles "braid" around each other in the process[14, 15, 16]. In two dimensions, this process can lead to non-trivial changes to the many-body wavefunction. In the case of a Laughlin state, the braiding of two quasi-holes (quasi-particles) results in a phase change of $\exp(i\pi/m)$ to the wavefunction instead of -1 (1) for fermions (bosons). Thus, such particles are called "anyons" (i.e. "any" statistics).

The Laughlin description does not, however, describe all experimentally observed fractions in the fractional quantum Hall effect (e.g. $\nu = 2/5$). Thus, a more general framework is necessary to fully understand this effect. The most successful theory that captures most quantum Hall states, including the compressible state observed at $\nu = 1/2$, is the theory of "composite fermions" (CF)[72, 56]. Introduced by Jain this theory describes FQHE states in terms of a "composite" bound state consisting of an electron and an even number ($2p$) of vortices. These "composite fermions" are weakly interacting and, in most cases, can be treated as effectively free particles. As a result, these particles can fill so-called Λ levels which are analogous to Landau levels. Within this framework, the fractional quantum Hall effect of strongly interacting electrons turns into the integer quantum Hall effect of weakly interacting composite fermions. This line of reasoning eventually leads to the CF

wavefunctions (also called the "Jain wavefunctions") given by

$$\Psi_\nu = \mathcal{P}_{\rm LLL}\Phi_n \prod_{j<k}^{N}(z_j - z_k)^{2p} \tag{1.9}$$

for the filling factor

$$\nu = \frac{n}{2pn \pm 1} \tag{1.10}$$

for integers n and p where Φ_n is the wavefunction for n filled Landau Levels and $\mathcal{P}_{\rm LLL}$ is the projection to the lowest Landau level (LLL). The concept of weakly interacting composite fermions turns out to be very powerful and robust. For example, various experimental observations of the compressible state (i.e. no plateau) observed at $\nu = 1/2$ is consistent with the description of a Fermi sea of composite fermions (so-called "CF Fermi sea") rather than that of electrons[73]. Also some fractions (e.g. $\nu = 4/11$) could possibly be described as the fractional quantum hall effect of composite fermions[74].

1.3.3 Filling Fraction $\nu = 5/2$

An experimentally observed FQHE state that does not fall in either camp (i.e. the Laughlin or the Jain series) is the plateau observed at half filling of the second Landau level (i.e. $\nu = 2 + 1/2$ where the lowest Landau level is filled with spin up and spin down electrons). Discovered in 1987[60], this state is (so far) the only incompressible FQHE state observed that breaks the "odd denominator" rule in monolayer systems. The leading description for $\nu = 5/2$ was introduced by Moore and Read in 1991[20] who used results from conformal field theory to suggest the

following ansatz that's often referred to as the Moore-Read (MR) Pfaffian:

$$\Psi_{\mathrm{MR}} = \mathrm{Pf}\left\{\frac{1}{z_j - z_k}\right\}\prod_{j<k}^{N}(z_j - z_k)^2 e^{-\sum_j |z_j|^2/4} \tag{1.11}$$

where $\mathrm{Pf}[M_{jk}]$ is the pfaffian of the matrix M_{jk}. In the context of CF theory, the MR Pfaffian can be thought of as the p-wave pairing of composite fermions similar to Bardeen-Cooper-Schrieffer (BCS) pairing of electrons in superconductivity[75]. The remarkable aspect of the MR theory for $\nu = 5/2$ is that the quasi-hole excitations have non-Abelian anyonic braiding statistics[20, 21, 22]. In particular, $2n$ quasi-holes in the MR description at fixed locations have 2^{n-1} approximately degenerate states. The interchange of any pair of quasi-hole excitations results in a unitary rotation within the degenerate subspace and all possible rotations do not necessarily commute with each other (i.e. the braiding of quasi-holes is a non-Abelian group). Direct experimental observation of non-Abelian anyons has not yet been achieved at the time of this writing but their discovery would be a major breakthrough in our understanding of collective phenomena.

The true nature of the $\nu = 5/2$ FQHE state is one of the most prominent open questions in condensed matter physics. Recent experimental studies have explored this mysterious state and give some weight to the Moore-Read theory. One of these studies is the recent experiment by Venkatachalam *et. al.* [76] that measured the charge of localized excitations in the $\nu = 5/2$ state to be $e/4$ as predicted by the MR theory[20]. These results are consistent with previous studies by Radu *et. al.* and Dolev *et. al.* that used shot noise to investigate the local charge [77, 78, 79]. In addition to the experiments noted above, Willett *et. al.* [80, 81] have seen evidence

of quasiparticle interference oscillations that support the existence of charge $e/4$ excitations at $\nu = 5/2$. Another recent study is work performed by Bid *et. al.*[82] which experimentally observed the theorized neutral mode of the $\nu = 5/2$ state consistent with the MR theory[83, 84]. Although these developments point to the MR theory as the likely candidate for the $\nu = 5/2$ state, they are not sufficient to unambiguously establish the existence of non-Abelian anyons. Also, it should be noted that the MR theory predicts a spin polarized state at $\nu = 5/2$, but recent experimental work [85, 86] suggest that this state may be unpolarized in some cases. This aspect will be discussed in more detail in Chapter 7.

1.3.4 Topological Quantum Computing

Another motivation for verifying the existence of non-Abelain anyons is that such exotic particles may eventually become the building blocks of a fault-tolerant "topological" quantum computer [23, 24]. Quantum computing, generally speaking, is the initialization, unitary evolution, and subsequent measurement of a quantum state in order to perform a calculation[87, 88]. The advantage of using a quantum rather than a classical system is that the principles of quantum superposition and entanglement allow for a quantum computer to coherently traverse many paths in parallel while performing a calculation. This massive quantum parallelism can potentially preform many calculations significantly faster than a classical computer. The most well-known example of this is the Shor quantum algorithm[89] which can factor a prime number in polynomial time compared to the exponential time scaling

that is required by the best classical algorithms. However, one of the main hurdles in implementing a quantum computer is correcting for errors. Quantum systems can not be perfectly isolated and will couple with the environment. This coupling eventually leads to decoherence where the quantum state used for computation evolves into a mixed state (i.e. classical uncertainty is introduced). Also, systematic errors can be introduced if the unitary evolution of the state is not done perfectly. These errors can accumulate after many operations, leading to unreliable results. These errors can potentially be remedied by employing quantum error correction algorithms and introducing "quantum redundancy," but this process can, itself, introduce errors[90]. Thus the calculation can only be made fault-tolerant with quantum error correction if the basic error rate is below a certain threshold. The most optimistic estimate for this threshold is on the order of 10^{-4}, meaning that the calculation can, at most, produce a single error after performing 10^4 operations to be fault-tolerant[91].

Many of the difficulties with quantum errors described above can potentially be overcome with a quantum computer constructed with non-Abelian anyons [23, 24]. Such a topological quantum computer would operate in the Hilbert subspace consisting of the degenerate ground states and unitary evolutions in this subspace would be carried out by braiding the non-Abelian anyons. The advantage of doing this is that the degenerate subspace is topologically protected and is immune to local perturbations. As long as the temperature is much lower than the size of the energy gap, the quantum system will remain in this subspace. Systematic errors are also avoided since rotations in this subspace are not dependent on the details of

how the quasi-holes are braided (as long as the trajectories do not encircle any other quasi-holes). Thus, such a quantum computer is naturally fault-tolerant. However, in the case of the MR Pfaffian, the set of possible unitary operations that can be preformed by braiding non-Abelian anyons is not enough to perform universal quantum computation (i.e. the system can not perform any arbitrary calculation).

It should be noted that $\nu = 5/2$ is not the only fraction predicted to have non-Abelian anyons, and the fractional quantum Hall effect is not the only system that's proposed to have such exotic excitations. Fractions that fall under the Read-Rezayi series ($\nu = N + k/(Mk+2)$ for M odd and $k \geq 2$) are also predicted to have non-Abelian anyonic excitations. A notable example in this series is the $\nu = 12/5$ state, but the true nature of this state has not been settled [63, 92]. Other systems that may have non-Abelian anyons include one-dimensional nano-wires adjoining s-wave superconductors where the signature of bound Majorana modes is believed to have been seen [93], cold atomic systems with spin-orbit interactions [94], $p_x + ip_y$ superconductors [95, 96], and Josephson junctions [97].

1.4 Overview

We now provide a brief overview of the chapters that follow in this thesis.

In Chapter 2, we provide background information on the 1D Aubry-André (AA) and Harper models. We outline the derivation for the mobility edge in the AA model and show how the Harper model is related to the problem of a particle traversing a 2D lattice in the presence of a magnetic field.

In chapter 3, we study localization in the 1D AA model and in the continuous Schrödinger equation representing a particle in an incommensurate bichromatic lattice. For the latter, we find that for shallow lattices, the problem has energy-dependent mobility edges that can not be mapped to the AA model. To understand the mobility edges in the framework of a tight binding model, we consider various extensions of the AA model by including extra hopping terms and show that these extended models have energy dependent mobility edges through exact diagonalization. We also produce a model that has a duality point that can be determined analytically and we show that this model can be mapped to the Schrodinger equation for shallow lattices.

In chapter 4, we examine topological aspects of the AA/Harper models by numerically calculating the Chern number. Recently it has been shown that[98] the AA model can be associated with a topological invariant. This association is due to the incommensurate ratio which results in the Chern density being constant over the twist angles. In this chapter we first verify these arguments by numerically calculating the Chern number for commensurate and incommensurate potentials and show that variation in the Chern density decreases with increasing system size, implying that it is constant in the thermodynamic limit. Next we introduce random disorder into the model and study the Chern number and the Chern density as a function of disorder strength by using the non-commutative geometry approach introduced by Bellissard [99]. We show that variations of the Chern density take on the same trends for both commensurate and incommensurate ratios after some critical disorder strength is reached.

In chapter 5, we provide background on Landau levels in the context of the quantum Hall effect. We also discuss the quantum Hall effect in the spherical geometry, which we use exclusively in the subsequent chapters, and discuss how the Coulomb potential can be parametrized by the Haldane pseudopotentials.

In chapter 6, we theoretically examine entanglement in fractional quantum hall states, explicitly taking into account and emphasizing the quasi-two-dimensional nature of experimental quantum Hall systems. In particular, we study the entanglement entropy and the entanglement spectrum as a function of the finite layer thickness d of the quasi-two-dimensional system for a number of filling fractions ν in the lowest and the second Landau levels: $\nu = 1/3,\ 7/3,\ 1/2$, and $5/2$. We observe that the entanglement measures are dependent on which Landau level the electrons fractionally occupy, and find that filling fractions 1/3 and 7/3, which are considered to be Laughlin states, weaken with d in the lowest Landau level (ν=1/3) and strengthen with d in the second Landau level (ν=7/3). For the enigmatic even-denominator $\nu = 5/2$ state, we find that entanglement in the ground state is consistent with that of the non-Abelian Moore-Read Pfaffian state at an optimal thickness d. We also find that the single-layer $\nu = 1/2$ system is not a fractional quantum Hall state consistent with the experimental observation. In general, our theoretical findings based on entanglement considerations are completely consistent with the results based on wavefunction overlap calculations.

In chapter 7, we compare ground state energies by variational Monte Carlo of the spin unpolarized Halperin 331 and the spin polarized Moore-Read (MR) Pfaffian fractional quantum Hall states at half filling of the lowest Landau level (LLL) and

the second Landau level (SLL) as a function of small deviations around the Coulomb point via the finite thickness effect and direct alterations to the the first two Haldane pseudopotentials. In the comparison we find that in the LLL, either the 331 state or the MR Pfaffian may be lower in energy depending on the deviations. In the SLL, however, the MR Pfaffian is consistently lower in energy except for large deviations. These results suggest that even under moderate deviations in the interaction potential (through various physical process such as finite thickness, Landau level mixing, etc.), the MR Pfaffian description is more energetically favorable than the Halperin 331 state in the half filled SLL (i.e. $\nu = 5/2$), consistent with recent experimental investigations.

Chapter 2

Quasi-Disordered Crystals

As discussed in chapter 1, Anderson localization of electronic wavefunctions can be caused by "quasi-disordered" potentials as well as purely random potentials. In this chapter, we focus on a particular example of quasi-disorder, the Aubry-André (AA) model[33], which is a tight binding approximation for the incommensurate lattice potential. We also discuss a precursor to the AA model, the Harper model, which was discussed long before AA's work to examine the behavior of an electron traversing a 2D periodic potential in the presence of a uniform magnetic field. Some of these results will prove to be relevant when we study topological aspects of the model in chapter 4.

2.1 The Aubry-André model

Conditions under which Anderson localization occurs due to correlated or deterministic potentials do differ in some ways compared to that of truly random disorder. One of the more striking differences is the possibility of mobility edges in 1D systems[34, 35, 36, 37]. One of the first quasi-disordered models to show a mobility edge was introduced by Aubry and André in 1980[33] in their study of one-dimensional quasicrystals. In this model, a 1D periodic lattice with a harmonic perturbation that is incommensurate with the underlying lattice is approximated

by a tight binding model. With this model, they show that all states are localized for an incommensurate potential strength above a critical value. In this section, we will review the AA model and its main results. For further details, see the original paper by Aubry and André[33], or its subsequent reviews[37, 100] .

Consider the following tight-binding model

$$Eu_n = t(u_{n-1} + u_{n+1}) + v\cos(2\pi\alpha n + \phi)u_n, \tag{2.1}$$

where t is the nearest neighbor hopping amplitude and, $v > 0$ is the strength of the on-site potential. This system approximates an incommensurate lattice when α is an irrational number. The phase shift, ϕ is given for completeness, but is not relevant in determining localization (but will become crucial later when the hidden topological properties of the AA model are discussed). To study this model, we define localized states to be those that are normalizable in an infinite system. In other words,

$$\sum_n |u_n|^2 < \infty. \tag{2.2}$$

Thus, extended states are unnormalized states with bounded amplitudes. A simple example of such is a plane wave, $\exp(inq)$ for some q. An exponentially localized state is a state where the envelope falls off exponentially with distance. At long length scales, these states can be described as $u_n \propto \exp(-\gamma(n - n_0))$ where $\gamma \geq 0$ is the characteristic exponent (also known as the Lyaponuv exponent).

Solutions to (2.1) can be written as sums of plane waves (i.e. discrete Fourier transform)

$$u_n = e^{in\lambda}\sum_m f_m e^{im(2\pi\alpha n+\phi)}. \tag{2.3}$$

If f_m is normalizable (i.e. localized), then we expect u_n to be extended and vice versa given that α is irrational. (Note that for $\alpha = p/q$ where p and q are relatively prime, the series would have a finite set of unique terms with $f_{m+q} = f_m \exp(i\phi q)$. Thus f_m is always extensive for α irrational). Inserting (2.3) into (2.1), we see that f_m satisfies

$$\frac{v}{2}(f_{m-1} + f_{m+1}) + 2t\cos(2\pi\alpha m + \lambda)f_m = Ef_m. \tag{2.4}$$

Here we see that solving (2.1) for u_n given t and v is equivalent to solving for f_m with the roles of t and v reversed. Also we see that (2.1) and (2.4) become duals of each other when $v = 2t$ and $\phi = \lambda$. Since (2.3) transforms localized states to extended states and vice versa and solving for u_n at $v/2t$ is equivalent to solving for f_m at $v'/t' = 2t/v$, then we should expect that the states u_n are extended for $v/2t < 1$ and localized for $v/2t > 1$. Thus, the AA model has a mobility edge (i.e. a metal-insulator transition).

We can make a somewhat more rigorous argument for a mobility edge by calculating the characteristic exponent, γ. To do so, we make use of "Thouless formula" which relates the characteristic exponent to the density of states. For the state u_n at energy E satisfying (2.1), the characteristic exponent γ_1 is given by

$$\gamma_1(E) = \int dE' \ln\left|\frac{E - E'}{t}\right| \rho(E'), \tag{2.5}$$

where $\rho(E)$ is the density of states. Similarly for (2.4), the characteristic exponent, γ_2 is given by

$$\gamma_2(E) = \int dE' \ln\left|\frac{2(E - E')}{v}\right| \rho(E'). \tag{2.6}$$

Since E is not changed after the transformation (2.3), then the density of states,

$\rho(E)$, is the same for both (2.5) and (2.6). Therefore we can relate the characteristic exponent of u_n with that of f_m by the simple relation: $\gamma_1(E) = \gamma_2(E) + \ln(v/2t)$. Since $\gamma \geq 0$, if $\gamma_1(E) > 0$, then by (2.3), $\gamma_2(E) = 0$ and so $\gamma_1(E) = \ln(v/2t)$ which implies that u_n is localized for $v > 2t$. Similarly, if $\gamma_2(E) > 0$, then $\gamma_1(E) = 0$ and $\gamma_2(E) = \ln(2t/v)$ which implies that u_n is extended for $v < 2t$.

What happens when $v = 2t$? In this case, the states are neither localized nor extended, but are critical. These states are weakly localized with a power law decay and the eigenspectrum is self-similar (i.e. has fractal structure)[101].

2.2 The Harper Model

Before Aubry and André introduced their quasi-disorder model to study localization, a similar model was introduced by Harper[102] in two dimensions and later studied by Hofstadter[103] to examine the energy spectrum of an electron in two dimensions in the presence of a magnetic field. In this section, we briefly motivate this model.

Consider an electron in a two dimensional square lattice in the $x - y$ plane in the presence of a uniform magnetic field, $\mathbf{B} = B\hat{z}$. In the Landau gauge, we can use for the vector potential $\mathbf{A} = (0, Bx, 0)$ where $\nabla \times \mathbf{A} = \mathbf{B}$. Using Peierls substitution where hopping terms in the presence of a magnetic field are related to zero-field hopping terms by

$$t_{n,m} = t^{(0)}_{n,m} \exp\left(\frac{ie}{\hbar c}\int \mathbf{A}\cdot\mathbf{dl}\right), \tag{2.7}$$

where $\mathbf{dl}$ is along the link between sites n and m on the lattice, a tight binding

model for the single particle wave function, $\Psi(x, y)$, is given by

$$E\Psi(x,y) = t_x(\Psi(x+a,y) + \Psi(x-a,y)) + t_y\left(\exp\left(\frac{ie}{\hbar c}Bxa\right)\Psi(x,y+a) + \exp\left(-\frac{ie}{\hbar c}Bxa\right)\Psi(x,y-a)\right), \tag{2.8}$$

where, a is the lattice constant and t_x (t_y) is the tunneling strength between neighboring sites along the x(y)-axis. The y-coordinate is cyclic, so the solution is of the form $\Psi(x, y) = u(x)\exp(ik_y y)$. In terms of the discrete tight binding wavefunction $u_n = u(na)$ where n is an integer, we have

$$Eu_n = t_x(u_{n+1} + u_{n-1}) + 2t_y\cos(2\pi\alpha n + k_y a)u_n, \tag{2.9}$$

where $\alpha = Ba^2e/hc$. Thus α gives the number of magnetic flux quanta per plaquette in the lattice. This model is often referred to as the diagonal Harper model. Note that this is the same as Eq. (2.1) for $t = t_x$, $v = 2t_y$, and $\phi = k_y a$. Thus the problem of an electron traversing an incommensurate lattice is analogous to that of an electron traversing a square lattice with a perpendicular magnetic field.

This model was later studied by Hofstadter who showed that the eigenspectrum takes on a self-similar structure when plotted over a range of different rational values for α[103]. The structure is shown in Fig. 2.1 and is often referred to as the "Hofstadter Butterfly." Using this self-similar structure, Hofstadter was able to show that the spectrum for α irrational formed a so-called Cantor set (i.e. has measure zero in the thermodynamic limit).

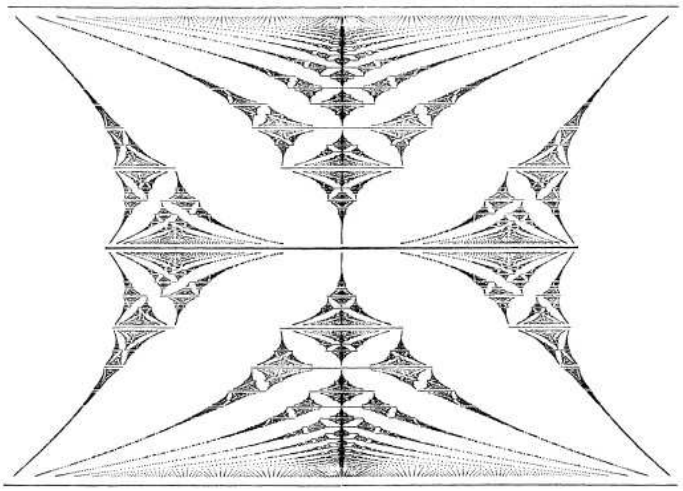

Figure 2.1: Energy spectrum as a function of α (bottom axis) of the Harper model with t fixed and $-4 < \alpha < 4$. From Ref. [103].

Chapter 3

Localization of Non-Interacting Particles in 1D Systems

In this chapter, we examine localization of non-interacting matter waves in one dimensional systems. We mostly focus on the bichromatic incommensurate lattice potential which can be studied experimentally in cold atomic systems [39]. The results presented here are published in Refs. [104, 105, 106].

3.1 Anderson Localization in a Bichromatic Lattice

One of the potentials that can be generated by laser beams to study localization in cold atomic systems is the 1D bichromatic lattice which is the addition of a primary and secondary lattice. For non-interacting particles moving along the x-axis, the Schrödinger equation with a bichromatic potential is given by

$$\left(-\frac{\hbar^2}{2m}\frac{d^2}{dx^2} + \frac{V_0}{2}\cos(2k_L x) + \frac{V_1}{2}\cos(2k_L \alpha x + \phi)\right)\psi(x) = E\psi(x). \tag{3.1}$$

where V_0 and V_1 describe the depth of the primary and secondary lattices respectively, k_L is the wave-vector of the primary lattice along the x-axis, and ϕ is an arbitrary phase. For an incommensurate system, α approximates an irrational number. When the depth of the primary lattice is sufficiently large as compared with the recoil energy $E_r \equiv (\hbar k_L)^2/2m$ as well as the depth of the secondary lattice V_1, the physical properties of the system can be studied with the single-band tight-binding Aubry-André model discussed in the previous chapter (Sec. 2.1). Thus this system

is expected to have a mobility edge as a function of the ratio of the lattice strengths, V_1/V_0. To estimate the mobility edge, we map Eq. (3.1) to the Aubry-André model by estimating $\psi(x) = \sum u_n \langle x|n\rangle$, where $|n\rangle$ is the nth Wannier state. We use the Gaussian approximation to estimate the Wannier states in the lattice. In other words, we treat the primary lattice potential as a string of independent simple Harmonic oscillators (SHO) and estimate the Wannier states as the ground states of each:

$$\langle x|n\rangle \approx \frac{\sqrt{k_L}}{\pi^{1/4}} \left(\frac{V_0}{E_r}\right)^{1/8} \exp\left(-\frac{1}{2}\sqrt{\frac{V_0}{E_r}}(k_L x)^2\right). \tag{3.2}$$

From this, we can estimate the tunneling rate, t (i.e. $\langle n\,|H_0|\,n+1\rangle$ where H_0 is given by Eq. (3.1) with $V_1 = 0$, by

$$t \approx \frac{4}{\sqrt{\pi}} E_r (\frac{V_0}{E_r})^{3/4} \exp(-2\sqrt{\frac{V_0}{E_r}}). \tag{3.3}$$

Also the incommensurate potential strength, v is approximated by

$$v \approx \langle n| \frac{V_1}{2} \cos(2k_L \alpha x) |n\rangle \approx \frac{V_1}{2} \exp(-\frac{\alpha^2}{\sqrt{V_0/E_r}}). \tag{3.4}$$

Note that v, and, therefore, the mobility edge predicted by the Aubry-André model, depends on V_1, α, and V_0/E_r.

To demonstrate localization of Eq. (3.1) for irrational α and the mapping the the AA model, we numerically solve the single-particle Schrödinger equation without any tight-binding approximation. To do so we discretize the Schrödinger equation in the position basis with a finite system size of length $L = Na$, where a is the lattice constant of the primary lattice associated with V_0. The discretized

Schroedinger equation is given by

$$\left(-\frac{\hbar^2}{2m}\right)\frac{\psi_{n+1}-2\psi_n+\psi_{n-1}}{\delta^2}+\left(V_0\cos(2k_Ln\delta)+V_1\cos(2k_L\alpha n\delta)\right)\psi_n=E\psi_n, \quad (3.5)$$

where $\delta = Na/M$ is the step interval for the discretization with M denoting the total number of steps. Then we proceed by diagonalizing the $M \times M$ matrix of the discretized Hamiltonian and study the first N eigenstates with smallest energy eigenvalues. These states would correspond to the ground band for the case with no secondary lattice (i.e. $V_1 = 0$). In our calculations for the following results, we have set $N = 500$, $M = 80,000$, and $2k_L = 1$. As our metric for localization, we use the inverse participation ratio (IPR) given by

$$IPR^{(i)} = \frac{\sum_n |u_n^{(i)}|^4}{(\sum_n |u_n^{(i)}|^2)^2} = \frac{\sum_n |\psi_n^{(i)}|^4}{(\sum_n |\psi_n^{(i)}|^2)^2}, \quad (3.6)$$

where the superscript i denote the i-th eigenstate (ordered according to energy from low to high). For spatially extended states, IPR approaches zero whereas it is finite for localized states [100]. IPR values of the first N eigenstates as a function of the secondary lattice strength V_1 are shown in Fig. 3.1 for a primary lattice strength of $V_0 = 30E_r$. In Fig. 3.1(a) the irrational ratio α is set to be the inverse golden mean, $(\sqrt{5}-1)/2$ whereas in Fig. 3.1(b), $\alpha = \pi/2$. The bold-dashed line represents the AA duality point calculated with Eqs. (3.3) and (3.4). We can see that the localization properties shown in Fig. 3.1 closely resemble the well-known results from the AA model. We do note, however, that the IPR results of Fig. 3.1 indicate a dependence on the specific value of α with $\alpha = (\sqrt{5}-1)/2$ providing a sharper AA duality than $\alpha = \pi/2$.

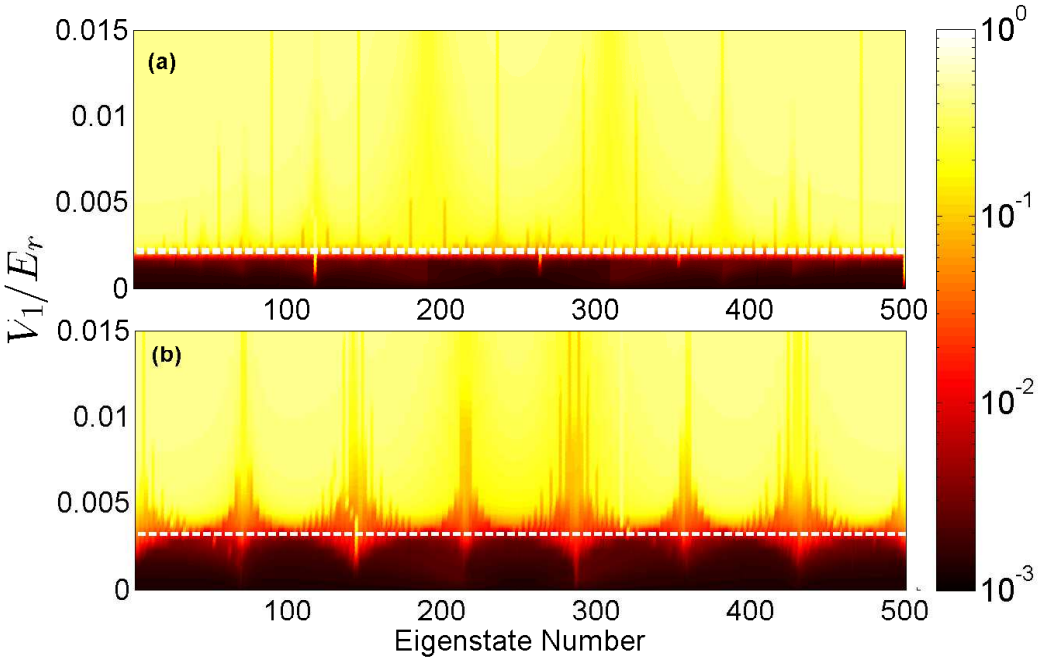

Figure 3.1: Inverse participation ratio obtained by solving the Schrödinger equation and calculated AA duality point (dashed line) at $V_0 = 30E_r$ (a) $\alpha = (\sqrt{5}-1)/2$; (b) $\alpha = \pi/2$.

In Fig. 3.2(a) we show the IPR values for the case of $V_0 = 2E_r$, a relatively shallow lattice compared to the case in Fig. 3.1, and $\alpha = (\sqrt{5}-1)/2$. In this case, the eigenstates no longer appear to localize all at once, but in discrete steps (represented by the solid lines in the figure). Also the transitions occur at fairly large values for V_1, where the secondary lattice can no longer be treated as a perturbation. We have also studied the cases where $V_0 = 2E_r$, $\alpha = \pi/2$ (Fig. 3.2(b)) and $\alpha = (\sqrt{5}+1)/2$ (not shown in the figure). In these cases no localization was observed in the eigenfunctions for any value of V_1 investigated (up to $V_1 = V_0$). This suggests that incommensurability between the lattices is not a sufficient condition to observe localization for shallow cases.

To examine the dependence of the localization transitions on α, we set $V_0 = V_1$

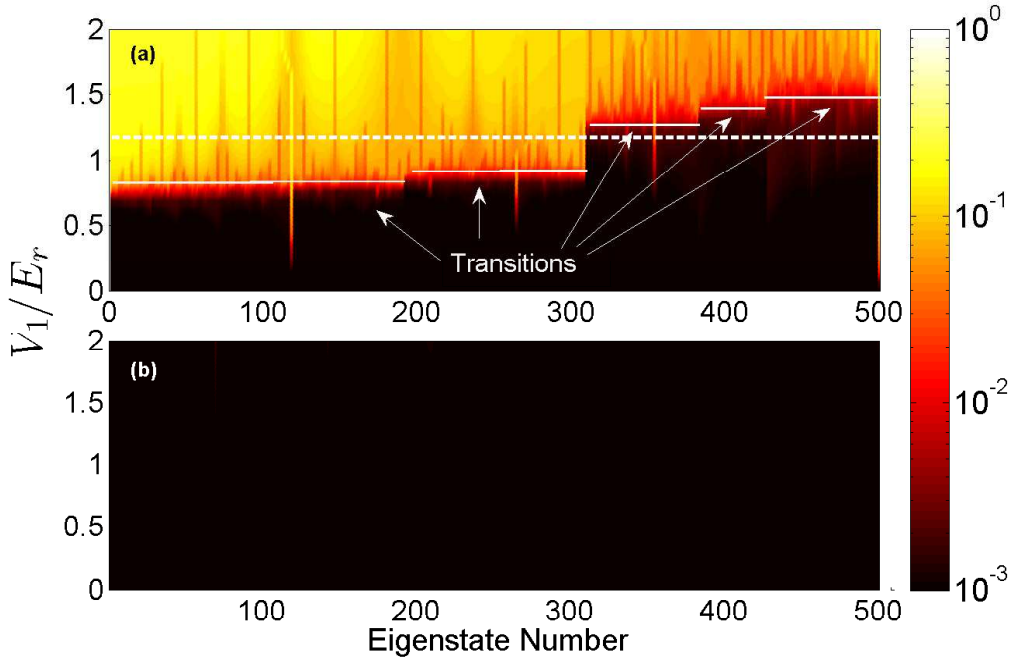

Figure 3.2: (a) Inverse participation ratio obtained by solving the Schrödinger equation and calculated AA duality point (dashed line) at $V_0 = 2E_r$ (a) $\alpha = (\sqrt{5}-1)/2$, solid lines are estimated location of localization transitions; (b) $\alpha = \pi/2$.

and calculate the IPR of the ground state for various values of V_0 and α (the values of α examined are all proportional to $(\sqrt{5}-1)/2$). These results are shown in Fig. 3.3. We see fairly distinct regions of localized and extended states, with localization tending towards areas of larger values for V_0 and smaller magnitudes for α. The curve in Fig. 3.3 represents the set of points (α,V_0) such that the AA duality point (calculated from Eqs. (3.3) and (3.4)) is equal to the lattice strength V_0. These sets of points serve as a simple heuristic estimation of the boundary between localized and extended states based on AA duality condition. Although in principle we should not expect the AA duality point obtained from Eqs. (3.3) and (3.4) to be applicable in the case of shallow lattices, this simple analytical result is in good qualitative agreement with our numerical findings.

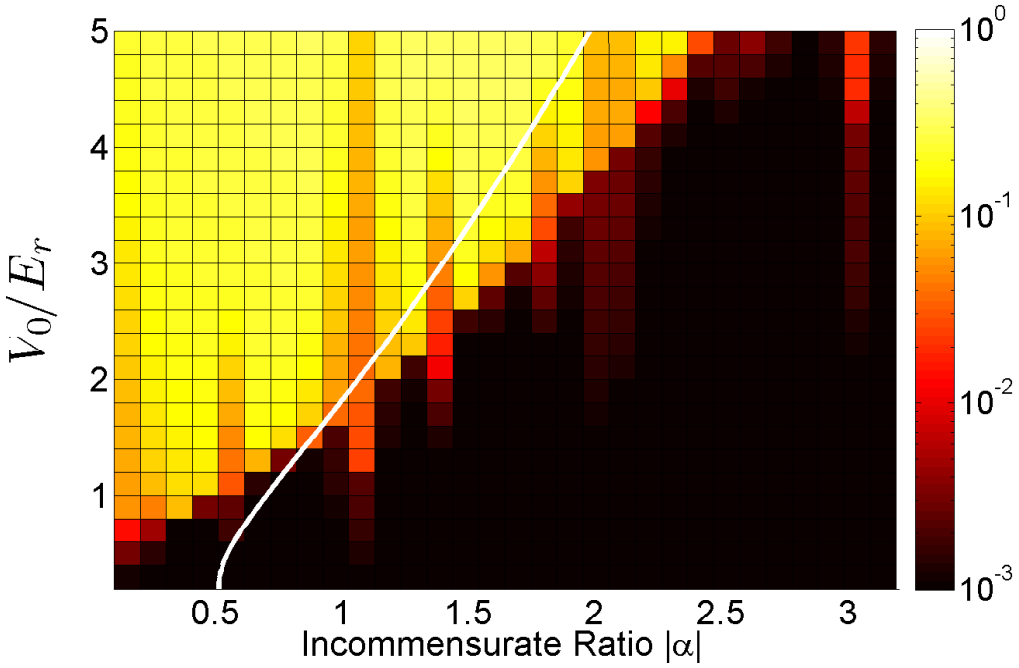

Figure 3.3: Inverse participation ratios of the ground state wavefunction for the case $V_0 = V_1$ and α equal to fractional multiples of $(\sqrt{5}-1)/2$. The solid curve represents an approximate analytical boundary between localized and extended regions based on the AA duality point.

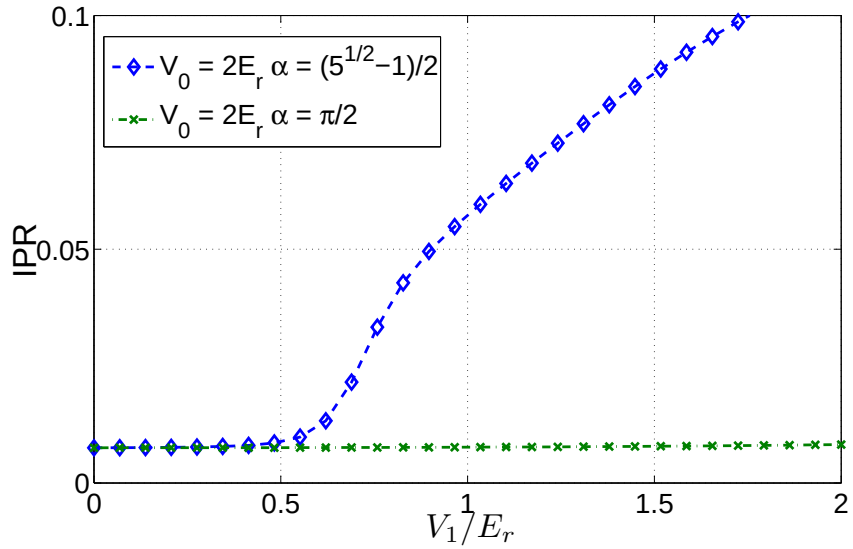

Figure 3.4: Inverse participation ratio of ground state wavefunction at time $T_0 \approx \hbar/E_r$ after the trap potential $V_{\text{trap}} = \Omega x^2$ has been turned off ($\Omega/E_r \approx 10^{-7}$).

We now briefly discuss how some of these results may be observed in cold atom experiments. We consider a diffuse BEC that is loaded into an incommensurate optical lattice, confined by a harmonic trap, $V_{trap} = \Omega x^2$. We assume that the diffuse gas is prepared in the ground state. At time $T = 0$, the harmonic trap is suddenly turned off and the BEC is allowed to diffuse. Localization can be observed by monitoring the IPR of the density wave function over time. In Fig. 3.4, we present the calculated values for the IPR as a function of V_1 for the wave function after a fixed period of time, $T_0 \approx \hbar/E_r$, has passed since the trap was turned off for the cases with $V_0 = 2E_r$, $\Omega/E_r \approx 10^{-7}$, $\alpha = (\sqrt{5}-1)/2$ and $\alpha = \pi/2$. In the figure, we see the two cases are similarly delocalized for small values of V_1. But for larger values of V_1, the IPR for the $\alpha = (\sqrt{5}-1)/2$ case begins to grow, showing increasing degree of localization, while in the $\alpha = \pi/2$ case it remains constant.

3.2 The Aubry-André model with next-nearest-neighbors hopping: the $t_1 - t_2$ model

In the previous section, we showed that even in the case of relatively shallow lattices, the AA model could qualitatively predict the mobility edge for the ground state and its dependence on the incommensuration ratio, α. However, the AA model is limited in its applicability since it can not explain the presence of energy dependent mobility edges in shallow lattices. In this section, we study a somewhat naïve extension to the AA model, by including next-nearest-neighbors (nnn) hopping. In

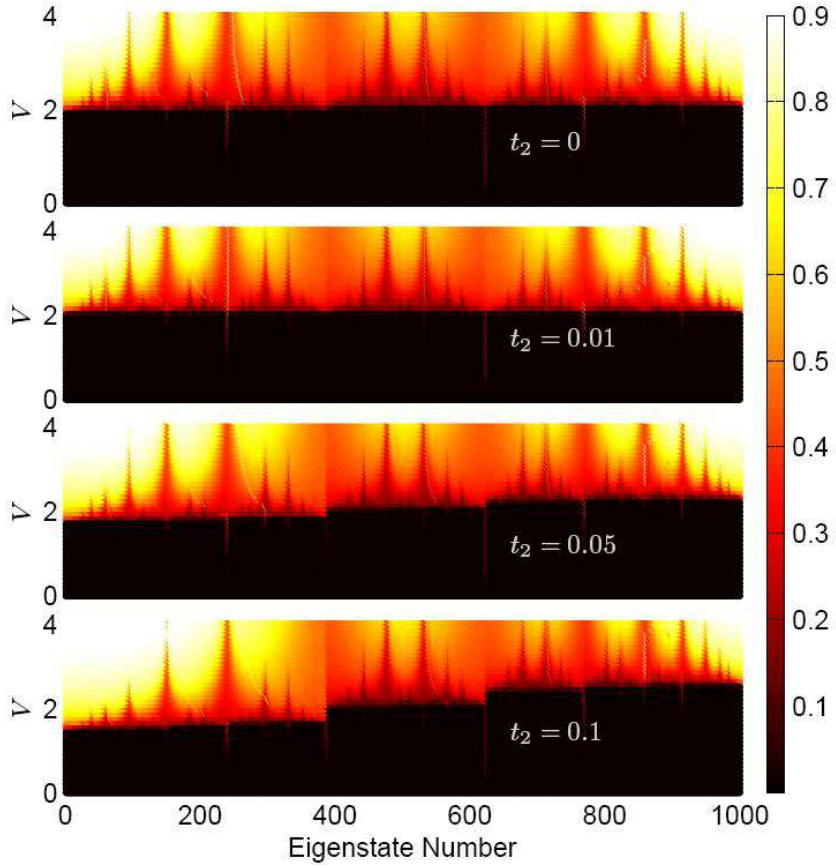

Figure 3.5: Inverse participation ratio of all eigenstates for $t_1 - t_2$ model with $\alpha = (\sqrt{5}-1)/2$. The size of the system is chosen to have 1000 sites. The four panels correspond to $t_2 = 0$, 0.01, 0.05, and 0.1 respectively. (t_1 is the unit for energy.) Darker shading corresponds to more extended states while lighter shading corresponds to more localized states.

particular, we consider the model:

$$\sum_{d=1,2} t_d(u_{n-d} + u_{n+d}) + V_n u_n = E u_n \tag{3.7}$$

where $V_n = V\cos(2\pi n)$. We solve the equation by direct diagonalization and quantify the localization of the wave function using the IPR via Eq. (3.6).

Fig. 3.5 shows the IPR values of all eigenstates as a function of the effective strength V of the secondary lattice based on the tight-binding $t_1 - t_2$ model with $\alpha = (\sqrt{5}-1)/2$ for various values of t_2 (t_1 is chosen to be unit of energy). The

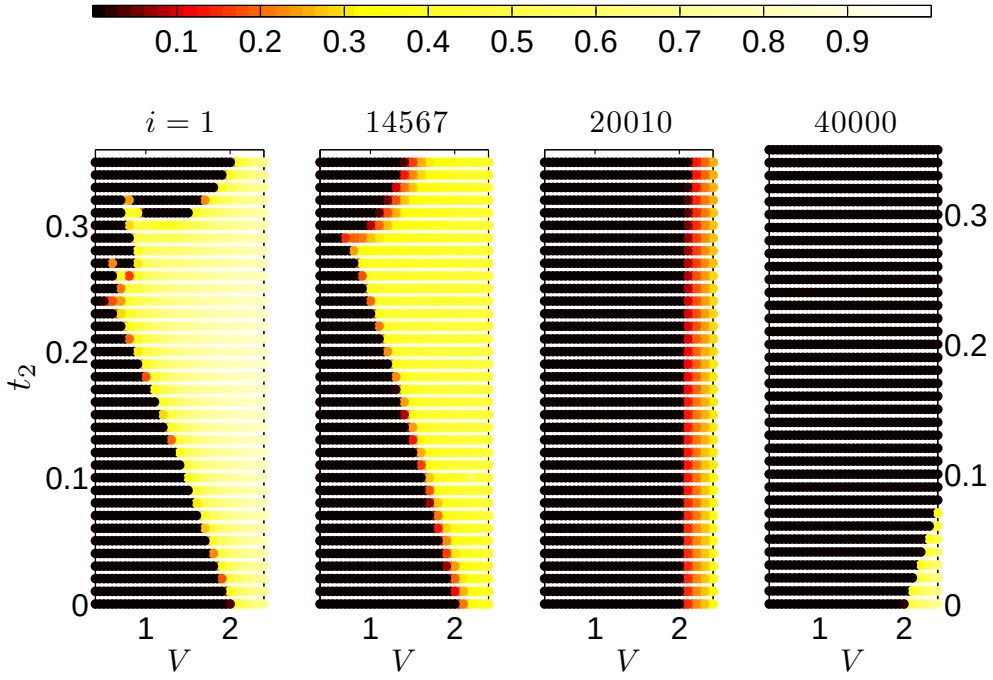

Figure 3.6: Inverse participation ratio on the $t_2 - V$ plane for $\alpha = (\sqrt{5}-1)/2$ based on the $t_1 - t_2$ model. The four panels correspond to four eigenstates labeled by i, with ascending eigenenergies. Darker regions correspond to more extended states and lighter regions correspond to more localized states.

calculation for Fig. 3.5 is done for a system with 1000 sites in the primary lattice. For small values of t_2 (e.g. $t_2 = 0.01$), the localization properties of the system have essentially the same features as those determined by the AA model. However, when $t_2 = 0.05$ or higher, AA duality is clearly destroyed and localization transitions appear to be energy dependent. For lower energies, the transition can appear for $V < 2t_1$ and for higher energies, the transition can appear for $V > 2t_1$.

In order to demonstrate the dependence of the localization transition on t_2 , we show the distribution of IPR on the $t_2 - V$ plane for four different eigenfunctions with $\alpha = (\sqrt{5}-1)/2$ in Fig. 3.6. For the calculation, the size of the system is chosen to be 40,000. At $t_2 = 0$, the $t_1 - t_2$ model reduces to the AA model, and from Fig. 3.6, one can see the sharp transition when V is increased across the duality point $V = 2$. However, the localization property of the system is greatly complicated when t_2 is finite. Besides the appearance of mobility edges, the results also reveal that the dependence of the localization property on t_2 is not monotonic, e.g. at fixed $V < 2$ when t_2 is increased the ground state could be tuned from extended to localized, but further increasing of t_2 could bring the ground state into an extended state again.

We infer from the results presented in Figs. 3.5 and 3.6 that 1) the AA duality is destroyed by having $t_2 \neq 0$; 2) instead of the $V = 2t_1$ dual point, the system has energy dependent mobility edges for $t_2 \neq 0$; 3) the precise localization condition deviates up or down from the $V = 2t_1$ AA condition depending on the energy of the eigenstate and the value of t_2. As illustrated by Figs. 3.5 and 3.6, the $t_1 - t_2$ model itself could be of interest.

However, for the study of localization properties in 1D incommensurate lattices, its validity must be dealt with caution, especially when t_2 is not sufficiently small as compared with t_1. The tight binding nn and nnn hoping integrals t_1 and t_2 can be estimated with the Wannier basis, which is fully determined by the primary lattice. One can easily estimate that when $V_0 = 3E_r$, the ratio of t_2/t_1 is on the order of 10%. To get higher t_2/t_1 ratio, one will need to tune the lattice potential shallower and should expect the tight-binding approximation to break down at some point.

3.3 Extension of the Aubry-André Model: An Exactly Solvable Model

In the previous section, we explored the localization of particle wavefunctions in cold-atomic systems with shallow lattices through numerical calculations and showed the presence of energy dependent mobility edges, in contrast to the predictions of the AA model with only nn hopping, which is expected to be relevant for deep optical lattices. We also showed that such energy dependent mobility edges might be explained by the nnn extension of the AA model although this extension breaks AA duality. In this section, we will explore a different tight binding model that has a duality point similar to the nn AA model despite having long range hopping terms but naturally predicts energy dependent mobility edges which can be analytically determined.

Consider the following tight binding model:

$$Eu_n = \sum_{n' \neq n} te^{-p|n-n'|}u_{n'} + V\cos(2\pi\alpha n + \delta)u_n, \tag{3.8}$$

where α is an irrational number and $p > 0$. This model can be thought of as a simple extension of the Aubry-André model with exponential hopping terms rather than the simple nearest neighbor. Like the AA model, this model also possesses self-duality and, thus, has a mobility edge. But we will also show that this mobility edge is necessarily energy dependent for finite p.

We begin by defining the parameter, $p_0 > 0$ such that

$$(E + t) - V\cos(2\pi\alpha n + \delta) = \Omega T_n, \tag{3.9}$$

$$T_n = \frac{\cosh(p_0) - \cos(2\pi\alpha n + \delta)}{\sinh(p_0)}, \tag{3.10}$$

$$\Omega = \sqrt{(E + t)^2 - V^2} \tag{3.11}$$

then it follows that $(E + t)/V = \cosh(p_0)$ and we can rewrite Eq. (3.8) as

$$\Omega T_n u_n = \sum_{n'} t e^{-p|n-n'|} u_{n'}. \tag{3.12}$$

If we now consider the transformation:

$$\tilde{u}_m = \sum_n e^{im(2\pi\alpha n+\delta)} T_n u_n, \tag{3.13}$$

and note that for $p > 0$ we have the identity,

$$T_n^{-1} = \sum_m e^{-p|m|} e^{im(2\pi\alpha n+\delta)}, \tag{3.14}$$

then it follows that the state, $\tilde{u}_m$ satisfies the equation:

$$\Omega \tilde{T}_m \tilde{u}_m = \sum_{m'} t e^{-p_0|m-m'|} \tilde{u}_{m'}, \tag{3.15}$$

where $\tilde{T}_m$ is given by:

$$\tilde{T}_m = \frac{\cosh(p) - \cos(2\pi\alpha m + \delta)}{\sinh(p)}. \tag{3.16}$$

We see that Eq. (3.12) is self dual under the transformation Eq. (3.13) when $p = p_0$, or equivalently $\cosh(p) = \cosh(p_0)$ for $p, p_0 > 0$. Therefore, the duality condition for Eq. (3.8) is given by:

$$\cosh(p) = \frac{E + t}{V}. \tag{3.17}$$

Thus our duality condition for this model is explicitly dependent on the energy eigenvalue, E. Moreover, if we take the limit as $p \to \infty$, we recover the AA duality point (i.e. $V = 2t$). Also note that the transformation in Eq. (3.13) is similar to the duality transformation for the AA model,Eq. (2.3). And just like Eq. (2.3), this transformation takes localized states to extended states and vice versa. Therefore we expect that the eigenstates of the system are critical (i.e. weakly localized) when Eq. (3.17) is satisfied.

Similar to the arguments made for for the AA model in the previous chapter, we now argue that the eigenstates of Eq. (3.12) are localized for $p > p_0$ and extended for $p < p_0$ (i.e. that Eq. (3.17) does, indeed, define a mobility edge). Since the Thouless formula used by Aubry and André was derived for models with nn hopping, we can not use it for our particular model. Therefore, our first step is to generalize the idea of the Thouless formula for the long-range hopping model. To do so, we treat Ω as the eigenvalue and consider the Green's matrix

$$G(\Omega)_{m,n} = (\Omega\bar{\mathrm{I}} - \overline{\mathrm{H}})^{-1}_{m,n} \tag{3.18}$$

$$= \frac{\mathrm{cofactor}(\Omega\bar{\mathrm{I}} - \overline{\mathrm{H}})_{m,n}}{\prod_\beta(\Omega - \Omega_\beta)} \tag{3.19}$$

where the cofactor is the appropriately signed determinant with the mth row and nth column removed and $\overline{\mathrm{H}}$ is the Hamiltonian corresponding to the eigenvalue

equation given in Eq. (3.12) where we have set $t = 1$ without loss of generality; $\bar{\mathrm{I}}$ is the identity matrix. Assuming a non-degenerate eigenspectrum, the Green's matrix has a simple pole for each eigenvalue, Ω_μ. Since, by definition, the residue of $G(\Omega^{(\mu)})_{m,n}$ is the product of the mth and nth elements of the eigenvector (i.e. $Res(G(\Omega)_{m,n}, \Omega_\mu) = u_m^{(\mu)} u_n^{(\mu)}$)[107], then we have for the product of the first and last elements of the eigenvector:

$$u_1^{(\mu)} u_N^{(\mu)} = \frac{\mathrm{cofactor}(\Omega_\mu \bar{\mathrm{I}} - \overline{\mathrm{H}})_{1,N}}{\prod_{\beta \neq \mu}(\Omega_\mu - \Omega_\beta)}. \tag{3.20}$$

If the state is exponentially localized about the site n', then we expect $u_n \sim \exp(-\gamma|n'-n|)$ where $\gamma \geq 0$ is the characteristic (or Lyapunov) exponent. Therefore the product $u_1 u_N \sim \exp(-\gamma(N-1))$. Thus, the characteristic exponent for large N is given by

$$\begin{aligned} \gamma(\Omega_\mu) &= \lim_{N\to\infty} -(N-1)^{-1} \ln |u_1^{(\mu)} u_N^{(\mu)}| \\ &= \lim_{N\to\infty} (N-1)^{-1} (\sum_{\beta \neq \mu} \ln |\Omega_\mu - \Omega_\beta| \\ &- \ln |\mathrm{cofactor}(\Omega_\mu \bar{\mathrm{I}} - \overline{\mathrm{H}})_{1,N}|). \end{aligned} \tag{3.21}$$

This is the generalized Thouless relation for the characteristic exponent of a wave-function. For the case where $\overline{\mathrm{H}}$ is given by Eq. (3.12), the cofactor takes on the form:

$$\mathrm{cofactor}(\Omega_\mu \bar{\mathrm{I}} - \overline{\mathrm{H}})_{1,N} = \Omega_\mu^{N-2} e^{-(N-1)p} T_N^{-1}. \tag{3.22}$$

Then we have for the characteristic exponent,

$$\gamma(\Omega_\mu) = p - \ln |\Omega_\mu| + \lim_{N\to\infty} (N-1)^{-1} \sum_{\beta \neq \mu} \ln |\Omega_\mu - \Omega_\beta|. \tag{3.23}$$

We now compare the characteristic exponents of the eigenvectors of Eq. (3.12), which we denote as $\gamma(\Omega)$, with the exponents of the dual problem Eq. (3.15), denoted as $\tilde{\gamma}(\Omega)$. Since the eigenvalue, Ω is not changed by the transformation given by Eq. (3.13), then we expect the summation term on the RHS of Eq. (3.23) to be equal for both Eq. (3.12) and Eq. (3.15). Therefore, the characteristic exponents have the following relation:

$$\gamma(\Omega) = \tilde{\gamma}(\Omega) + (p - p_0). \tag{3.24}$$

Considering the case when $p > p_0$, since $\tilde{\gamma}(\Omega) \geq 0$, then it follows that $\gamma(\Omega) > 0$ and therefore the eigenstate, u_n is localized while the dual state, $\tilde{u}_n$ is extended. Similarly, when $p_0 > p$, we can argue that $\tilde{\gamma}(\Omega) > 0$ and therefore the dual state, $\tilde{u}_n$, is localized while u_n is extended. Therefore, returning to the original problem given by Eq. (3.8) and using the fact that $\cosh(p_0)$ is a monotonically increasing function of $p_0 > 0$, then it follows that the eigenstates are localized for $(E + t)/V < \cosh(p)$ and extended for $(E + t)/V > \cosh(p)$.

The self-duality described above has a general form. Considering a model of the general form

$$\sum_m t_m u_{n+m} + V_0 v_n u_n = E u_n. \tag{3.25}$$

The model will have a similar form of self-duality if the on-site potential and the hopping terms satisfy the relation:

$$\frac{A}{B - v_n} = \sum_m t_m e^{im(2\pi\alpha n + \delta)} \tag{3.26}$$

where A and B are constants. In particular, the constant B gives the slope of the the duality condition (i.e. $B = E/V_0$).

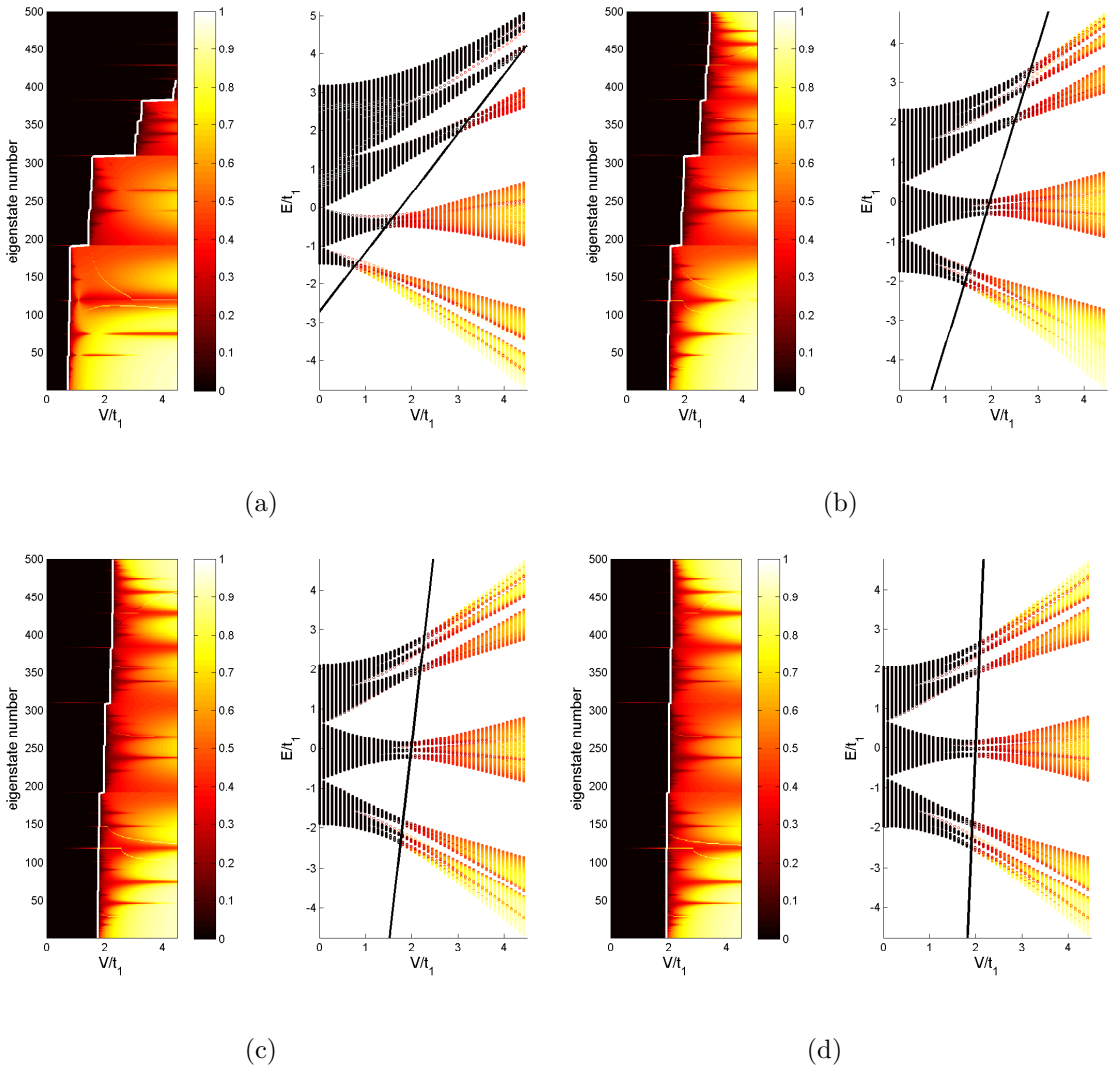

Figure 3.7: Energy eigenvalues and inverse participation ratios of Eq. (3.8) with 500 lattice sites and $\alpha = (\sqrt{5}-1)/2$ for (a) $p = 1$, (b) $p = 2$, (c) $p = 3$, (d) $p = 4$. The solid line represents the analytical boundary between spatially localized and spatially extended states.

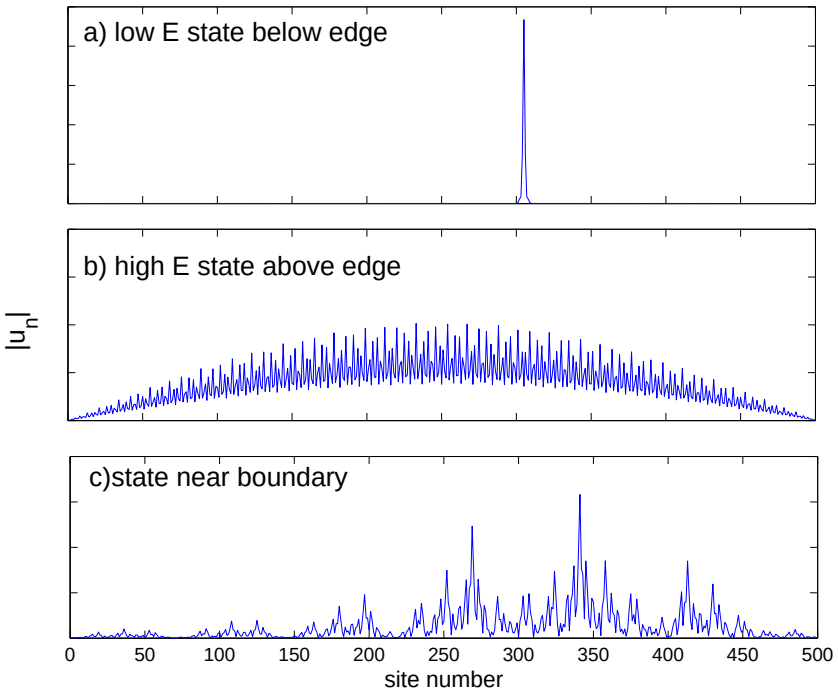

Figure 3.8: Eigenstates of Eq. (3.8) with 500 lattice sites, $\alpha = (\sqrt{5}-1)/2$, $V = 1.8$, and $p = 1.5$ for different energy eigenvalues: a) low energy localized state below the mobility edge b) high energy extended state above the mobility edge c) critical state near the mobility edge.

We now numerically examine localization in Eq. (3.8) (and equivalently Eq. (3.12)) by calculating the inverse participation ratio (IPR) of the wavefunctions (3.6) Fig. 3.7 plots energy eigenvalues (or eigenstate number) and the IPR of the corresponding wavefunctions for Eq. (3.8) as a function of potential strength, V, with $\alpha = (\sqrt{5}-1)/2$ and $p = 1$, 2, 3, or 4. The solid curves in the figures represent the boundary given in Eq. (3.17). From the figure we see that IPR values are approximately zero for energies above the boundary and are finite for energies below the boundary. This supports our assertion that the mobility edge is, indeed, given by Eq. (3.17).

In Fig. 3.8, we directly examine sample eigenstates in each regime (i.e. localized, extended and near the mobility edge) for $p = 1.5$ and $V = 1.8$. We see that the wavefunction is localized for low energies (Fig 3.8a), extended for high energies (Fig 3.8b), and critical (power law decay) near the boundary (Fig 3.8c).

We now examine the eigenvalues of Eq. (3.12) for different values of α at the duality point ($p = p_0$) where we expect the eigenspectrum to form a fractal set for large N. The results of this are given in Fig. 3.9. In the figure, we see that for large values of p, the eigenspectrum closely resembles the well known Hofstadter's butterfly which results from the solutions of Harper's equation [102, 103]. For smaller values of p, however, we see a generalized form of Hofstadter's butterfly that is not symmetrical about the the band center, but skewed towards lower eigenvalues. The self-similarity in the figure suggest that the eigenspectrum does, indeed, form a Cantor set at the duality point in the thermodynamic limit.

To understand the relevance of these results to ultra-cold atoms in optical

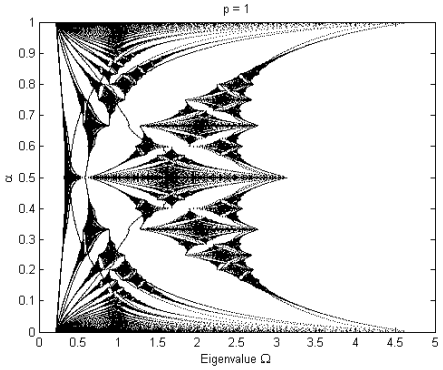

(a)

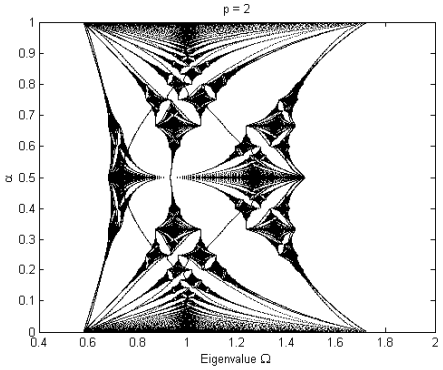

(b)

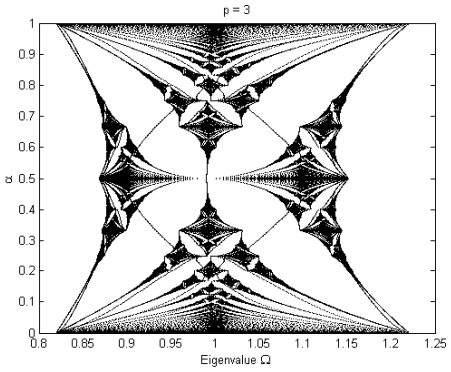

(c)

Figure 3.9: Eigenspectrum of Eq. (3.12) with varying α for (a) $p = 1$, (b) $p = 2$, and (c) $p = 3$.

lattices, we draw the connection between the implicit short-range tight binding model given in Eq. (3.8) and the fundamental single particle Schrödinger equation in (3.1). To do this, we study the ground band Wannier functions [108], $w_n(x)$ of Eq. (3.1) for $V_1 = 0$ and approximate the matrix elements of the Hamiltonian in the Wannier basis. Using the Gaussian approximation for the ground band Wannier states, the potential strength, V, in Eq. (3.8) is approximated by the expression given earlier in Eq. (3.4). Also from this approximation, we have for the constant energy difference between (3.8) and (3.1):

$$E_0 = \langle w_n|H_0|w_n\rangle \approx \frac{1}{2}(V_0 e^{-\sqrt{\frac{E_r}{V_0}}} + \sqrt{V_0 E_r}), \tag{3.27}$$

where H_0 is the Hamiltonian corresponding to (3.1) with $V_1 = 0$. The hopping coefficient, t, can be estimated using the deep lattice approximation for the ground bandwidth:

$$t \approx \frac{4}{\sqrt{\pi}} E_r (\frac{V_0}{E_r})^{3/4} \exp(-2\sqrt{\frac{V_0}{E_r}} + p). \tag{3.28}$$

To estimate the hopping overlap integrals, we make use of the results reported by Kohn on the analytical properties of Wannier functions [109]. According to Kohn, the overlap integrals have the asymptotic characteristic:

$$\langle w_n|H_0|w_n'\rangle \sim e^{-p|n-n'|}, \tag{3.29}$$

where p is the imaginary part of the branch point of $E(k)$ (k is the quasi-momentum) that connects the ground band to the first excited band in complex k-space. The parameter p can be obtained from the first stationary point, μ_0, of Kramers' function $\mu(E) = \cos(k(E)b)$ [110], where b is the period of the primary lattice, by the

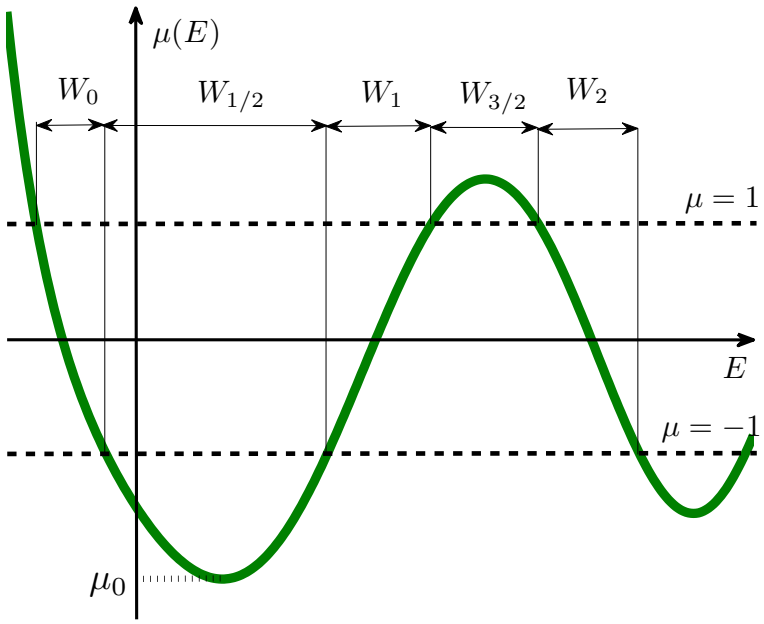

Figure 3.10: Schematic drawing of Kramers' function [110]. The energy bands correspond to $|\mu(E)| \leq 1$ and the band gaps correspond to $|\mu(E)| > 1$

expression:

$$p = |\cosh^{-1}|\mu_0||. \tag{3.30}$$

Fig. 3.10 gives a representative schematic plot of Kramer's function, $\mu(E)$. Let W_0 be the bandwidth of the ground band and let $W_{1/2}$ be the width of the first bandgap. If we use as an approximation for the ground band energy:

$$E \approx -\frac{W_0}{2}\cos(kb) + \epsilon_0, \tag{3.31}$$

where ϵ_0 is a constant, then we have as an estimate for $d\mu/dE$ at the top edge of the ground band, labeled ϵ^+:

$$\left.\frac{d\mu}{dE}\right|_{E=\epsilon^+} \approx -\frac{2}{W_0}. \tag{3.32}$$

If we approximate $\mu(E)$ as a parabola within the bandgap and use (3.32), then we obtain as an approximation for μ_0:

$$\mu_0 \approx -1 - \frac{W_{1/2}}{2W_0}. \tag{3.33}$$

The ratio $W_{1/2}/W_0$ can be estimated using properties of the Mathieu functions [111]:

$$\frac{W_{1/2}}{W_0} = \frac{\sqrt{\pi}}{8}(\frac{V_0}{E_r})^{-1/4} \exp\left(2\sqrt{\frac{V_0}{E_r}}\right). \tag{3.34}$$

Finally, using (3.30) and (3.4), the equivalent of (3.17) for the 1-D incommensurate lattice Schrödinger equation (3.1) is given by:

$$2\exp\left(\frac{\alpha^2}{\sqrt{V_0/E_r}}\right)(E - E_0 + t) = V_1\left(1 + \frac{W_{1/2}}{2W_0}\right), \tag{3.35}$$

where E_0 is estimated by (3.27). One interesting implication of (3.35) is that the sharpness of the extended/localization transition is determined by the ratio of the bandgap width to the width of the ground band. The AA condition is analogous to (3.35) when the bandgap is much larger than the width of the ground band.

To examine the accuracy of (3.35), we numerically integrate (3.1) to obtain the energy eigenvalues and wavefunctions and calculate the IPR. In our calculations, we set $k_L = 1$, $\alpha = (\sqrt{5}-1)/2$, $m = 1$. The size of the system is given by $L = Na$ where a is the lattice constant. N is chosen to be 500 and (3.1) is sampled over 80,000 points. Fig. 3.11 gives eigenstates at three different energy eigenvalues for $V_0 = 2E_r$ and $V_1 = 1.43E_r$(similar to Fig 3.8). Similar to the results in the tight binding model, we see that for a fixed potential strength an eigenstate can be localized for low energies (Fig 3.11a), extended for high energies (Fig 3.11b), and critical near the boundary (Fig 3.11c). Fig. 3.12 gives calculated IPR values as a function of

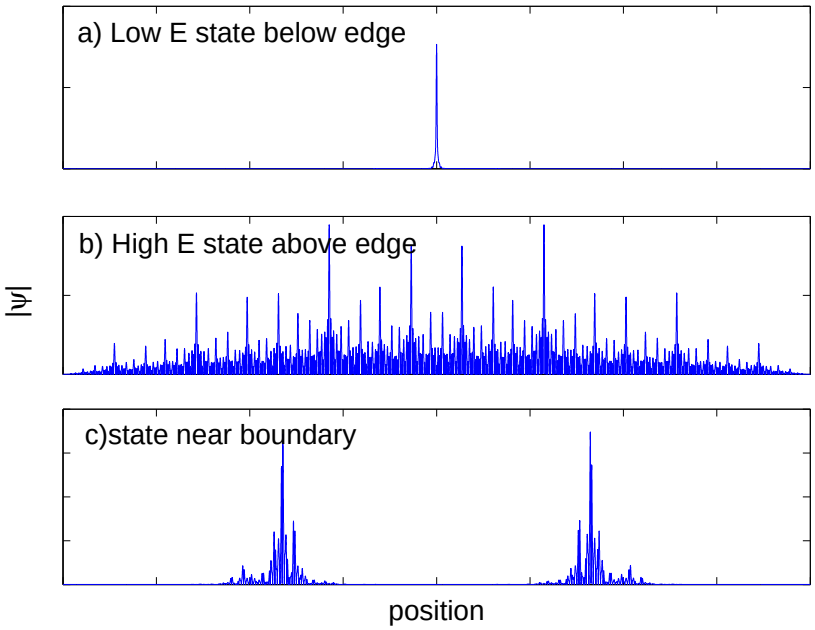

Figure 3.11: Eigenstates of (3.1) with 500 lattice sites, $\alpha = (\sqrt{5}-1)/2$, $V_0 = 2E_r$ and $V_1 = 1.43E_r$ for different energy eigenvalues: a) low energy state below mobility edge b) high energy state above mobility edge c) critical state near the predicted mobility edge.

eigenstate number and V_1 for the first N eigenstates (equivalent to the ground band when $V_1 = 0$) The solid curves gives the analytical boundary between localized and extended states as given by (3.35). We see in Fig 3.12 that our analytical prediction is in good agreement with our IPR calculations. We also note that (3.35) is dependent on incommensuration and may predict no localization transition for $\alpha^2/\sqrt{V_0/E_r} \gg 1$, where the slope of the boundary in $E - V_1$ space is essentially flat. This is consistent with numerical results reported in section 3.1 [104] where localization transitions in (3.1) are observed to be dependent on incommensuration for shallow lattices.

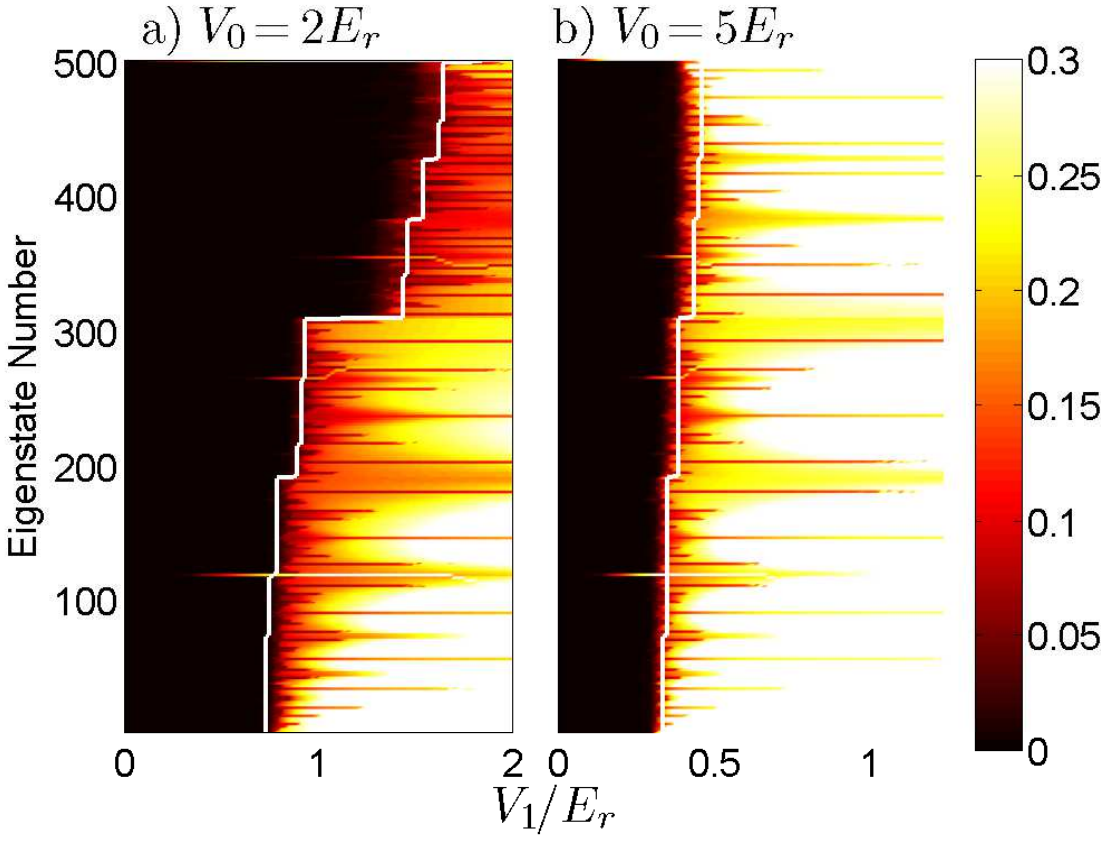

Figure 3.12: Inverse participation ratios of the approximate ground band eigenstates of (3.1) with $\alpha = (\sqrt{5}-1)/2$ for a) $V_0 = 2E_r$ and b) $V_0 = 5E_r$. The solid curves represent the analytical boundary between spatially localized and spatially extended states.

3.4 Non-dual Extensions of the Aubry-Andre Model

In the previous section, we have introduced a tight binding model that naturally predicts energy-dependent mobility edges that can be determined analytically and showed an approximate mapping to the Schrodinger equation. The mapping, however, is not perfect and it is likely that the exponentially decaying hopping model is not appropriate for all shallow lattices. With these caveats in mind, we examine alternative models where the extended hopping terms are allowed to decay either more quickly (i.e. Gaussian) or more slowly (i.e. power law). These models do not have an easily discernible duality point like that seen in Eq. (3.8) or in Eq. (2.1), but these models do show energy dependent mobility edges which can be predicted qualitatively by the condition in Eq. (3.17).

We begin by revisiting the $t_1 - t_2$ model discussed in section 3.2. We have already seen that this model gives energy-dependent mobility edges for $t_2 > 0$. Here, we will use this model to illustrate a heuristic prediction of mobility edges based on Eq. (3.17). If we consider an approximately equivalent exponential hopping model, then the parameters are given by $p = \ln(t_1/t_2)$ and $t = t_1 e^p$. Using Eq. (3.17), we can approximate the boundary between localized and extended states. To examine how well this heuristic works in practice we calculate the IPR of the eigenstates of Eq. (3.7). The results are given in Fig. 3.13 for 500 lattice sites, $\alpha = (\sqrt{5} - 1)/2$ and various values of the ratio t_2/t_1. The solid lines in the figure give the approximate mobility edge given by Eq. (3.17). From the figure, we see that for small values of t_2/t_1, the approximate boundary is in good qualitative

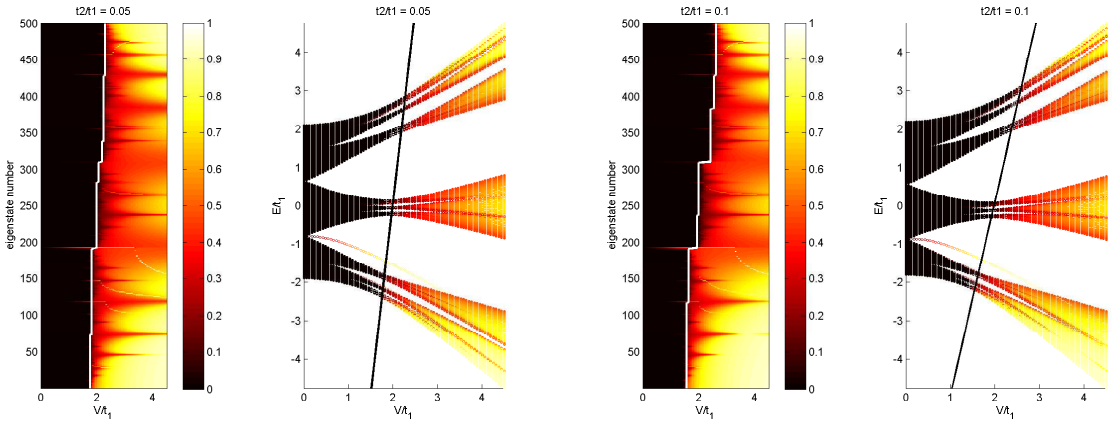

(a)

(b)

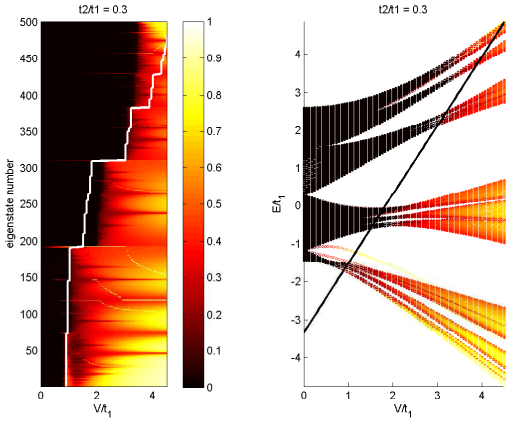

(c)

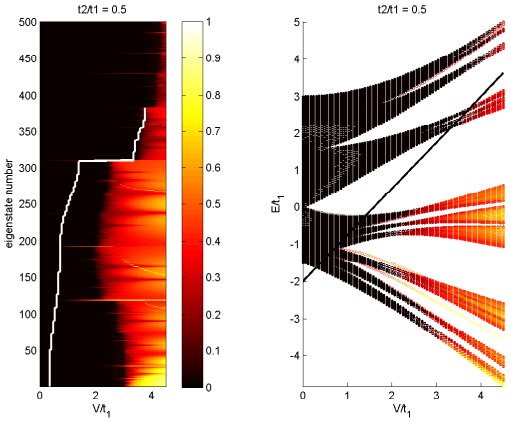

(d)

Figure 3.13: Inverse participation ratios and energy eigenvalues of all eigenstates of Eq. (3.7) with 500 lattice sites and $\alpha = (\sqrt{5}-1)/2$ for $t_2/t_1 =$ (a) 0.05, (b) 0.1, (c) 0.3, (d) 0.5. The solid curves represent the approximate boundary between spatially localized and spatially extended states.

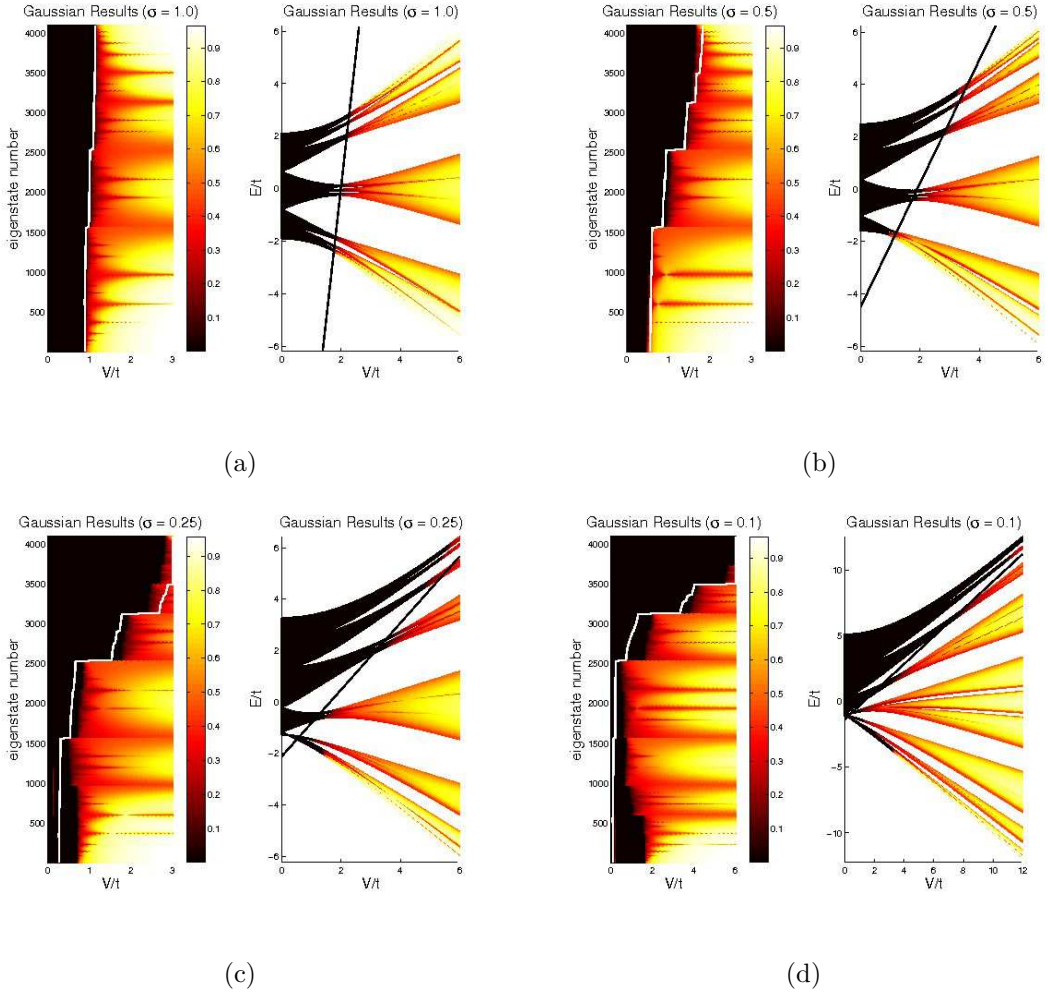

Figure 3.14: Inverse participation ratios and energy eigenvalues of all eigenstates of Eq. (3.36) with 4096 lattice sites and $\alpha = (\sqrt{5}-1)/2$ for $\sigma =$ (a) 1.0, (b) 0.5, (c) 0.25, and (d) 0.10. The solid curves represent the approximate boundary between spatially localized and spatially extended states.

agreement with the numerical IPR results. For larger values, however ($t_2/t_1 \gtrsim 0.3$) the boundary differs considerably from the linear condition in Eq. (3.17), as we might expect.

It is likely that the exponentially decaying approximation for the tunneling rate is an overestimation of the actual rate. In this case, a more appropriate model may be to assume that the tunneling rate has a Gaussian (rather than exponential) decay with distance. Such an alternative tight binding model is of the form,

$$\sum_{n' \neq n} e^{-\sigma |n-n'|^2} u_{n'} + V \cos(2\pi\alpha n + \delta) u_n = E u_n, \tag{3.36}$$

where σ describes the decay rate. Given the results on the $t_1 - t_2$ model, we expect that this model will still display energy-dependent mobility edges for large enough σ. Also, in some cases, the heuristic we applied in the $t_1 - t_2$ model will also give a qualitative prediction for the mobility edges. To determine this heuristic based on the condition given in Eq. (3.17), we estimate p from the ratio t_2/t_1, which yields $p = 3\sigma$. To examine how well the heuristic works on the Gaussian decaying hopping model, we again look at the IPR for different values of σ. The IPR results for this model are given in Fig. 3.14 (again, $\alpha = (\sqrt{5}-1)/2$ and $t_1 = 1$). In this figure, we see that the approximate boundary is in good qualitative agreement with the numerical results for larger values of σ. Small values of σ (i.e. $\sigma < 0.5$), however, do not easily fit the heuristic. Also, the mobility edges in these cases have very interesting trends. In particular, in some cases, the lower and higher energy tails have extended states while the states in the middle of the band are localized.

Finally we consider the case where the decay in the tunneling rate is relatively

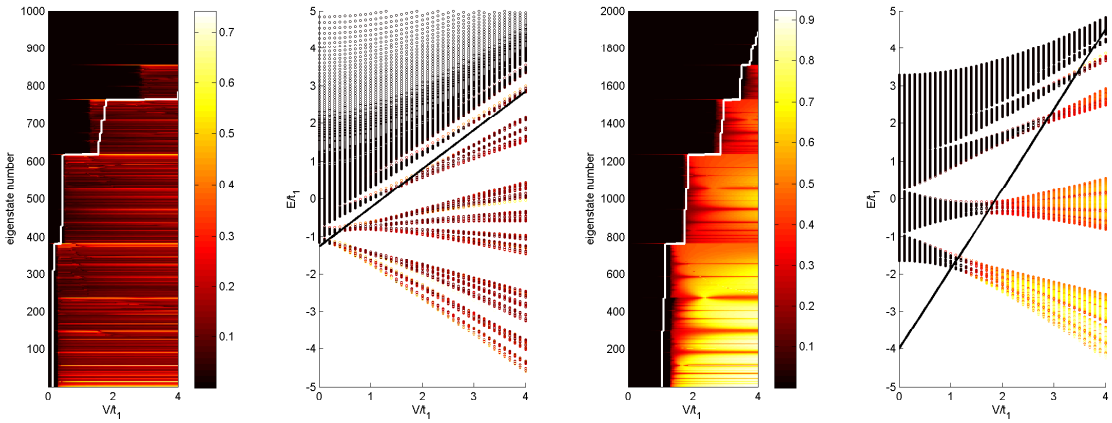

(a) $r = 1/3$

(b) $r = 2$

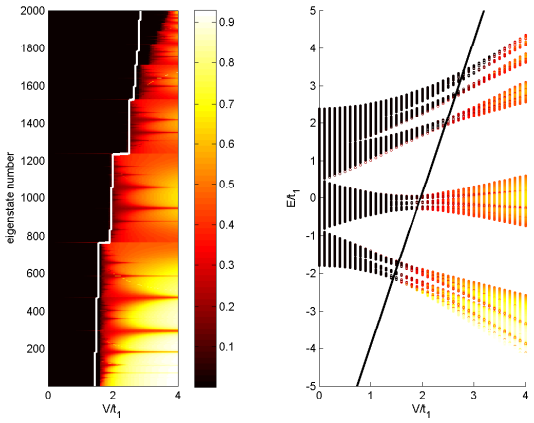

(c) $r = 3$

Figure 3.15: Inverse participation ratios and energy eigenvalues of all eigenstates of Eq. (3.37) with 2000 lattice sites and $\alpha = (\sqrt{5} - 1)/2$ for various values of r. The solid curves represent the approximate boundary between spatially localized and spatially extended states.

slow (i.e. a power low) compared to the exponential model. For power law decay in the hopping terms, we examine the model:

$$\sum_{n' \neq n} t \frac{u_{n'}}{|n - n'|^r} + V \cos(2\pi\alpha n + \delta) = E u_n. \tag{3.37}$$

In this case, the exponential coefficient, p for our heuristic prediction is given by $p = r \ln(2)$. Fig 3.15 gives IPR results for this model with $\alpha = (\sqrt{5} - 1)/2$ and $r = 1/3$ (Fig 3.15(a)), $r = 2$ (Fig 3.15(b)), and $r = 3$ (Fig 3.15(c)). In each of these cases, the approximate localization boundary is in good qualitative agreement with the numerical results.

From the numerical results above, we see that, in general, extensions of the AA model that include hopping terms beyond the nn coupling predict energy dependent mobility edges. However, the difference between the models and how the mobility edges emerge is intriguing and deserves further discussion. Suppose that there is a functional form for the critical potential strength at which an eigenstate at energy E localizes and that it is a function of E, say $V_c(E)$. Then for the exponentially decaying hopping model, this function is known (i.e. Eq. (3.17)) and varies linearly with E. In the case of the power law decay in tunneling rate, it appears that $V_c(E)$ is monotonically increasing with positive curvature ($d^2V_c/dE^2 \leq 0$). For Gaussian decay in tunneling rate, $V_c(E)$ appears to have negative curvature and is not one-to-one in some cases (i.e the inverse is multi-valued). Thus it appears that the speed with which tunneling decays with distance in the quasi-disordered tight binding models affects the curvature of $V_c(E)$ with our solvable model being the case where the curvature of $V_c(E)$ is flat (i.e. linear). Further study is necessary, however, to

verify the nature of $V_c(E)$ with respect to t_n and the type of quasi-disorder.

Chapter 4

Topological Quasi-Crystals: Chern Numbers in the Harper/Aubry-André Model

In chapter 2, we showed that the Aubry-André model is a special case of the Harper model which describes an electron in a 2D periodic potential in the presence of a perpendicular magnetic field. This mapping from 2D to an effective 1D problem has been known for quite some time [102], but some of the topological aspects of this mapping have only recently been discussed. In a recent publication, Kraus *et al.*[98] showed that through adiabatic change of the phase shift, ϕ (which we largely ignored in our localization studies), topological edge states that traverse the bulk gaps can be seen in the spectrum. Furthermore, the Aubry-André model (where α in the Harper model is irrational) is a special case where an unambiguous topological index can be assigned for all values of ϕ. In this chapter, we will briefly review the arguments by Kraus *et al.* and study the topological index (i.e. the Chern number) with respect to random disorder[112].

4.1 Background

Recall that in the derivation of the 1D Harper model in Eq. (2.9), the phase shift in the onsite harmonic potential, ϕ, is proportional to the quasi-momentum in the cyclic dimension k_y of the original 2D tight binding model. Thus, we can

say that the phase shift is an "extra-dimensional" degree of freedom that retains information from the higher dimensional (2D) model. The interesting observation made in Ref. [98] is that topological features of the 2D system (in particular, the Chern number) can be teased out from the 1D system by varying ϕ. To demonstrate this, we numerically solve (2.1) for $\alpha = (\sqrt{5}+1)/2$ (the golden mean) with varying ϕ and fixed boundary conditions. The resulting spectrum is shown in Fig. 4.1. In the eigenspectrum, we see states that traverse the bulk gaps as a function of ϕ. These states are localized on the edges of the system and are topological in nature. In particular, they signify that the bands from the 2D ancestor model have non-trivial Chern numbers. The existence of topological edge states is not contingent on irrational α, however. Such states will present themselves for any α associated with a 2D ancestor with non-trivial Chern number (e.g. $\alpha = 1/3$) . What makes the irrational case special is that a topological index can be associated with the system regardless of ϕ. We outline the argument below. For full details, see Ref. [98].

In Ref. [58], Avron *et al.* showed that the Chern number of a 2D band of single-particle states (or alternatively, a many-body state of electrons that fill a band) can be obtained by introducing twisted boundary conditions (i.e. $\Psi(x+L_x, y) = \exp(i\theta)\Psi(x,y)$ and $\Psi(x, y+L_y) = \exp(i\phi)\Psi(x,y)$). The twisted boundary conditions are equivalent to threading magnetic flux through the rings of a torus. Similar boundary conditions can be imposed on the Harper model in order to obtain the Chern number of the 2D ancestor. Consider the following altered version of the

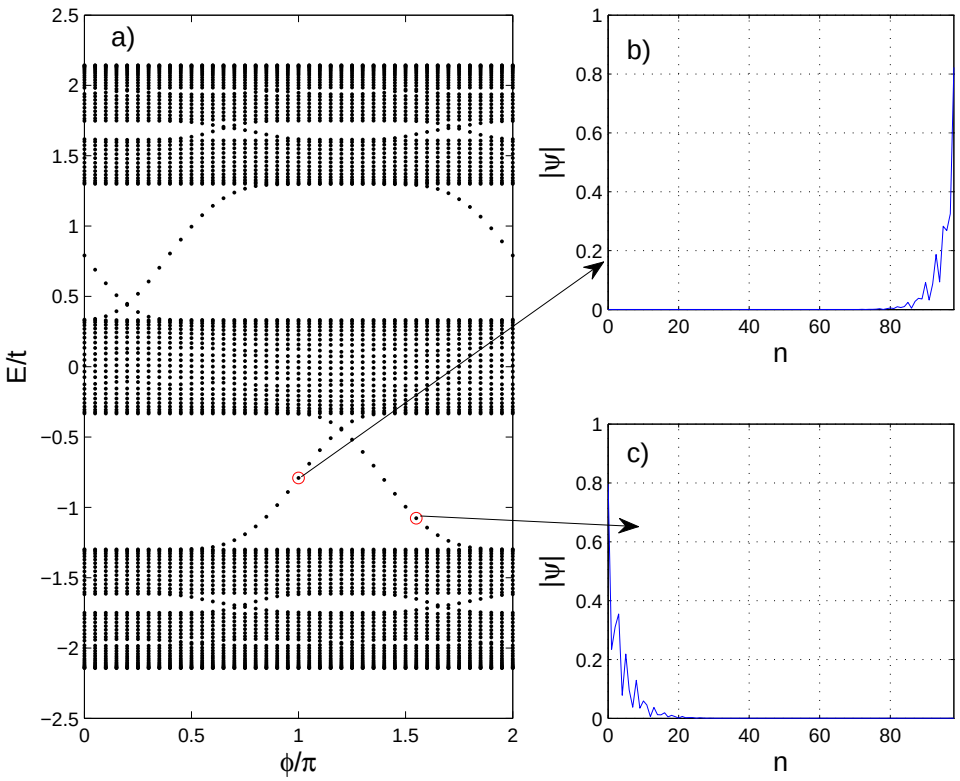

Figure 4.1: a) The eigenspectrum of the AA model with fixed boundary conditions as a function of ϕ with $N = 99$ and $\alpha = (\sqrt{5}+1)/2$. States that cross the bulk band gaps are localized at the edge of system. Examples are shown in b) and c).

Harper/AA model with periodic boundary conditions:

$$Eu_n = te^{i\theta/N}u_{n+1} + te^{-i\theta/N}u_{n-1} + \lambda\cos(2\pi\alpha n + \phi)u_n. \tag{4.1}$$

where N is the system size. The additional phase terms, $\exp(i\theta/N)$, on the hopping coefficients threads $\theta/2\pi$ flux quanta through the ring and is equivalent to imposing a twisted boundary condition along the x-axis in the 2D ancestor model (i.e. $\Psi(x + L, y) = \exp(i\theta)\Psi(x, y)$ for $L = Na$). Similarly, fixing ϕ is equivalent to imposing a twisted boundary condition along the y-axis (i.e. $\Psi(x, y + L) = \exp(i\phi)\Psi(x, y)$ for $\phi = k_y L$). Thus, following TKNN, Avron, and others [11, 58, 59], the Chern number of the 2D ancestor model can be found from the following integral:

$$\nu = \frac{1}{2\pi i}\int d\theta d\phi C(\theta, \phi), \tag{4.2}$$

where $C(\theta, \phi)$ is the "Chern density" given by

$$C(\theta, \phi) = \mathrm{Tr}\left(P(\theta, \phi)\left[\frac{\partial P}{\partial\theta}, \frac{\partial P}{\partial\phi}\right]\right). \tag{4.3}$$

The projection operator, $P(\theta, \phi)$, is given by

$$P(\theta, \phi) = \sum_{E_m < E_{\mathrm{gap}}} |\psi_m(\theta, \phi)\rangle \langle\psi_m(\theta, \phi)|, \tag{4.4}$$

where $|\psi_m(\theta, \phi)\rangle$ is an eigenstate of Eq. (4.1) with eigenvalue E_m and E_{gap} is the energy at the center of a gap.

Following Kraus *et al.*[98], we examine the dependence of the Chern density with respect to θ and ϕ. From Eq. (4.1), we see that the effect of θ is suppressed by $1/N$, so we expect that in the thermodynamic limit, (i.e. $N \to \infty$), the Chern density becomes constant with respect to θ. For irrational α, Kraus *et al.* argues

that in the thermodynamic limit, for any phase shift $\phi_\epsilon = 2\pi m/N$ for integer m, there exist an integer n_ϵ independent of ϕ such that the shift in phase $\phi \to \phi + \phi_\epsilon$ is equivalent to a translation of the lattice sites $n \to n + n_\epsilon$. Spatial translations in the lattice do no affect the spectrum (i.e. close energy gaps). Therefore, given the correspondence between shifts in ϕ and translations, changing ϕ has no physical consequences (although the wavefunctions may change, the spectrum will not). Thus it can be argued that $\partial H/\partial\phi$ is independent of ϕ in the thermodynamic limit and, therefore, the Chern density is a constant in θ and ϕ. So for constant Chern density, $2\pi C/i$ is an integer. As a result, this integer can be associated to the 1D AA equation for arbitrary ϕ in the thermodynamic limit when α is irrational.

4.2 Chern number in the Harper/Aubry-André Model without disorder

We now examine the topological aspects of the Harper/AA model by numerically calculating the Chern number and the Chern density for the altered Harper/AA model with varying ϕ and θ. Results on the Chern number for $\alpha = 1/3$ are shown in Fig. 4.2 for $\lambda = 1$ and $\lambda = 6$. Also shown is the density of states. In the figures, we see that in the areas where the Fermi energy is within an energy band, the Chern number is not an integer. This is indicative of level crossings as a function of θ and/or ϕ where, strictly speaking, the Chern number is not well defined. However, changes in ν within a band can be thought of as an indicator of "current-carrying" states. Between integer values within the energy band gaps, the Chern number

varies monotonically for both $\lambda = 1$ and $\lambda = 6$. This differs from the case with $\alpha = (\sqrt{5}+1)/2$ (the AA model), which is shown in Fig. 4.3. In this case, we see peaks in the lower and upper band of the spectrum, possibly indicating the presence of "sub-bands" with non-trivial topology. But these peaks are not integer valued. This suggests that these "sub-bands" are not fully formed in the sense that they do not form a complete subspace in which the Chern number is well defined. This is similar to earlier results reported on the Hall conductivity in 2D systems with anomalous band structure[113].

The main difference between rational and irrational values for α (i.e. the Harper and AA models respectively), can be made evident by examining the Chern density as a function of ϕ. According to Kraus *et al.*, for irrational α, the Chern density becomes independent of ϕ in the thermodynamic limit. To examine this argument we calculate the Chern density and integrate over θ. In particular, we calculate

$$\bar{C}(\phi) = -i \int d\theta C(\theta, \phi). \tag{4.5}$$

For C constant, $\bar{C}$ is an integer (i.e. $\bar{C} = 2\pi C/i$). Calculations for $\bar{C}(\phi)$ are given in Fig. 4.4 with $N = 105$. In the case of $\alpha = 1/3$, we see that $\bar{C}$ oscillates as a function of ϕ with relatively large amplitude. In contrast, in the case of $\alpha = (\sqrt{5}+1)/2$ the variation is relatively small which is consistent with Kraus *et al.*. In both cases, however, the amplitude appears to increase with λ. At least in the case of $\alpha = (\sqrt{5}+1)/2$, we suspect that the non-zero amplitude in $\bar{C}(\phi)$ to be a finite size effect given Kraus *et al.* arguments but it seems this effect is dependent on λ. To

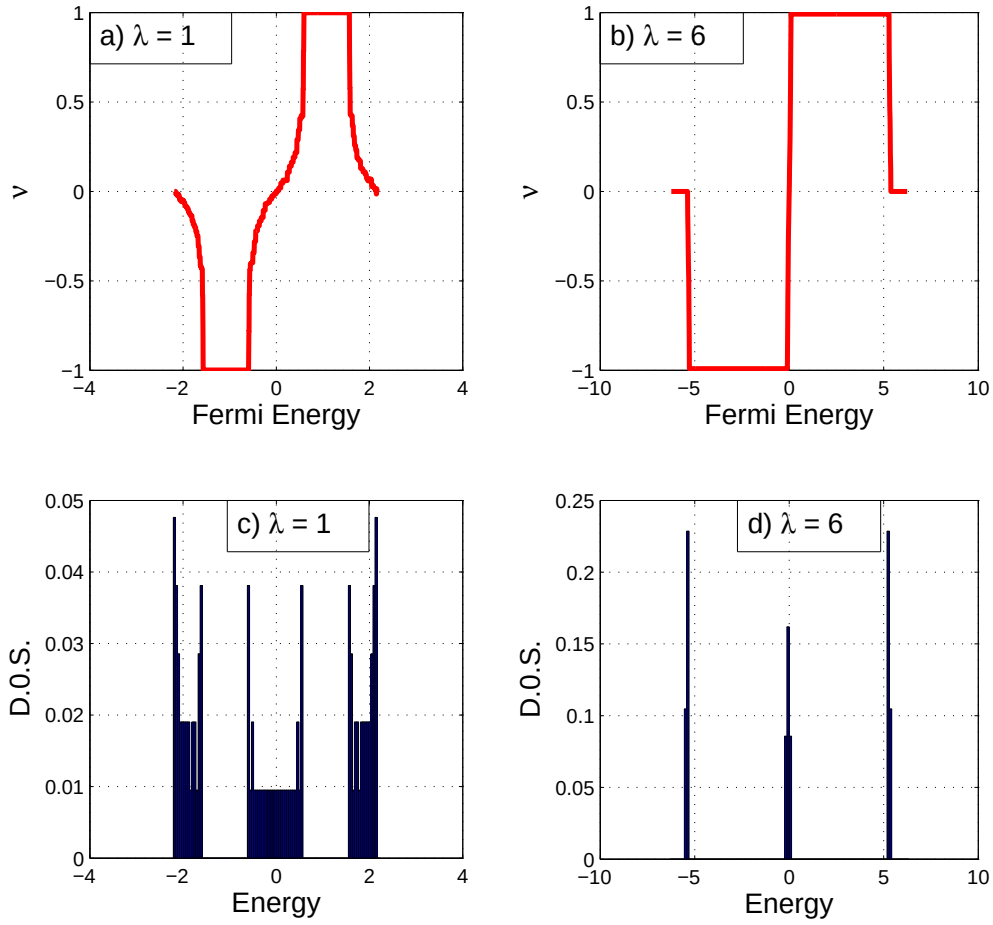

Figure 4.2: The Chern number as a function of the Fermi energy with $\alpha = 1/3$, $N = 105$ for a) $\lambda = 1$ and b) $\lambda = 6$. The respective density of states are given in c) and d).

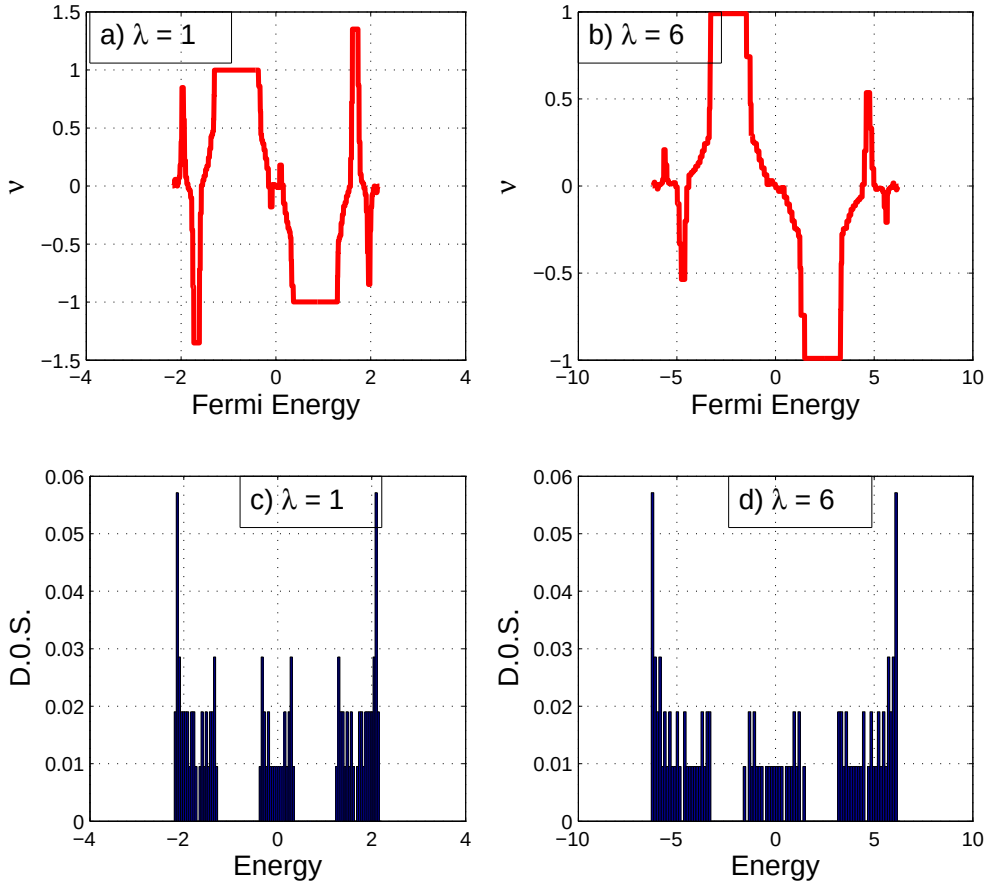

Figure 4.3: The Chern number as a function of the Fermi energy with $\alpha = (\sqrt{5}+1)/2$, $N = 105$ for a) $\lambda = 1$ and b) $\lambda = 6$. The respective density of states are given in c) and d).

examine this further and to verify that the amplitude does approach zero in the thermodynamic limit, we calculate the Chern density for several different system sizes and estimate the amplitude by calculating the statistical standard deviation of $\bar{C}(\phi)$ over the discretized grid of points in ϕ that are used in the numerics. We denote this estimate as $\sigma(\bar{C})$. The result of this is shown in Fig. 4.5(a) for $\lambda = 1$, 2, 4, and 6 as a function of $1/N$. The data shown in the figure are obtained for system sizes $N = 21 - 100$. In the figure, we see that the the amplitude of the Chern density fluctuates for different system sizes, but tends towards zero with $1/N$ as expected. Despite the fluctuations, the overall trend in the amplitude with $1/N$ appears linear, so we have fitted the results to a simple linear relation with the y-intercept fixed at zero. The results are shown by the dashed lines. The slopes of these fits are plotted against λ in Fig. 4.5(b). Here we see that the slopes appear to increase linearly with λ. It would be interesting to verify this result with a larger set of values for λ. This verification we leave for future work.

4.3 Chern number in the disordered Harper/AA model

We now introduce random disorder into the Harper/AA model and examine how robust the Chern number is with respect to disorder. In particular, we now study the model

$$Eu_n = te^{i\theta/N}u_{n+1} + te^{-i\theta/N}u_{n-1} + (\lambda\cos(2\pi\alpha n + \phi) + v_n)u_n, \tag{4.6}$$

where v_n is random disorder uniformly distributed from $[-v/2, v/2]$. To study this model, we can apply Eqs. (4.2) and (4.3) and average the results over several differ-

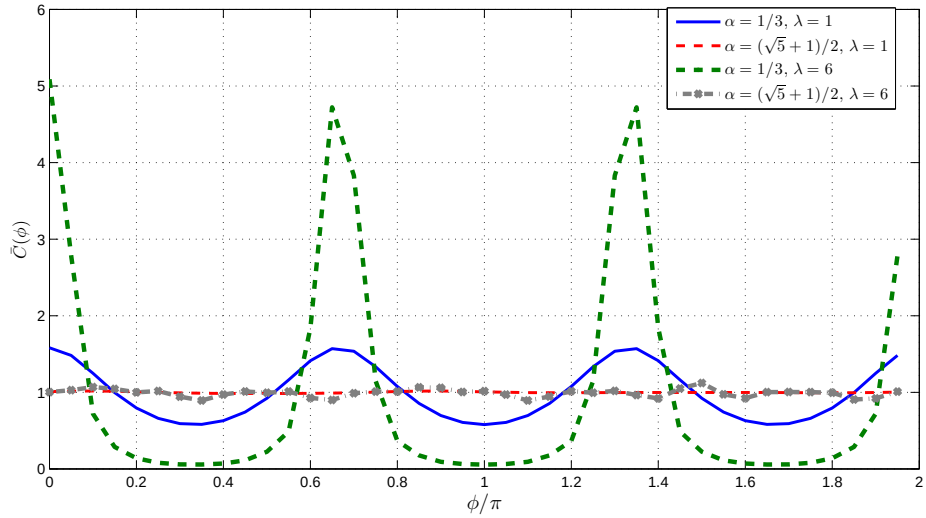

Figure 4.4: Chern density, $\bar{C}$ as a function of ϕ in the altered Harper model with $N = 105$.

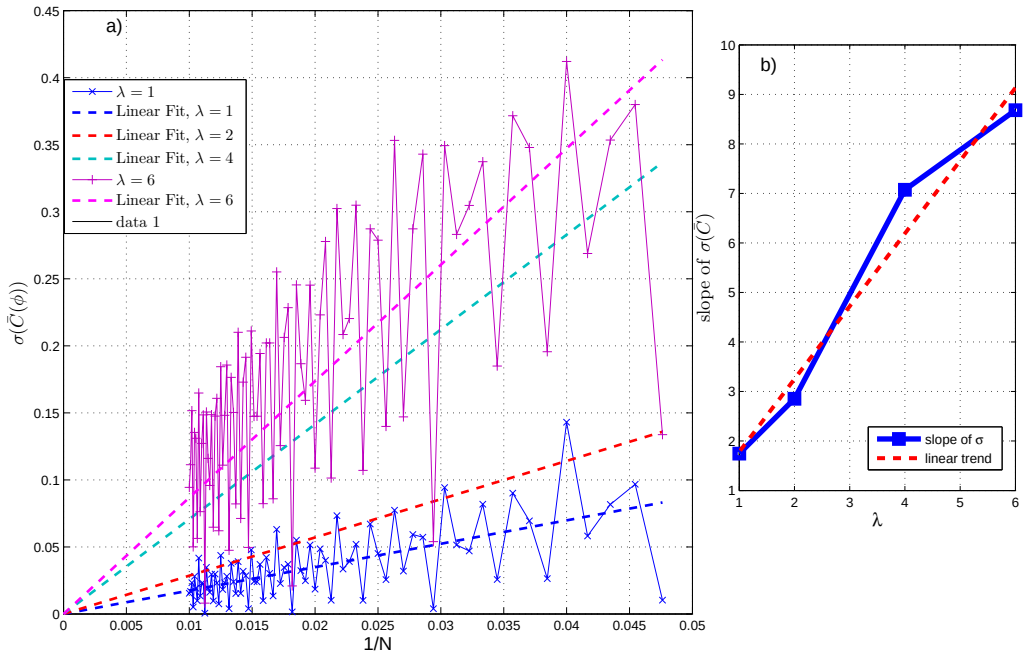

Figure 4.5: a) Standard deviation of the Chern density as a function of $1/N$. The numerical results for $\lambda = 1$ and $\lambda = 6$ are given by the solid, marked curves. The dashed curves give linear fits to results for $\lambda = 1$, 2, 4, and 6. The linear fits are performed with the intercept fixed at 0. b) Slopes of the linear fits in (a) as a function of λ. The approximate linear trend in the slopes with lambda is shown by the dashed line.

ent realizations of v_n to obtain an ensemble average, but this is a numerically cumbersome task. An alternative approach is to take advantage of the "non-commutative" Chern number introduced by Bellissard et al. [99] to study disorder in the IQHE. In this approach, the formalism of non-commutative geometry is applied to generalize the definition of the Chern number for disordered systems without the use of twist angles. We will now very briefly summarize this approach. For full details the interested reader is encouraged to examine the report by Bellissard et al. in Ref. [99]. Also details on how to implement this approach numerically for various systems beyond IQHE is described in Ref. [114], which we will mostly follow here.

To very briefly summarize the non-commutative approach, first consider the 2D case with no disorder where the crystal momentum, $\boldsymbol{k}$, is well-defined. In this case the Chern number can be obtained by integrating the Chern density over the first Brillouin zone,

$$\nu = \frac{1}{2\pi i} \int dk^2 \mathrm{Tr} \left(P_k(k_x, k_y) \left[\frac{\partial P_k}{\partial k_x}, \frac{\partial P_k}{\partial k_y} \right] \right), \tag{4.7}$$

where the projection operator, P_k is defined in the same way as Eq. (4.4), but is now considered a function $\boldsymbol{k}$ instead of the twist angles. To generalize the Chern number for disordered systems where the crystal momentum is no longer a good quantum number, we first note that the partial derivative of an operator with respect to $\boldsymbol{k}$ can be written as a commutator: $\partial_{k_i} A = -i[x_i, A]$ where x is the position operator. This commutator is well-defined even in the case of disorder where $\boldsymbol{k}$ is no longer a good quantum number. Next, we note that for certain operators, $A(k)$, in the unperturbed Hilbert space, there are a family of operators, A_ω associated with

disorder configurations $\omega \in \Omega$ such that in the thermodynamic limit

$$\frac{1}{(2\pi)^2}\int d^2k \mathrm{Tr}[A(k)] = \lim_{N\to\infty}\frac{1}{N^2}\int dP(\omega)\mathrm{Tr}[A_\omega], \tag{4.8}$$

where $dP(\omega)$ is the probability measure for the disorder configuration, ω. These observations allow for the construction of a so-called "non-commutative Brillouin zone" where a Chern number can be defined and is given by

$$\nu = \lim_{N\to\infty}\frac{2\pi i}{N^2}\int dP(\omega)\mathrm{Tr}\left[P_\omega[-i[x,P_\omega],-i[y,P_\omega]]\right]., \tag{4.9}$$

where P_ω is the projection operator in the disordered configuration, ω. For a more through discussion of the non-commutative Chern number, see [99] and [114].

We now seek to apply this idea to the disordered Harper/AA model. A straightforward extension of Eq. (4.9) to our 1D disordered problem is to consider a "hybrid" space consisting of the 1D disordered configuration, ω, and the extra-dimensional parameter ϕ. The hybrid expression for the Chern number is given by

$$\nu = \frac{i}{N}\int dP(\omega)d\phi\mathrm{Tr}\left[P_{\phi,\omega}\left[-i\left[x,P_{\phi,\omega}\right],\frac{\partial P_{\phi,\omega}}{\partial\phi}\right]\right]. \tag{4.10}$$

An example of Eq. (4.10) in use is given in figure 4.6 for the case with $\alpha = 1/3$, $\lambda = 1$, and disorder strength $v = 0.6$. Fig. 4.6(a) shows the "raw" Chern numbers as a function of energy for 100 different random configurations. Fig. 4.6(b) shows the average Chern number as function of the Fermi energy. Note that this result only differs qualitatively with the case without disorder (Fig 4.2(a)) by a sign. The similarity suggests that Eq. (4.10) behaves as we expect.

In Fig. 4.7, we show the effect of disorder on ν in the case of $\alpha = (\sqrt{5}+1)/2$ with $\lambda = 1$. For small disorder (i.e. $v = 0.1$) ν is qualitatively similar to the results

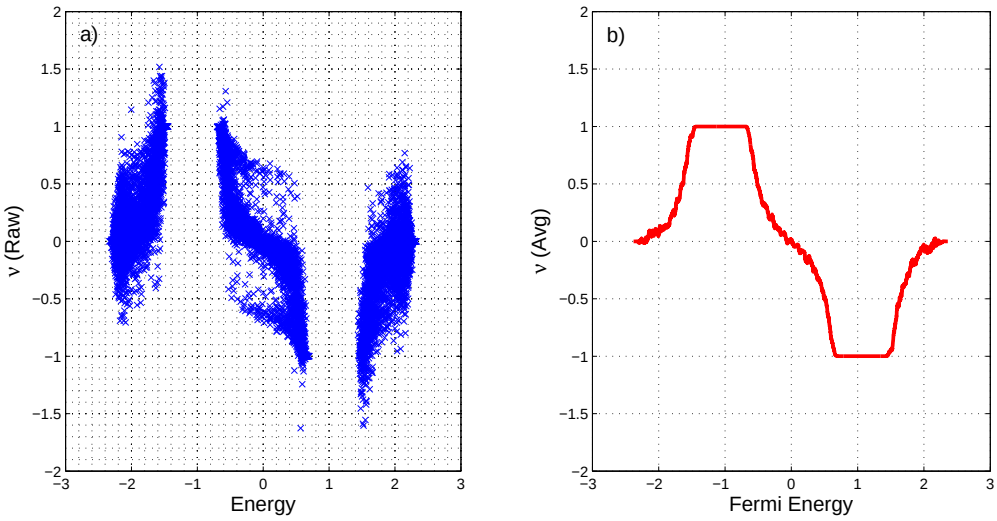

Figure 4.6: Chern number, ν, for disordered Harper model using Eq. (4.10) for $\alpha = 1/3$, $\lambda = 1$, $v = 0.6$, and $N = 99$. a) "Raw" values of ν for 100 different realizations of the disordered potential as a function of energy and b) the average values for ν as function of the Fermi energy.

in Fig. 4.3(a). For intermediate disorder (i.e. $v = 0.1$), the peaks are suppressed, but ν does reach integer values in the band gaps. In strong disorder, ν varies weakly with energy but never reaches integer values other than zero. In this case, the bands have almost completely mixed due to the disorder (Fig. 4.7(d)). As a result, the contributions to ν from states in different bands cancel each other out. Thus qualitatively speaking, the topological Chern number is robust to the presence of random disorder provided the disorder strength is weaker than the band gap. Only for disorder stronger than the original band gap are the topological features destroyed.

To get a sense of how the Chern number varies with both λ and v, we calculate ν for the first band gap which we determine from the spectrum of the non-disordered model for each value of λ under investigation. The result for $\alpha = 1/3$ is shown in

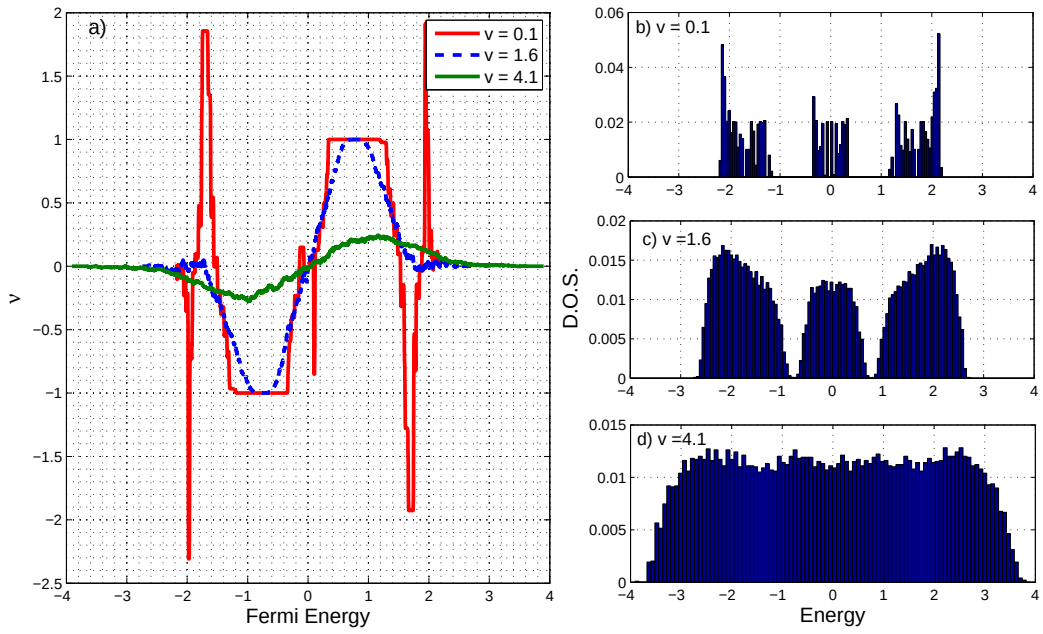

Figure 4.7: a) Chern number, ν, for disordered AA model using Eq. (4.10) for $\alpha = (\sqrt{5}+1)/2$, $\lambda = 1$, and $N = 99$ at different values for the disorder strength, v. The density of states are given for $v =$ b) 0.1, c) 1.6, d) 4.1.

Fig. 4.8(a) with $N = 84$. For comparison, we also provide the band-gap as a function of v and λ in Fig. 4.8(b). From the figure, we see that ν remains near the integer value, 1, for $v \lesssim 2$. This boundary appears to be insensitive to λ and does not correlate with any equipotentials in the band gap. However, the $\lambda - v$ contour for $\nu \sim 0.5$ does, qualitatively, appear to vary linearly with λ and correlates with the $E \sim 0$ equipotential in the plot for the band gap. The case for $\alpha = (\sqrt{5}+1)/2$ gives similar results and is shown in Fig. 4.9. Here we see also that $\nu \sim -1$ for $v \lesssim 2$ and the $\nu \sim -0.5$ contour increases monotonically with λ. But in this case, the band gap equipotentials appear to vary with the root of λ in contrast to the previous case.

We now examine the effect of random disorder on the Chern density and how it

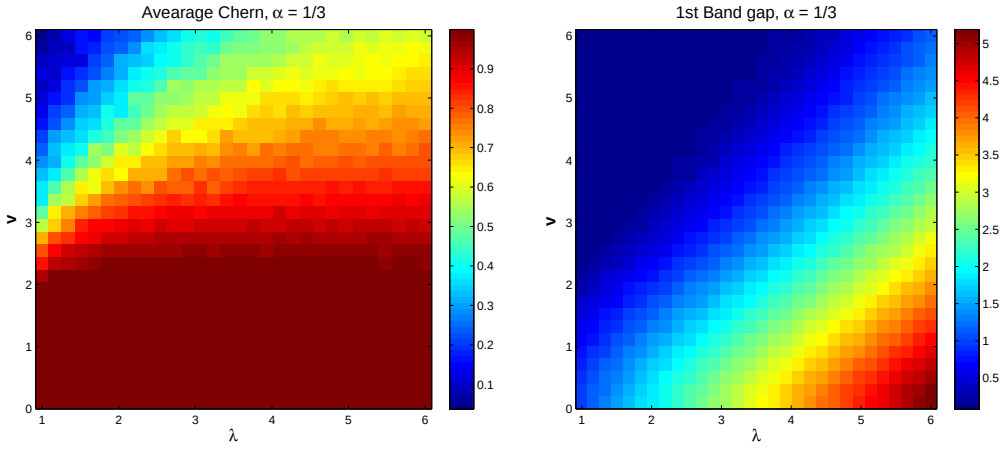

Figure 4.8: a) Chern number, ν, of the first band gap for the disordered Harper model with $\alpha = 1/3$ and $N = 84$. b) Size of the first band gap as a function of λ and v in units of t.

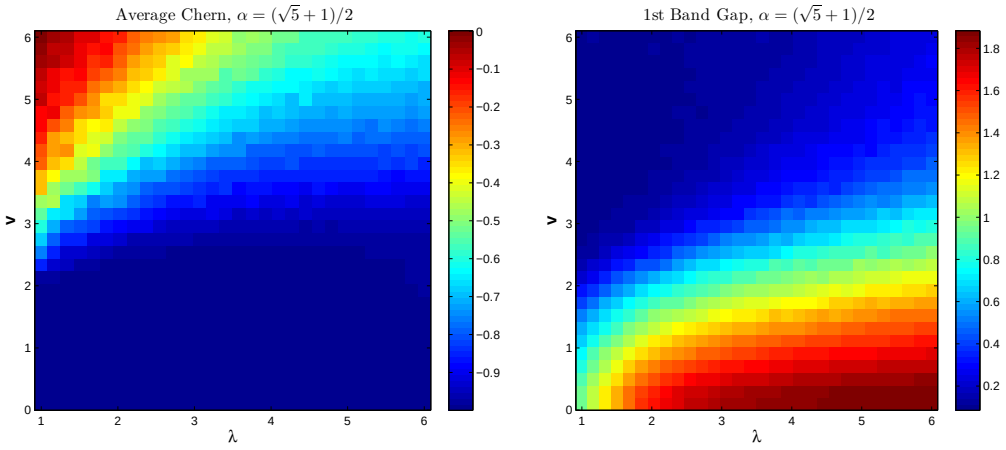

Figure 4.9: a) Chern number, ν, of the first band gap for the disordered Harper model with $\alpha = (\sqrt{5}+1)/2$ and $N = 84$. b) Size of the first band gap as a function of λ and v in units of t.

varies with the angle ϕ. In the context of Eq. 4.10, we define $\bar{C}(\phi)$ in the disordered case as

$$\bar{C}(\phi) = \frac{2\pi i}{N} \int dP(\omega) \mathrm{Tr} \left[P_{\phi,\omega} \left[-i \left[x, P_{\phi,\omega} \right], \frac{\partial P_{\phi,\omega}}{\partial \phi} \right] \right]. \tag{4.11}$$

For $\bar{C}$ independent of ϕ, $\bar{C} = \nu$. Similar to what was done in the case of no disorder, we diagonalize the system for different values of N and estimate the amplitude of $\bar{C}(\phi)$ by calculating the standard deviation over the mesh of points used in the numerics. Again, we denote this result by $\sigma(\bar{C})$. The results of this calculation are given if Fig. 4.10 as a function of $1/N$ for $\lambda = 1$, and $N = 21 - 100$. In the case of $\alpha = 1/3$ (Fig 4.10(a)), $\sigma(\bar{C})$ increases somewhat with N with low disorder (i.e. $v = 0.1, 1.36$). In the highly disordered case ($v = 6$), $\sigma(\bar{C})$ decreases with N and is likely zero in the thermodynamic limit. This corresponds to the case where the bands have completely mixed and the total Chern number is zero. For $\alpha = (\sqrt{5}+1)/2$, we see that $\sigma(\bar{C})$ decreases with N in small ($v = 0.1, 1.36$) and large disorder ($v = 6$), but increases with N with "intermediate" disorder. This may be indicative of some kind of "phase" transition. It is interesting to see that for α irrational, $\sigma(\bar{C})$ behaves similarly for small and large disorder. The case of $\lambda = 6$ is shown in fig. 4.11. Here, $\sigma(\bar{C})$ is constant or slightly increasing with N for $\alpha = 1/3$ and decreasing with N for $\alpha = (\sqrt{5}+1)/2$ in all cases shown.

To summarize the effect of disorder on the Chern density, we perform a linear fit on $\sigma(\bar{C})$ and examine how the fitting parameters vary with v. In particular, we estimate the parameters c_1 and c_2 such that $\sigma(\bar{C}) \sim c_1/N + c_2$. The result of this is shown if Fig. 4.12. For $\lambda = 1$, c_1 (Fig. 4.12(a)) is initially negative for $\alpha = 1/3$

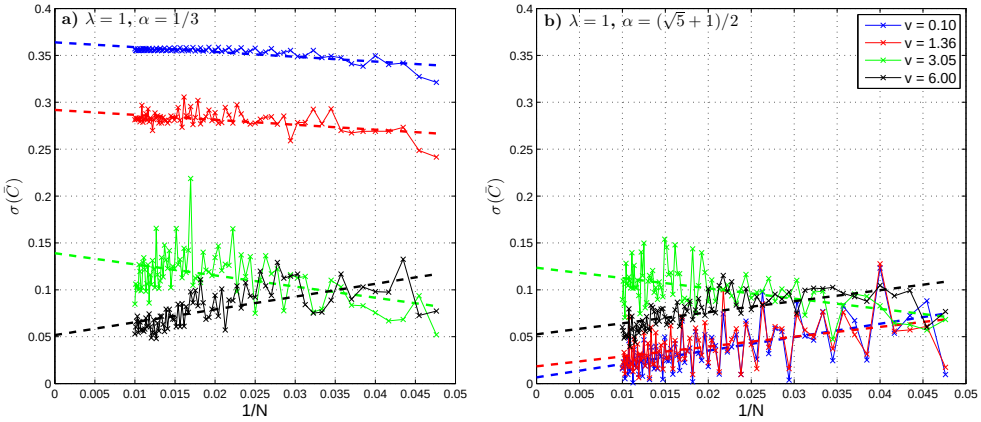

Figure 4.10: Standard deviation of the Chern density, $\sigma(\bar{C})$ as a function of $1/N$ for the disordered Harper model at different disorder strengths (v) with $\lambda = 1$, a) $\alpha = 1/3$ and b) $\alpha = (\sqrt{5}+1)/2$. The dashed lines are linear fits to $\sigma(\bar{C})$.

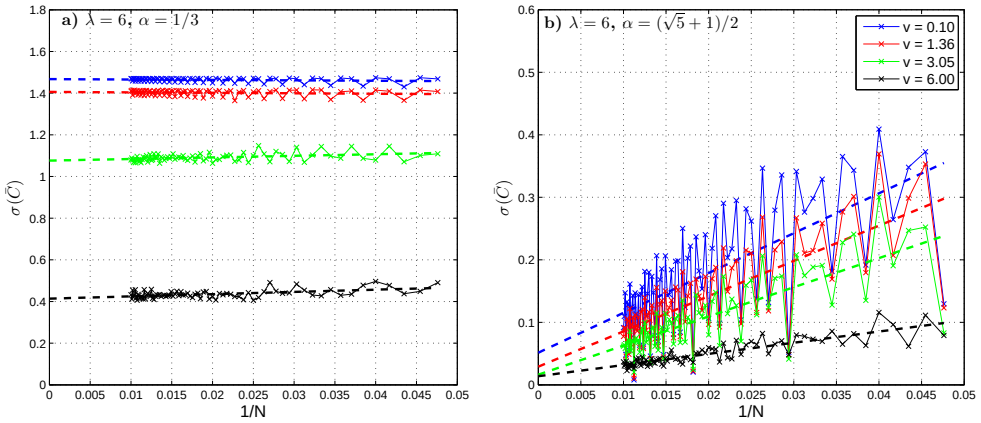

Figure 4.11: Standard deviation of the Chern density, $\sigma(\bar{C})$ as a function of $1/N$ for the disordered Harper model at different disorder strengths (v) with $\lambda = 6$, a) $\alpha = 1/3$ and b) $\alpha = (\sqrt{5}+1)/2$. The dashed lines are linear fits to $\sigma(\bar{C})$.

and positive for $\alpha = (\sqrt{5}+1)/2$ as was seen in the case of no disorder. As v is increased however, c_1 decreases for $\alpha = (\sqrt{5}+1)/2$ and eventually becomes negative near $v \sim 2$. This is the transition that was observed in Fig. 4.10(b). After this transition, the value of c_1 for $\alpha = (\sqrt{5}+1)/2$ takes on similar values to those with $\alpha = 1/3$, which both begin to increase for $v \gtrsim 3$. Similar trends are seen for the intercept in Fig. 4.12(b). Here c_2 is relatively large initially for $\alpha = 1/3$ then begins to decrease. c_2 for $\alpha = (\sqrt{5}+1)/2$ has the opposite trend initially until $v \sim 3$ where the two cases both begin to decrease in v while giving very similar values for c_2. These results seem to suggest that the two systems transition to similar states near $v \sim 3$. Thus it could be argued that the there is no longer any distinction between rational and irrational α at this point. But it should be noted that ν is non-zero at this transition point for both cases ($|\nu| \sim 0.5$), so we can not say that the disorder has completely suppressed the contributions from the extra-dimensional parameter. Figs. 4.12(c) and (d), show the case for $\lambda = 6$ where there does not appear to be a transition point where the two cases merge in the disorder strengths shown, but we expect from the trends in the figures and from the results of $\lambda = 1$, that such a point exists for some $v > 6$.

4.4 Conclusions

In summary, we have examined topological aspects of the Harper and AA models with and without random disorder through numerical calculations of the Chern number. Our calculations support the argument that the case of irrational α (i.e.

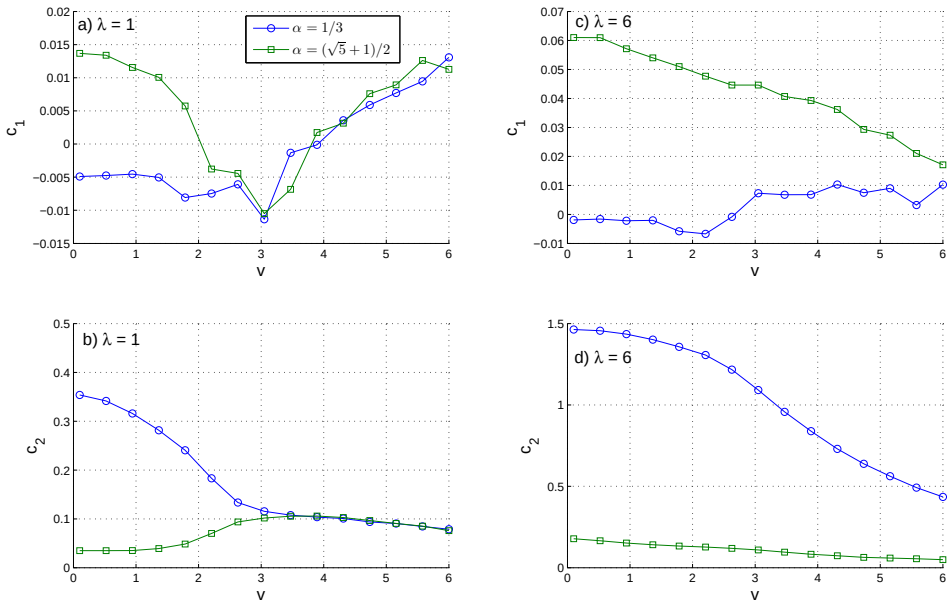

Figure 4.12: Results on the linear fitting parameters c_1, and c_2 where $\sigma(\bar{C})) \sim c_1/N + c_2$ for $\lambda = 1$ ((a) and (b) respectively) and $\lambda = 6$ ((c) and (d) respectively).

a quasi-crystal) has topological properties that are distinct from the rational case (i.e. normal crystal). In particular, we have shown that the variations in the Chern density decreases with increasing system size, suggesting that it is constant in the thermodynamic limit. We have also shown through the use of the non-commutative Chern number, that this distinction can be destroyed by the introduction of disorder. There results are not surprising since we might expect that disorder will eventually overshadow the lattice, leading to the two cases to look identical.

Chapter 5

Landau Levels in the Quantum Hall Effect

In this chapter, we briefly review some of the main results on Landau levels and their single particle eigenstates. Many of these results are used in subsequent chapters to study the quantum Hall effect. More through derivations can be found in Refs. [54, 55, 56].

5.1 Planar Geometry

A single non-relativistic electron with mass m and electric charge $q = -e$ confined to two dimensions and in the presence of a uniform perpendicular magnetic field is described by the time independent Schrodinger equation, $H\Psi = E\Psi$ where the Hamiltonian, H, is given by

$$H = \frac{1}{2m}\left(\boldsymbol{p} + \frac{e\boldsymbol{A}}{c}\right)^2, \tag{5.1}$$

$\boldsymbol{p} = -i\hbar\nabla$ is the canonical momentum, and $\boldsymbol{A}$ is the vector potential which is related to the magnetic field by $\nabla \times \boldsymbol{A} = B\hat{z}$. The Hamiltonian is gauge invariant, so we are free to choose a convenient gauge to solve Eq. (5.1). For now, we use the Landau gauge where $\boldsymbol{A} = (0, Bx, 0)$. With this choice of vector potential, the Hamiltonian becomes

$$H = \frac{p_x^2}{2m} + \frac{1}{2m}\left(p_y + \frac{eBx}{c}\right). \tag{5.2}$$

There is no dependence on y, so $p_y = \hbar k_y$ is a good quantum number. As a result, the problem maps to that of a simple harmonic oscillator. Defining the magnetic length, $\ell = \sqrt{\hbar c/eB}$, and the cyclotron frequency, $\omega_c = eB/mc$, we have for the Hamiltonian:

$$H = \frac{p_x^2}{2m} + \frac{1}{2}m\omega_c^2\left(x + \ell^2 k_y\right). \tag{5.3}$$

This is a simple harmonic oscillator with shifted center about $x_0 = \ell^2 k_y$. Thus, the energy eigenvalues are the same as those in the harmonic oscillator: $E_n = \hbar\omega_c(n + 1/2)$ where n is a non-negative integer. The eigenstates are plane waves in the y dimension, and harmonic oscillator wavefunctions in the x dimension. The (unnormalized) eigenstate, for quantum numbers, k_y and n, is given by

$$\Psi(x, y) = e^{ik_y y} e^{-\frac{1}{2}\left(\frac{x}{\ell} + \ell k_y\right)^2} H_n\left(\frac{x}{\ell} + \ell k_y\right), \tag{5.4}$$

where H_n are the Hermite polynomials. The degeneracy per unit area (ignoring spin) is given by $G = 1/(2\pi\ell^2) = B/\phi_0$, where $\phi_0 = hc/e$ is the magnetic flux quantum.

In some cases, it is more convenient to work in the symmetric gauge where $\boldsymbol{A} = B(-y/2, x/2, 0)$. In this gauge, the Hamiltonian is given by

$$\begin{aligned} H &= \frac{1}{2m}\left(p_x - \frac{eBy}{2c}\right)^2 + \frac{1}{2m}\left(p_x - \frac{eBy}{2c}\right)^2 && (5.5)\\ &= \frac{1}{2m}\left(p_x^2 + p_y^2\right) + \frac{e^2B^2}{8mc^2}\left(x^2 + y^2\right) + \frac{eB}{2mc}\left(xp_y - yp_x\right) && (5.6)\\ &= \frac{1}{2m}\left(p_x^2 + p_y^2\right) + \frac{1}{2}\left(\frac{\omega_c}{2}\right)^2\left(x^2 + y^2\right) + \frac{eB}{2mc}L_z, && (5.7) \end{aligned}$$

where $L_z = xp_y - yp_x$ is the z-component of the orbital angular momentum. This Hamiltonian describes two decoupled harmonic oscillators with an additional term

that couples to angular momentum. The Hamiltonian commutes with L_z, so H and L_z can be diagonalized simultaneously. In terms of the ladder operators, $a_i, a_i^\dagger$, the Hamiltonian becomes

$$H = \hbar\frac{\omega_c}{2}\left(a_x^\dagger a_x + a_y^\dagger a_y + 1\right) + i\hbar\left(a_x a_y^\dagger - a_x^\dagger a_y\right) \tag{5.8}$$

where the ladder operators are given by

$$a_x = \sqrt{\frac{m\omega_c}{2\hbar}}\left(x + \frac{i}{m\omega_c}p_x\right) \tag{5.9}$$

$$a_x^\dagger = \sqrt{\frac{m\omega_c}{2\hbar}}\left(x - \frac{i}{m\omega_c}p_x\right). \tag{5.10}$$

Similarly for a_y. A more convenient form for the Hamiltonian comes from making the following canonical transformation:

$$a = \frac{a_x - ia_y}{\sqrt{2}} \tag{5.11}$$

$$b = \frac{a_x + ia_y}{\sqrt{2}}. \tag{5.12}$$

The resulting commutation relations are $[a, a^\dagger] = 1$, $[b, b^\dagger] = 1$ with all other combinations resulting in zero. Then the Hamiltonian and L_z are now written as

$$H = \hbar\omega_c\left(a^\dagger a + \frac{1}{2}\right) \tag{5.13}$$

$$L_z = -\hbar\left(b^\dagger b - a^\dagger a\right). \tag{5.14}$$

If we denote the eigenstates by $|n, m\rangle$ where $L_z|n, m\rangle = -m\hbar|n, m\rangle$ and $H|n, m\rangle = E_n|n, m\rangle$ and noting that the eigenvalues of the number operators (i.e. $N_a = a^\dagger a$, $N_b = b^\dagger b$ must be non-negative), then the eigenvalue, m, takes on integer values between $-n$ to ∞. This implies that the operation of $b^\dagger$ increases m by one while

$a^\dagger$ increases n by one and decreases m by one. Thus the eigenstates are given by

$$|n,m\rangle = \frac{(b^\dagger)^{m+n}}{\sqrt{(m+n)!}} \frac{(a^\dagger)^n}{\sqrt{n!}} |0,0\rangle \,. \tag{5.15}$$

To determine $\langle \boldsymbol{r}|n,m\rangle$, we solve the equation $a\,|0,0\rangle = b\,|0,0\rangle = 0$ where the ladder operators can be written in terms of $z = x - iy$ and $\bar{z} = x + iy$,

$$b = \frac{1}{\sqrt{2}}\left(\frac{\bar{z}}{2\ell} + 2\ell\frac{\partial}{\partial z}\right), \tag{5.16}$$

$$b^\dagger = \frac{1}{\sqrt{2}}\left(\frac{z}{2\ell} - 2\ell\frac{\partial}{\partial \bar{z}}\right), \tag{5.17}$$

$$a^\dagger = \frac{1}{\sqrt{2}}\left(\frac{\bar{z}}{2\ell} - 2\ell\frac{\partial}{\partial z}\right), \tag{5.18}$$

$$b = \frac{1}{\sqrt{2}}\left(\frac{z}{2\ell} - 2\ell\frac{\partial}{\partial \bar{z}}\right). \tag{5.19}$$

This ultimately leads to the following wavefuntions (see [56, 115] for complete derivation)

$$\eta_{n,m} = \frac{(-1)^n}{\sqrt{2\pi}} \sqrt{\frac{n!}{2^m(m+n)!}} e^{-\frac{r^2}{4}} z^m L_n^m\left(\frac{r^2}{2}\right), \tag{5.20}$$

where $L_n^m(r)$ are the Laguerre polynomials.

5.2 Spherical Geometry

We now examine the case of an electron confined to the surface of a sphere with fixed radius, R that surrounds a hypothetical magnetic monopole with magnetic charge $2Q$. One of the advantages of the spherical geometry is that there are no edges, so bulk properties are much more easily accessible in calculations. Also, each Landau level has finite degeneracy, so it is easier to work with full or partially filled Landau levels given a finite number of electrons. These aspects make it easier to study FQHE states numerically in many cases[56]. In subsequent chapters, we will

work exclusively in the spherical geometry. In this section, we give a very brief overview of the Landau levels on the sphere. For a complete discussion, see Refs. [116, 117].

The non-interacting Hamiltonian on the sphere surrounding a magnetic monopole with magnetic charge, $2Q$, is given by

$$H = \frac{\hbar^2}{2mR^2} \left|\mathbf{\Lambda}\right|^2, \tag{5.21}$$

where

$$\mathbf{\Lambda} = \boldsymbol{R} \times \left(-i\nabla + \frac{e}{\hbar c}\boldsymbol{A}(\mathbf{\Omega})\right), \tag{5.22}$$

$\mathbf{\Omega} = \boldsymbol{R}/R$, and the flux through the surface is $2\left|Q\right|\phi_0 = 4\pi R^2\left|B\right|$. For the vector potential, it has been shown that any gauge choice will have at least one singularity in the vector potential [118]. Also it has been shown that in order for this singularity to not have any physical consequences, $2Q$, must be an integer (for details see Refs. [119, 120, 121]). The singularity can be removed by patching the surface of the sphere with different over-lapping gauge choices, similar to coordinate maps on a manifold [119, 120, 121], but this is not necessary for our purposes since the Coulomb matrix elements are not affected by the singularity. In this section, we will use the following gauge choice:

$$\boldsymbol{A} = \frac{-\hbar c Q}{eR}\cot(\theta). \tag{5.23}$$

An angular momentum operator can be introduced by noting that the operators $\mathbf{\Lambda}$ and $\mathbf{\Omega}$ have the commutation relations (in Cartesian coordinates)

$$[\Lambda_i, \Lambda_j] = i\epsilon_{ijk}(\Lambda_k - Q\Omega_k) \tag{5.24}$$

$$[\Lambda_i, \Omega_j] = i\epsilon_{ijk}\Omega_k. \tag{5.25}$$

Thus, we can introduce the operator

$$\boldsymbol{L} = \boldsymbol{\Lambda} + Q\boldsymbol{\Omega}, \tag{5.26}$$

which satisfies the angular momentum algebra

$$[L_i, L_j] = i\epsilon_{ijk}L_k. \tag{5.27}$$

Since $\boldsymbol{\Lambda} \cdot \boldsymbol{\Omega} = 0$, then it follows that

$$|\boldsymbol{\Lambda}|^2 = |\boldsymbol{L} - Q\boldsymbol{\Omega}|^2 = L^2 - Q^2. \tag{5.28}$$

Thus, the Hamiltonian commutes with $\boldsymbol{L}$ and the solutions can be simultaneous eigenstates of H, L^2, and L_z. These solutions are often referred to as "monopole harmonics" which are similar to the spherical harmonics for $Q = 0$ and are denoted $Y_{Q,l,m}$ where $L_z Y_{Q,l,m} = mY_{Q,l,m}$ and $L^2 Y_{Q,l,m} = l(l+1)Y_{Q,l,m}$. The angular momentum commutation relations constrain the eigenvalues, l and m, such that l must be a non-zero integer or half integer (i.e. $l = 0, 1/2, 1, 3/2, ...$) and $m = -l, -l+1, ...l$ (note that due to the singularities in the vector potential, m is not constrained to only integers as is the case with $Q = 0$ [115]). Also Eq. (5.28) implies that $l(l+1) > Q^2$ which suggests $l = |Q|, |Q|+1, |Q|+2 \cdots$. And the energy eigenvalues are given by

$$E_{Q,l,m} = \hbar^2\omega_c \frac{l(l+1) - Q^2}{2|Q|}. \tag{5.29}$$

In this case, the nth Landau level is associated with eigenvalue $l = |Q| + n$. Thus each Landau level has a finite degeneracy, $G = 2l + 1 = 2(|Q| + n) + 1$. The planar result (i.e. $E_n = \hbar\omega_c(n + 1/2)$) is obtained in the limit $|Q| \to \infty$.

The solutions for the $Y_{Q,l,m}$ are obtained by solving the Schrödinger equation. The solution is given below for the LLL (i.e. Y_{QQm}) without proof (details can be found in Refs. [116, 117, 56])

$$Y_{QQm} = \left(\frac{2Q+1}{4\pi}\binom{2Q}{Q-m}\right)^{1/2}(-1)^{Q-m}v^{Q-m}u^{Q+m}, \tag{5.30}$$

where $v = \sin(\theta/2)\exp(-i\phi/2)$ and $u = \cos(\theta/2)\exp(i\phi/2)$.

A notable difference between the spherical and the planar geometries is that the filling fractions in the spherical geometry are only well defined in the thermodynamic limit,

$$\nu = \lim_{N\to\infty}\frac{N}{2\,|Q|}. \tag{5.31}$$

For finite N, there will often be a shift in the actual filling: $N_\phi = N/\nu - \chi$, where χ is an integer. The shift, χ, will depend on the state under investigation. For example, for the Jain composite fermion wavefunctions at planar filling fraction $\nu = n/(2pn+1)$, the shift is given by $\chi_{\rm CF} = 2p + n$. This shift call also lead to an effect called "aliasing" where a given pair (N, N_ϕ) can fit more than one FQHE state describing different filling fractions[122]. For example, filling fraction $\nu = 2/5$ is aliased with $\nu = 4/7$ for $N = 8$. (Note that the case of N electrons (N_e) at filling fraction ν is equivalent to that of N holes (N_h) at filling fraction $\nu' = 1 - \nu$)

For FQHE states on the sphere, the uniform ground state has total angular momentum, $L = 0$. Thus the ground state can be obtained in the Hilbert subspace where the total z-component of angular momentum, $L_z = 0$.

5.3 The FQHE Hamiltonian and Landau Level Projection

The FQHE Hamiltonian for an interacting two dimensional electron gas in the presence of a perpendicular magnetic field is given by (ignoring disorder)

$$H = \sum_j \frac{1}{2m}\left(\boldsymbol{p} + \frac{e}{c}\boldsymbol{A}(\boldsymbol{r_j})\right)^2 + \frac{e^2}{\epsilon}\sum_{j<k}\frac{1}{|\boldsymbol{r_j} - \boldsymbol{r_k}|} + g\mu\boldsymbol{B}\cdot\boldsymbol{S}, \tag{5.32}$$

where μ is the Bohr magneton and g is the Landé g-factor. The first term is the kinetic energy which leads to quantized Landau levels as discussed in previous sections in the limit of no interactions. The second term is the Coulomb interaction energy. And the third term is the Zeeman energy that describes the coupling between the magnetic field and the electron spin. In studying FQHE, an appropriate starting point can be reached by considering the limit $B \to \infty$. Approaching this limit, the Landau level splitting $E_L \sim \hbar\omega_c$ increases linearly with B, the Zeeman splitting, $E_Z \sim g\mu B$, also increases linearly with B, but the Coulomb energy $E_C \sim e^2/\epsilon\ell$ increases with the square root of B. Therefore in the limit of very large magnetic fields, the splitting between Landau levels, E_L and the energy to flip the spin of an electron in a magnetic field, E_Z are greater than the effective Coulomb energy. As a result, the many-body ground state is expected to be entirely in the lowest Landau level (LLL) (assuming $\nu < 1$) with the spin degree of freedom effectively frozen. Thus we can treat the problem as spinless, interacting electrons residing in the LLL. This gives the following effective Hamiltonian:

$$H = \mathcal{P}_{\mathrm{LLL}}\frac{e^2}{\epsilon}\sum_{j<k}\frac{1}{|\boldsymbol{r_j} - \boldsymbol{r_k}|}\mathcal{P}_{\mathrm{LLL}}, \tag{5.33}$$

where $\mathcal{P}_{\mathrm{LLL}}$ is the projection into the LLL. In the case of higher Landau levels where $\nu > 2$ (i.e. the LLL is filled twice with spin up and spin down electrons) we treat the filled Landau levels as inert and assume all relevant interactions occur in the partially filled Landau level.

Of course, real 2DEG's in experimentally relevant conditions are much more complicated. This is especially true for the Zeeman term. When considering the renormalized mass and Landé factor for an electron inside the band structure of a material (e.g. GaAs) at relevant magnetic fields, the Zeeman energy is often much less than the Coulomb energy. Thus, FQHE states can be polarized, unpolarized, or partially polarized depending on the filling fraction. For most FQHE fractions, the polarization of states is well understood with the application of an altered Hund's rule that is applied to composite fermions rather than electrons [56]. But there are a few cases, particularly the case of $\nu = 5/2$, that is controversial and remains to be settled. This case is studied in more depth in chapter 7.

5.4 Haldane Pseudopotentials

In 1983, Haldane introduce a very useful representation for the Coulomb interaction between particles in the LLL[116]. In this representation, the potential is parametrized in terms of the relative angular momentum between two particles. In this section, we briefly review how these parameters, which are often referred to as "Haldane pseudopotentials," are arrived at. This discussion will largely follow Refs. [56, 115].

Consider the kinetic energy of two particles in a magnetic field (in the symmetric gauge):

$$H = \frac{1}{2m}\left(\boldsymbol{p}_1 + \frac{e}{c}\boldsymbol{A}(\boldsymbol{r}_1)\right)^2 + \frac{1}{2m}\left(\boldsymbol{p}_2 + \frac{e}{c}\boldsymbol{A}(\boldsymbol{r}_2)\right)^2. \tag{5.34}$$

We can transform to the relative and center of mass coordinates, $Z = (z_1 + z_2)/2$ and $z = z_1 - z_2$ (i.e. $\boldsymbol{R} = (\boldsymbol{r_1} + \boldsymbol{r_2})/2$ and $\boldsymbol{r} = \boldsymbol{r_1} - \boldsymbol{r_2}$) and define the relative and center of mass ladder operators

$$b_C^\dagger = \frac{b_1^\dagger + b_2^\dagger}{\sqrt{2}} = \frac{1}{\sqrt{2}}\left(\frac{Z}{2\ell_C} - 2\ell_C\frac{\partial}{\partial \bar{Z}}\right), \tag{5.35}$$

$$b_r^\dagger = \frac{b_1^\dagger - b_2^\dagger}{\sqrt{2}} = \frac{1}{\sqrt{2}}\left(\frac{z}{2\ell_r} - 2\ell_r\frac{\partial}{\partial \bar{z}}\right), \tag{5.36}$$

$$a_C^\dagger = \frac{a_1^\dagger + a_2^\dagger}{\sqrt{2}} = \frac{1}{\sqrt{2}}\left(\frac{\bar{Z}}{2\ell_C} - 2\ell_C\frac{\partial}{\partial Z}\right), \tag{5.37}$$

$$a_r^\dagger = \frac{a_1^\dagger - a_2^\dagger}{\sqrt{2}} = \frac{1}{\sqrt{2}}\left(\frac{\bar{z}}{2\ell_r} - 2\ell_r\frac{\partial}{\partial z}\right), \tag{5.38}$$

where $\ell_C = \ell/\sqrt{2}$ and $\ell_r = \sqrt{2}\ell$. Under this transformation, the relative and center of mass degrees of freedom decouple. As a result, the eigenstates can be written in terms of the total and relative angular momentum. In particular, for the LLL,

$$|M, m\rangle = \frac{(b_C^\dagger)^M (b_r^\dagger)^m}{\sqrt{M!m!}}\,|0,0\rangle\,, \tag{5.39}$$

where M is the eigenvalue for the z-component of the total angular momentum. This leads to the following expression for the wavefunction:

$$\eta_{M,m}(\boldsymbol{R}, \boldsymbol{r}) = \eta_M^C((R))\eta_m^r((r)) = \frac{(Z/\ell_C)^M}{\sqrt{2\pi\ell_C^2 2^M M!}}\frac{(z/\ell_r)^m}{\sqrt{2\pi\ell_r^2 2^m m!}}\exp\left(-\frac{Z\bar{Z}}{4\ell_C^2} - \frac{z\bar{z}}{4\ell_r^2}\right). \tag{5.40}$$

In this basis, the Coulomb interaction Hamiltonian has a simple form. Assuming the interaction only depends on the distance between particles, then we have for

the interaction matrix elements

$$\langle M', m'| V(|\boldsymbol{r}_1 - \boldsymbol{r}_2|) |M, m\rangle = \delta_{M',M}\delta_{m',m} \langle m| V(r) |m\rangle . \tag{5.41}$$

This simple form is a result of momentum conservation. Thus the interaction Hamiltonian becomes

$$\begin{aligned} \mathcal{P}_{\mathrm{LLL}} V(|\boldsymbol{r}_1 - \boldsymbol{r}_2|)\mathcal{P}_{\mathrm{LLL}} &= \\ &= \sum_{M,m} \langle m| V(r) |m\rangle |M, m\rangle \langle M, m| \\ &= \sum_{M,m} V_m P_{M,m}, \end{aligned} \tag{5.42}$$

where $V_m = \langle m| V(r) |m\rangle$ are the so-called Haldane pseudopotentials and $P_{M,m}$ is the projection operator onto the state with total momentum M and relative angular momentum m in the LLL. The pseudopotentials in the LLL can be determined from the wavefunctions given in Eq. (5.40):

$$\begin{aligned} V_m &= \frac{e^2}{\epsilon\ell} \int d^2\boldsymbol{r} \frac{1}{r} |\eta^r_m(\boldsymbol{r})|^2 \\ &= \frac{e^2}{2\epsilon\ell} \frac{\Gamma(m + \frac{1}{2})}{\Gamma(m+1)}. \end{aligned} \tag{5.43}$$

The pseudopotentials provide a very useful alternative to the real space potential, $V(r)$, in describing the interaction strength that is convenient for numerical calculations and obtaining trial wavefunctions. The particular numerical values for the pseudopotentials has inspired various "toy" models which are easier to describe analytically. A particularly famous example of this is the "hardcore" potential,

$$\hat{H}^{(q)}_L = \sum_{m}^{q-2} \sum_{i<j} P_m(m_{ij}). \tag{5.44}$$

where $P_m(m_{ij})$ projects onto states where particles i and j have relative angular momentum $m_{ij} = m$. (Note that for spinless fermions, the pseudopotentials for even m are irrelevant due to the exclusion principle). This model effectively assumes that $V_m = 1$ for $m < q$ and zero otherwise (this is in units where $e^2/\epsilon\ell = 1$). This model is motivated by the fact that the LLL pseudopotentials decrease considerably with m. The exact solution for the ground state of this potential is the famous Laughlin wavefunction at filling fraction $\nu = 1/q$. Also, a similar 3-body model can be arrived at that results in the MR Pfaffian [123]:

To study higher Landau levels, we note that the problem of particles in the nth Landau level with interaction potential, $V(r)$ can essentially be simulated in the LLL where particles are interacting with an effective potential, $V_{\text{eff}}(r)$ that satisfies

$$\langle n, m_1', m_2'| V(|\boldsymbol{r}_1 - \boldsymbol{r}_2|) |n, m_1, m_2\rangle = \langle m_1', m_2'| V_{\text{eff}}(|\boldsymbol{r}_1 - \boldsymbol{r}_2|) |m_1, m_2\rangle . \quad (5.45)$$

This argument essentially says that Landau level subspaces, at least in planar systems, are mathematically equivalent. The effective potential can be found in Fourier space (see Ref. [115] for details) by the expression

$$V_{\text{eff}}(k) = \left(L_n\left(\frac{k^2}{2}\right)\right)^2 V(k), \quad (5.46)$$

where $V(k)$ is the Fourier transform of the Coulomb interaction (i.e. $1/k$ in 2D in units of $e^2/\epsilon\ell$), and L_n are the Laguerre polynomials. Thus, the psuedopotentials for the nth Landau level are given by the integral

$$V_m^{(n)} = \int_0^\infty dk \left(L_n\left(\frac{k^2}{2}\right)\right)^2 L_m(k^2) e^{-k^2}. \quad (5.47)$$

The Haldane pseudopotentials in the spherical geometry are similarly defined.

In this case, the two particle matrix element can be written as

$$\langle Qm_1', Qm_2'| V(r) |Qm_1, Qm_2\rangle = \sum_{L=0}^{2Q} \sum_{M=-L}^{L} \langle Qm_1', Qm_2'|LM\rangle V_L \langle LM|Qm_1, Qm_2\rangle. \tag{5.48}$$

The spherical Haldane pseudopotentials,V_L, in the LLL are given by (see Ref. [117] for details):

$$V_L = \frac{e^2}{\epsilon}\frac{2}{R}\frac{\binom{4Q-2L}{2Q-L}\binom{4Q+2L+2}{2Q+L+1}}{\binom{4Q+2}{2Q+1}^2} \tag{5.49}$$

In general, the spherical pseudopotentials differ only "slightly" from the planar pseudopotentials. In particular, $V_m = V_L$ in the thermodynamic limit. As a result, planar pseudopentials are often used in spherical geometries.

5.5 The Quasi-2D Coulomb Potential

In all of our discussions of the quantum Hall effect in the previous sections, we have assumed that the electrons exist in a purely 2D system. Of course, the full 3D description of a 2DEG is slightly more complicated. Although the movement of electrons along the perpendicular axis (i.e. the z direction) is, indeed, frozen for 2DEG's under typical experimental conditions, the quantum well the electrons reside in has a non-zero thickness. This finite thickness essentially smears the charge of the electron over the extent of the quantum well. As a result, the effective interaction between electrons differs somewhat from the purely 2D Coulomb potential. This deviation is often referred to as the quasi-2D potential, or the finite thickness effect[124, 125, 126, 127].

A straight forward model of the finite thickness effect can be obtained by

treating the quantum well in the z-dimension as an infinite square well. Then an effective Coulomb potential can be obtained by averaging over the single particle ground state (i.e., $n(z) = \sqrt{2/d}\cos(\pi z/d)$), in the perpendicular dimension, where d is the effective thickness of the layer. This gives for the the effective interaction potential (given in Fourier space)

$$\begin{aligned} V_{SQ}(k) &= \frac{e^2}{\epsilon l}\frac{1}{k}\int dz_1 dz_2 |n(z_1)|^2 |n(z_2)|^2 e^{-k|z_1-z_2|} \\ &= \frac{e^2 l}{\epsilon k}\frac{\left\{3kd + \frac{8\pi^2}{kd} - \frac{32\pi^4(1-e^{-kd})}{(kd)^2[(kd)^2+4\pi^2]}\right\}}{(kd)^2+4\pi^2}. \end{aligned} \tag{5.50}$$

There are other models that account for the finite layer thickness for different confinement potentials (e.g. triangular confinement as appropriate in a heterostructure) [124, 125, 126, 127], however, these models all provide similar qualitative results [128, 129]. So for qualitative studies, the square well potential is often adequate, although for precise quantitative accuracy (or for comparison with experimental data) more refined quasi-2D models may be necessary..

Chapter 6

Entanglement Measures of Quasi-2D Fractional Quantum Hall States

In Chapter 1 we discussed how the quantum Hall effect is an example of a "topological" phase of matter where the many-body groundstates have non-trivial topological structures. And these topological properties have consequences that can be probed experimentally. The fractional charge of excitations, for example, has been experimentally verified for several fractions [130, 131]. Also anyonic braiding statistics have also claimed to have been observed for some fractions [132]. However, these experimentally accessible properties can not, in some cases, uniquely determine the true nature of the underlying quantum Hall state and its topology. The prime example of this is the case of $\nu = 5/2$. Several experimental results such as the fractional charge of excitations [76, 80, 81, 77, 78, 79] and the observation of an excited neutral mode [82, 83, 84] are consistent with the Moore-Read theory for this state, but these experiments neither verify nor rule out the existence of non-Abelian anyons. Thus for several FQHE states, particularly $\nu = 5/2$, we must rely on theoretical tools to probe certain aspects of their topological structures.

A particularly straightforward theoretical probe for FQHE states is calculation of the overlap integral between a numerically obtained ground state and a trial wavefunction. This method has proven to be a very powerful tool in numerical investigations of FQHE states. In fact, the wide acceptance of the Laughlin wave-

function (and others) is almost entirely due to results with the overlap (e.g. an overlap of 0.9964 for $\nu = 1/3$ was calculated with the Laughlin wavefunction of 7 electrons [117]). However, initial results on the $\nu = 5/2$ state showed modest overlap with the MR Pfaffian (e.g. 0.8674 for 8 electrons [133]). But subsequent studies have shown that this overlap can be improved by certain alterations of the interaction potential. An especially interesting example of this is a study reported in Ref. [129] which showed that when the finite thickness effect is taken into account (see section 5.5), the overlap is near unity for some optimal value of the thickness, d, of the 2DEG. Additionally, this "strengthening" of the overlap with d appears to be a feature of second Landau level (SLL) states. States in the LLL show the opposite behavior. But we must exercise caution in interpreting results on the overlap since it is not a definitive confirmation of a trial wavefunction and it can be misleading in some cases. An example of this involves the $\nu = 2/5$ state that has been shown to have a large overlap with both the Jain composite fermion wavefunction as well as the so-called "Gaffnian" wavefunction, even though these two states have different underlying topological orders [134, 135]. The problem here is that the extrapolation to the thermodynamic limit from finite size overlap calculations may be non-unique or simply unknown. Thus we seek alternative theoretical tools that would, ideally, be able to distinguish topological order within numerically obtained groundstates.

Recently, several studies have shown that measures of entanglement within many-body groundstates can reveal certain aspects of the underlying topological order. One of the most common entanglement measures that is used in this regard is the bipartite entanglement entropy. The entanglement entropy (EE), generally

speaking, measures the extent to which degrees of freedom are entangled in a bipartioned system[136] and has proven to be a very powerful tool in examining quantum correlations in interacting many-body systems[137, 138]. Also, the EE can be used to calculate a topological invariant known as the "topological entanglement entropy" which is an indicator of topological order[139, 140], although the measure can be ambiguous in some cases. An alternative to the EE, which is commonly known as the "entanglement spectrum" (ES), directly examines the eigenvalues of the reduced density matrix and reportedly offers more information about the underlying topology than the EE alone. In this chapter, we examine these tools (the EE and ES) and apply them to numerically obtained FQHE states. We do this while varying the thickness, d, of the Coulomb interaction in the finite thickness effect in order to tease out possible Landau level dependence in the same spirit as Ref. [129]. This work is also provided in Ref. [141].

6.1 Entanglement Measures Overview

6.1.1 Entanglement Entropy

The entanglement entropy is defined as the the von-Neuman entropy,

$$S_E(\rho_A) = \mathrm{Tr}[\rho_A \ln \rho_A] \tag{6.1}$$

of the reduced density matrix $\rho_{A/B} = \mathrm{Tr}_{B/A}[|\Psi\rangle \langle\Psi|]$ for state $|\Psi\rangle \in \mathcal{H} = \mathcal{H}_A \otimes \mathcal{H}_B$ in a Fock space $\mathcal{H}$ that has been partitioned into two parts. The partitioning of $\mathcal{H}$ can be any division of the degrees of freedom, but is often done in real space where

the physical space is effectively divided into two equal (or almost equal) parts. In this case, the EE is sometimes referred to as the spatial entanglement entropy. The spatial EE has been shown to have the following form:

$$S_E(\rho) = \alpha L - \gamma + \mathrm{O}(L^{-1}). \tag{6.2}$$

where L is the area (length) of the boundary between the two partitions. The first term in the expression reflects the "area law"[136, 137] where the EE is expected to scale linearly with the boundary area. The coefficient, α, is nonuniversal, but the constant term, γ, has been shown to be a topological invariant. In particular, γ is related to the "total quantum dimension", $\mathcal{D}$, by the relation

$$\gamma = \ln \mathcal{D}, \tag{6.3}$$

where

$$\mathcal{D}^2 = \sum_a d_a^2, \tag{6.4}$$

and d_a is the quantum dimension of the quasiparticle of type a. The quasiparticle types and their respective quantum dimensions can be derived from the fusion rules of the anyon model that describes the excitations. A good review of this topic can be found in Ref. [24]. For Laughlin states at filling fraction $\nu = 1/q$, $\mathcal{D}^2 = q$ for odd q. For the MR Pfaffian, $\mathcal{D}^2 = 4q$ for filling fraction $\nu = 1/q$ with q even.

The topological EE in a 2D system can be obtained, generally speaking, by dividing the medium into several partitions, calculating the EE of these partitions, and summing them in such a way that the αL term cancels (details can be found in Ref. [142]). This kind of partitioning, however, is not possible in FQHE states since

the Landau level basis does not have two spatial degrees of freedom. An alternative approach is to calculate $S(\rho_A)$ at different partition sizes and system sizes to estimate α in the thermodynamic limit. This has been attempted in Refs. [143], [144], and [145]. Their results are consistent with the Laughlin and MR Pfaffian descriptions for $\nu = 1/3$ and $\nu = 5/2$ respectively (although Ref. [144] had the interesting conclusion that $\nu = 7/3$ was more consistent with the $k = 4$ Read-Rezayi state [146] instead of the Laughlin state) however they are not definitive since the extrapolation process inevitably introduces numerical errors. In this chapter, we do not attempt to calculate γ. Instead we examine the EE in finite systems with respect to the quasi-2D thickness. This study is exploratory in the sense that we seek to learn what can be gleaned from the EE alone about the nature of FQHE states.

6.1.2 Entanglement Spectrum

The entanglement spectrum (ES) attempts to tease out more information from the reduced density matrix than the von-Neuman entropy alone. Consider again the many-body non-degenerate groundstate, $|\Psi\rangle$ of the Hamiltonian, H and the reduced density operator, $\rho_A = \mathrm{Tr}_B[|\Psi\rangle \langle\Psi|]$ for the partition $\mathcal{H} = \mathcal{H}_A \otimes \mathcal{H}_B$. In Ref. [147], Li and Haldane suppose that the reduced density matrix can be associated with a system governed by a separate hermitian Hamiltonian, $\widehat{H}$, at finite "temperature", $T = 1$. In other words, the reduced density matrix can be written as

$$\rho_A = e^{-\widehat{H}}. \tag{6.5}$$

In this form, Li and Haldane conjecture that the Hamiltonian, $\widehat{H}$, is in the same universality class (i.e. has the same topological structure) as the original Hamiltonian of the full system, H. Therefore we can study topological properties of the original Hamiltonian through $\widehat{H}$, or by extension, the reduced density matrix. What makes the Li-Haldane conjecture (and to a lesser extent, the topological EE) quite remarkable is that topological aspects of H can essentially be inferred by studying the groundstate alone. Since this conjecture was initially made in Ref. [147], several studies have followed that support it [148, 149, 150, 151, 152, 153].

When applied to FQHE states, the structure of the entanglement spectrum appears to follow the so-called "Haldane exclusion statistics" of FQHE states [154]. The Haldane exclusion statistics are topological properties of FQHE states that can be thought of as a generalized version of Fermi statistics. To illustrate Haldane statistics, consider the many-body wavefunction in the spherical geometry $|\Psi\rangle = |n_{m_1}, n_{m_2}, n_{m_3}, ...n_{m_{\max}}\rangle$ where n_{m_i} is the number of particles in the m_i orbital, $m_i < m_{i+1}$. For spinless fermions, Fermi statistics tells us that no more than one particle can be in any single orbital (i.e. $n_{m_i} \leq 1$). In the thermodynamic limit, Haldane showed that for Laughlin states at $\nu = 1/q$, the occupation of orbitals follow a stronger restriction where no more than one particle is allowed within a set of q consecutive orbitals. For example, for $q = 3$, $|1, 0, 0, 1, 0, 0, 1, 0, 0\rangle$ is allowed, but $|1, 0, 1, 0, 0, 0, 1, 0, 0\rangle$ is not. The Haldane statistics are very useful in the counting of quasihole states and is topological in origin [154]. The MR Pfaffian state follows similar exclusion rules where a set of 4 consecutive orbitals can have no more than 2 particles.

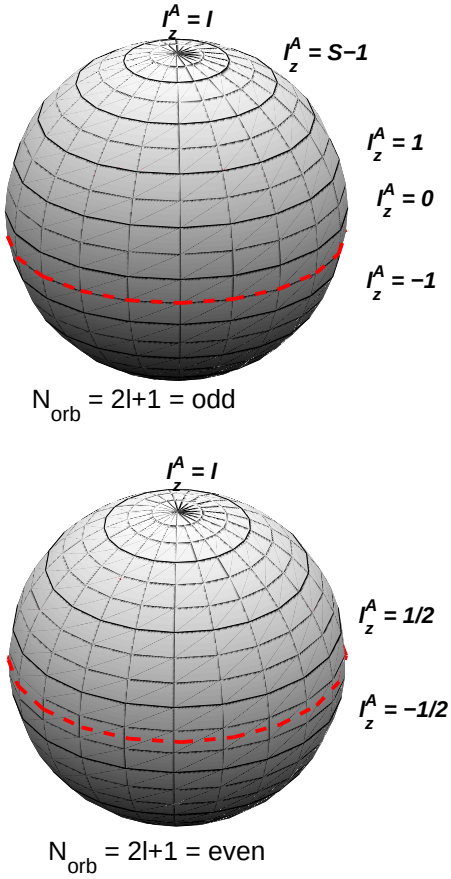

Figure 6.1: Graphical illustration of the partitioning of the Fock space. In the spherical geometry, the single-particle states are states with the z-component of angular momentum from l to $-l$, represented by the solid latitudinal lines. We choose our partitions to cut the sphere in two as close to the equator as possible, represented by the dashed lines. Thus, for $N_{\mathrm{orb}} = 2l + 1$ even, we cut the sphere after $N_{\mathrm{orb}}/2$ (see top panel) and after $(N_{\mathrm{orb}} + 1)/2$ for N_{orb} odd (see bottom panel).

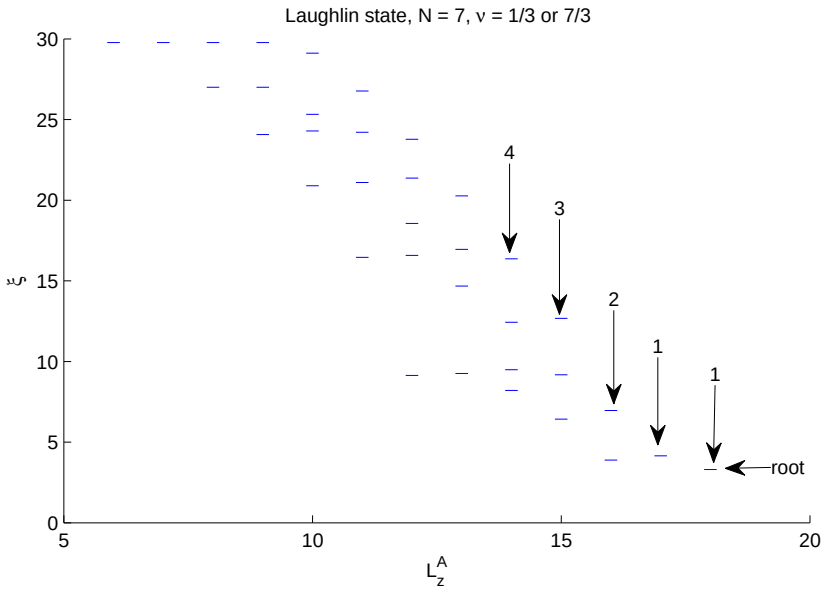

Figure 6.2: The entanglement spectrum of the Laughlin wavefunction with $N = 7$ particles in the spherical geometry with respect to $\left|L_z^A\right|$. The cut is chosen so that $N_{\text{orb}}^A = 10$. The state corresponding to the root configuration is denoted. Also the number of states is also shown for several values of $\left|L_z^A\right|$ up to $\Delta L = L_z^A - L_{z,\text{root}}^A = 4$ is shown. At $\Delta L = 4$, the number of states (4) differs from that expected from Haldane statistics (5).

To illustrate how Haldane statistics manifest in the entanglement spectrum, we take the Laughlin state at $\nu = 1/3$ in the spherical geometry, partition the sphere in half and calculate $\xi_i = 2\ln(|\rho_i|)$ where ρ_i is the i-th eigenvalue of the reduced density matrix. In splitting the sphere, we note that in the LLL, the single particle L_z orbitals are well localized about regularly spaced latitudinal lines on the sphere (see Fig. 6.1). Thus we can partition the sphere into two sections by writing our Fock space as $\mathcal{H} = \mathcal{H}_A \otimes \mathcal{H}_B$ with respective basis states

$$\left|\psi_A^j\right\rangle = \left|n_{-l}^j, n_{-l+1}^j \ldots n_{-l+N_{\text{orb}}^A-1}^j\right\rangle \in \mathcal{H}_A \tag{6.6}$$

$$\left|\psi_B^k\right\rangle = \left|n_{l-N_{\text{orb}}^B}^k, n_{l-N_{\text{orb}}^B+1}^k \ldots n_l^k\right\rangle \in \mathcal{H}_B \tag{6.7}$$

where $N_{\text{orb}}^A + N_{\text{orb}}^B = N_{\text{orb}} \equiv 2l+1$ is the total number of Landau level orbitals. Since

the quantum numbers for angular momentum and particle number in each region, L_z^A, L_z^B, N^A, N^B, are constrained such that $L_z^A + L_z^B = L_z = 0$ and $N^A + N^B = N$, the reduced density matrix is block diagonal with L_z^A and N^A being good quantum numbers for the eigenstates of ρ_A. Therefore L_z^A and N^A are good labels for the corresponding entanglement spectrum. In Fig. 6.2, we show the result for the ES with respect to L_z^A of the Laughlin state with $N = 7$ electrons, $N_{\text{orb}}^A = 10$, and $N^A = 4$. In the figure, we see a very sparse pattern of states. According to Li-Haldane, the counting of these states follows Haldane statistics. To see this, we note that for the full system, $N_{\text{orb}} = 19$ and Haldane statistics tells us that the ground state configuration is '1001001001001001001' with total $L_z = 0$. After tracing out the degrees of freedom in the B partition, we are left with a hemisphere that has an edge. Thus, in this reduced geometry, we can expect to see edge excitations about the partitioned ground state, '1001001001', with $\left|L_z^A\right| = 9 + 6 + 3 + 0 = 18$. This is the "root configuration" and has the maximal value for $\left|L_z^A\right|$ and corresponds to the state seen in Fig. 6.2 at $\left|L_{z,\text{root}}^A\right| = 18$. We can determine the edge excitations by adding orbitals to the root configuration and determining the possible states that satisfy the Haldane statistics. The first excitation, for example, is '10010010001' (move the last electron one orbital to the left) with $\left|L_z^A\right| = 9 + 6 + 3 + -1 = 17$ so $\Delta L = L_z^A - L_{z,\text{root}}^A = 1$. There is only one state possible with $\Delta L = 1$, so we see only one state in the ES at $L_z^A = 19$. For $\Delta L = 2$ we have two possibilities, '100100100001' and '100100010010'. For $\Delta L = 3$, we have 3 possibilities: '1000100100100', '1001000100010', and '1001001000001'. This counting rule breaks down at $\Delta L = 4$ (we should expect 5 states instead of 4). This breakdown is due

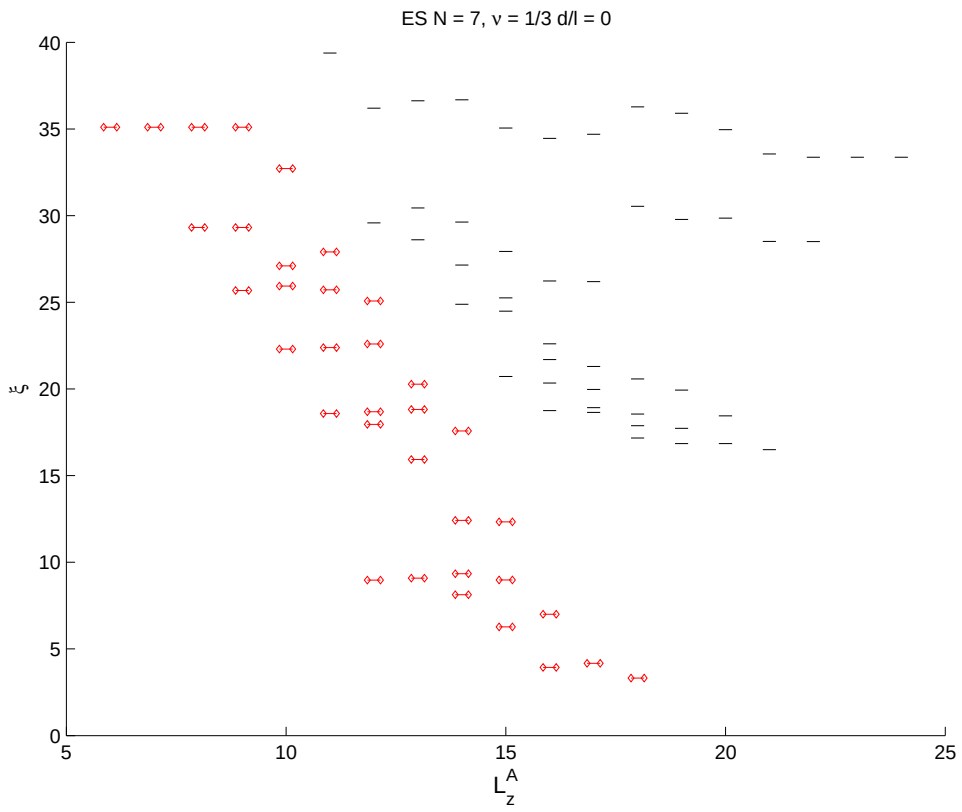

Figure 6.3: The entanglement spectrum of the $\nu = 1/3$ filled FQHE state with $N = 7$ particles in the spherical geometry with respect to $\left|L_z^A\right|$. The cut is chosen so that $N_{\text{orb}}^A = 10$. The lowest "energy" states that match the counting in the ES of the Laughlin wavefunction are marked in red.

to the finite extent of the original system since the counting rule persists longer in larger systems[147], so it is expected to be true in the thermodynamic limit.

When we examine the ES of a FQHE state (i.e. ground state of the LLL projected Coulomb potential), the spectrum is more complicated. The ES of the $\nu = 1/3$ state is shown in Fig. 6.3 for $N = 7$, $N_{\text{orb}}^A = 10$ and $d = 0$. In this case, we see a great deal more states than what is seen in the ES of the Laughlin state. However, for ΔL small, there appears to be low "energy" states that are separated from a band of higher energy states by a gap. Li and Haldane conjecture that these low-lying states are topological and are the same as those that we discussed when

examining the Laughlin state. The higher energy states, however, are generic. Li and Haldane also conjecture that as long as there is an appreciable gap between the low-lying topological states and these generic states, the FQHE state can be said to have the same topology as the Laughlin state. Thus, the size of these gaps in the ES (also called the entanglement gaps) can be thought of as a quantitative measure of how well the $\nu = 1/3$ state fits the Haldane statistics governing the Laughlin state. The closing of these gaps for larger ΔL is conjectured to be due to the finite size of the system. To distinguish the two kinds of states, we call the states that are consistent with the Haldane statistics (and/or with the counting seen in a model wavefunction) "topological" states (these states are also sometimes called "CFT" states since they are consistent with the "conformal field theory" description of the state).

6.1.3 The Conformal Limit

One of the limitations of the ES that is apparent in Fig. 6.3 is that there is not a "full" gap in the spectrum. The entanglement gaps can only be interpreted as a function of L_z^A and, according to Li and Haldane, only the gaps for small values of ΔL have meaning. Thus in general, the ES can only be interpreted if there is a good quantum number in which to interpret the ES and only a portion of the ES has meaning. It has recently been suggested however, that some of the finite size effects can be corrected for, allowing for a full use of the entire ES [155]. This correction, which has been introduced as the "conformal limit", applies specifically to the ES

of states on the sphere. This limit is obtained by expressing the ground state in terms of a special choice of unnormalized basis states. The normalized single particle wavefunction on a sphere in the LLL with angular momentum m is given by Eq. (5.30). In the conformal limit, we "unnormalize" the single particle wavefunctions by removing the prefactor in Eq. (5.30) such that the wavefunctions take the simple form $\Psi'(u,v) = u^{l+m}v^{l-m}$. This procedure is an attempt at removing the finite size effects inherent in these calculations by basically removing the "length" in the problem. With the ground state redefined in this new basis, the entanglement spectrum is calculated in the usual way. Examples of this are given in section 6.2.4.

6.2 Numerical Results for Quasi-2D FQHE States

6.2.1 Method

In this study, we consider the FQH ground states at the Laughlin filling fractions $\nu = 1/3$ and $\nu = 7/3$ with particle number $N = 6$, 7, and 8 and the even-denominator filling fractions $\nu = 1/2$ and $\nu = 5/2$ with particle number $N = 8$ and $N = 10$. We restrict ourselves to these relatively modest system sizes in order to investigate a large number of FQH ground states for various values of the finite thickness d/ℓ with reasonable computing resources. Although the Hilbert space for particle number $N = 12$ at the half fillings is not prohibitively large, this system is also aliased with $\nu = 2/3$ and could, therefore, yield ambiguous results. Since we are largely concerned with the qualitative features of the finite-thickness effect, these system sizes are adequate. We diagonalize the FQH Hamiltonians (one for each d/ℓ

and LL index n) in the spherical geometry[116] where N electrons are confined to the surface of a sphere. Although we use this geometry, we use the pseudopotentials obtained from the infinite planar geometry (Eq.(5.47)) since the finite layer thickness effect is more conveniently modeled in this case. Furthermore, the pseudopotentials in the spherical geometry equal those in the planar geometry as the thermodynamic limit is approached (as the spherical radius is taken to infinity) and it can be argued that they provide a better approximation to the thermodynamic limit (this is discussed in detail in Ref. [129] and in section 6.2.6). To model the finite thickness effect, we use the Coulomb potential derived from the infinite square well potential (Eq. (5.50)).

We calculate the entanglement entropy (EE) and the entanglement spectrum (ES) of FQH ground states by dividing the sphere into two regions as given in Eqs. (6.7) and (6.7). For all cases we choose our partitions when dividing our Fock space $\mathcal{H}$ into $\mathcal{H}_A$ and $\mathcal{H}_B$ such that for the number of single particle orbitals $N_{\rm orb} = 2l+1$ even, $N^A_{\rm orb} = N^B_{\rm orb} = N_{\rm orb}/2$ and for $N_{\rm orb}$ odd, $N^A_{\rm orb} = N^B_{\rm orb} + 1 = (N_{\rm orb}+1)/2$. Geometrically this is equivalent to dividing the sphere along a line of latitude (see Fig. 6.1).

6.2.2 Entanglement Entropy

We now report numerical results for the entanglement entropy (EE) of quasi-2D FQH ground states as a function of the finite layer thickness d/ℓ for FQH states in the LLL ($\nu = 1/3$ and $1/2$) and the SLL ($\nu = 2+1/3 = 7/3$ and $2+1/2 = 5/2$).

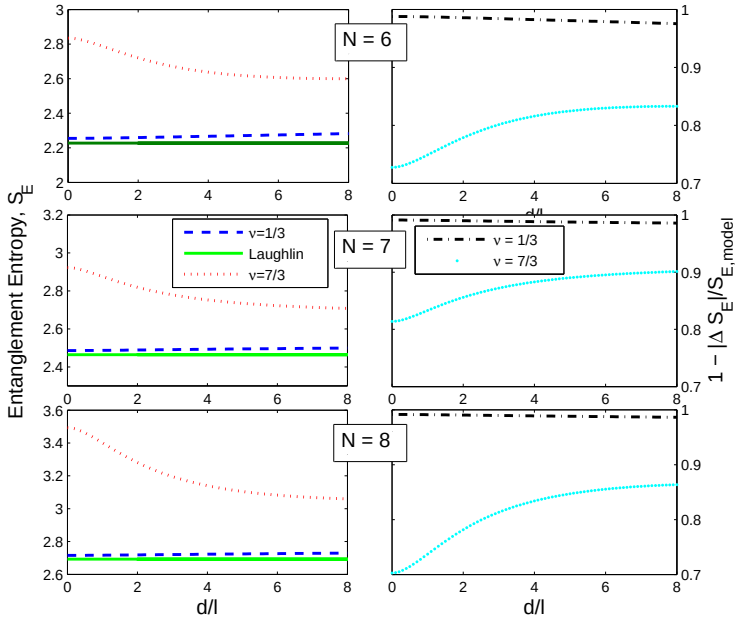

Figure 6.4: Entanglement entropy S_E as a function of finite layer thickness, d/ℓ for Laughlin filling fractions $\nu = 1/3$ and $\nu = 7/3$ for particle number $N = 6$, 7 and 8. The dashed and dotted lines in the left panels correspond to the Coulomb Hamiltonian of a quasi-2D system in the LLL and SLL, respectively, while the solid lines in the left panels corresponds to the finite size Laughlin states. The plots in the right panels give one minus the percentage difference in the Coulomb EE and the model state EE, i.e., $1 - |\Delta S_E|/S_{E,\text{model}}$ in the LLL (dash-dotted line) and the SLL (dotted line) and are found to be similar qualitatively and quantitatively to overlap calculations [156, 127, 128, 129].

As mentioned above we choose the partition to be as close to the equator of the sphere as possible to minimize finite size effects.

The results for EE for the Coulomb ground state at filling fractions $\nu = 1/3$ and $\nu = 7/3$ are shown in Fig. 6.4 as a function of finite layer thickness d/ℓ. For comparison, the EE of the corresponding Laughlin model wavefunction is also shown as a d/ℓ independent horizontal line. In each of the figures, we see that in the LLL, the EE is near that of the Laughlin model wavefunction at $d = 0$ and rises slightly as a function of d/ℓ. In contrast, the EE in the SLL is large compared to that of the

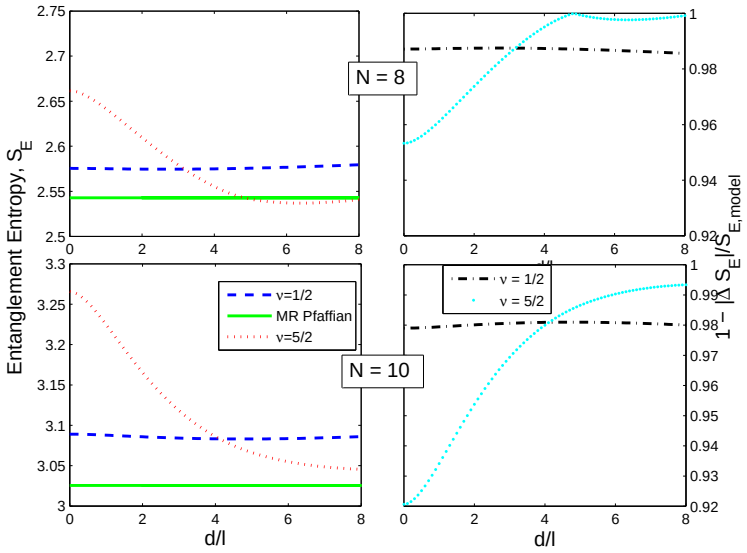

Figure 6.5: (Color online) Entanglement entropy S_E as a function of finite layer thickness, d/ℓ for even-denominator filling fractions $\nu = 1/2$ and $\nu = 5/2$ for $N = 8$ and 10. Similar to Fig. 6.4 the plots in the right panels give one minus the percentage difference between S_E and $S_{E,\mathrm{model}}$.

Laughlin model at $d = 0$, but decreases as a function of d/ℓ and evidently reaches an asymptotic value. The qualitative behavior is independent of system size. If we consider $\Delta S_E = S_E - S_{E,\mathrm{model}}$ for both the LLL and SLL filling fractions and speculate that ΔS_E is a qualitative measure of how far removed the ground state is from the Laughlin model state, then we see that the LL dependence of ΔS_E as a function of d/ℓ behaves qualitatively similar to that of the overlap between the ground state and the model wavefunction as reported in Ref. [156, 127, 128, 129]. In particular, the ground state in the LLL is a "strong" FQHE state (i.e., ΔS_E is small) at $d = 0$ and gradually becomes "weaker" for increasing d/ℓ (albeit only slightly), whereas in the SLL, the ground state is initially weak at $d = 0$ but gets stronger with increasing d/ℓ (i.e., ΔS_E decreases). Thus, the EE for these cases qualitatively and semi-quantitatively captures how well the states are "Laughlin-like" as a function

of d/ℓ in similar manner to the overlap.

Our operational definition of "weak" and "strong" depends on how close the EE of the Coulomb state is to the model state which, in this case, is the Laughlin state. In the SLL, S_E becomes closer to the S_E for the Laughlin state but, as mentioned above, appears to saturate at some asymptotic value that is still nearly $\sim 1.1 S_{E,\text{Laughlin}}$. In contrast, the EE in the LLL is almost identical to that of the Laughlin state. We conjecture as to the reason for this difference between the EE in the SLL Coulomb ground state compared to the Laughlin state and the difference between the EE in the LLL as compared to the SLL: (i) it is possible that the FQHE at 7/3 is *not* described by the Laughlin state and is instead described by a state in a different topological universality class such as those given by Read and Rezayi [146] and Bonderson and Slingerland [157], (ii) perhaps composite fermion interactions, which are thought [158] to be more relevant in higher LLs, are producing this difference in S_E and the Laughlin state, (iii) perhaps the 7/3 FQHE state is in fact a Laughlin state but our model system is leaving out realistic effects such as LL mixing which are crucial to its success.

Fig. 6.5 gives results for the EE of FQH ground states with even denominator filling fractions $\nu = 1/2$ and $5/2$ as a function of finite layer thickness d/ℓ. Also shown in the figure is the EE of the Moore-Read Pfaffian state for comparison. In the LLL ($\nu = 1/2$), the EE has a weak minima as a function of d/ℓ, in contrast to the Laughlin fractions (this minimum is difficult to discern on our scale). The location of this minima changes with N, suggesting a finite size effect, but the qualitative behavior is similar in both cases. In the SLL ($\nu = 5/2$), the EE has a

very pronounced minima that approaches the EE of the MR Pfaffian model state for $N = 10$ and crosses it for $N = 8$. This suggest that the FQH states becomes more MR Pfaffian-like at near an optimal d/ℓ. However, this optimal d/ℓ also changes with N. Similar to the Laughlin fractions, this LL dependence in EE as a function of d/ℓ is also qualitatively similar to that seen in the overlap between the FQH ground states and MR Pfaffian reported in Ref. [128, 129]. These results suggest that $\nu = 1/2$ is not particularly well-described by the MR Pfaffian, whereas $\nu = 5/2$ is better described by the MR Pfaffian model state at finite thickness.

We note that recently, entanglement entropy in the SLL including finite thickness effects has been investigated [144, 145]. However, the previous study did calculations using the torus geometry, in contrast to our spherical geometry, and attempted to isolate and calculate the topological entanglement entropy. The conclusion of Refs. [144, 145] was that the topological entropy of the ground states of the LLL or SLL Coulomb Hamiltonians was consistent with associated model states (we note, however, that in Ref. [144] it was concluded that $\nu = 7/3$ was more consistent with the $k = 4$ Read-Rezayi state [146] instead of the Laughlin state). However, they also included finite thickness in the form of an infinite square well potential and, interestingly, found that there was not much difference between the EE and the topological entropy with or without finite thickness included. We, however, clearly see a finite thickness effect on the EE. It is possible that this difference in the two studies (our present study and Refs.[144, 145]) is due to the different geometry used in the calculations (sphere vs. torus) but we find this scenario unlikely since most quantities of interest produce consistent results in the two geometries [159, 128, 129].

Such a comparison between geometries (torus vs sphere) was shown in Ref. [160] to give similar results for the entanglement spectra of Laughlin states, supporting our suspicion. Also results given in Ref. [161] suggests that the the extrapolation procedure performed in Refs. [144, 145] may have been inappropriate for the torus. More work is clearly necessary in understanding the difference between the results in spherical and toroidal geometries, particularly in the presence of the realistic finite thickness effects.

Before moving on to entanglement spectra we briefly discuss how our results compare to the previous overlap calculations done in Refs. [128, 129]. The right panels in Figs. 6.4 and 6.5 gives one minus the percentage error in the entanglement entropy, $1 - |\Delta S_E|/S_{E,\text{model}}$. In Ref. [129] it is found that the overlap between the Laughlin state and the Coulomb ground state at 1/3-filling in the LLL and SLL is approximately ~ 0.99 at $d/\ell = 0$ and is reduced monotonically to ~ 0.98 at $d/\ell = 8$ in the LLL and is ~ 0.73 at $d/\ell = 0$ and has a maximum of ~ 0.84 for $d/\ell \sim 4$ in the SLL. These overlap trends are very consistent with what we have seen previously in EE. For the 1/2-filled LLL and SLL we find [128, 129] the overlap is relatively constant in the LLL at ~ 0.9 and in the SLL it is ~ 0.96 at $d/\ell = 0$ and has a maximum value of nearly ~ 1 at $d/\ell \sim 4$. Again, one minus the percentage error in the entanglement entropy tracks the behavior in the overlap to a remarkable degree. Perhaps this is not a surprise since if the overlap $\langle \Psi_0 | \Psi_{\text{model}} \rangle$ is close to one then the EE (which is a particular combination of $|\Psi\rangle\langle\Psi|$) should also be nearly identical to the EE of the model state Ψ_{model}.

6.2.3 Entanglement Spectrum

In the previous section, we saw that the entanglement entropy S_E (and in particular, ΔS_E) as a function of d/ℓ behaves qualitatively similar to the overlap [128, 129]. For the half-filled case, increasing d/ℓ makes the calculated S_E closer to the MR Pfaffian state for the SLL ($\nu = 5/2$) in a rather dramatic way while increasing d/ℓ has very little effect on the S_E in the LLL ($\nu = 1/2$), i.e., using the entanglement entropy as a measure we see that the MR Pfaffian is *stabilized* by finite thickness. For the 1/3-filled case we find that increasing d/ℓ drives S_E away from the Laughlin value in the LLL ($\nu = 1/3$) and closer to the Laughlin value in the SLL ($\nu = 7/3$), however, as in the previous overlap investigations, the value of the entanglement entropy for the 7/3 case never gets as close to the Laughlin value as the 5/2 entanglement entropy gets to the MR Pfaffian. As discussed above, this could be a hint that something is missing from our understanding of the physics for the FQHE at $\nu = 7/3$.

To gain a deeper understanding of entanglement, we now turn our attention to the finite layer thickness dependence of the entanglement spectrum (ES), which as discussed earlier, provides more information than the EE alone. To calculate the ES, we partition the sphere the same as was done for the EE. We follow the convention established by Li and Haldane[147] and restrict ourselves to the part of the ES where the number of particles in the A partition, N^A, is the same as that of the "root" configuration for the corresponding Laughlin or Moore-Read Pfaffian model wavefunction[162, 147] for a given partition size $N^A_{\rm orb}$. The "root" configurations

FQH state	$N^A_{\rm orb}$	root config.	L^A_z	N^A
Laughlin 1/3,7/3	8	'10010010'	13.5	3
	10	'1001001001'	18	4
	11	'10010010010'	24	4
MR Pfaffian 1/2, 5/2	7	'1100110'	16	4
	9	'110011001'	24.5	5

Table 6.1: Root configurations of the Laughlin ($\nu = 1/3,\ 7/3$) and MR Pfaffian ($\nu = 1/2,\ 5/2$) wavefunctions for the given partition sizes, $N^A_{\rm orb}$, on the sphere. '10010010′, for example, means that the single-particle angular momentum $l = 7.5$, $l - 3 = 4.5$, and $l - 6 = 1.5$ are all occupied with the others unoccupied. Hence, there are $N^A = 3$ electrons with total z-component of angular momentum $L^A_Z = l - 9 = 13.5$ in this root configuation.

describe the occupancy of LL orbitals for MR Pfaffian and Laughlin model states in the thermodynamic limit. Root configurations with a maximum z-component of angular momentum, and their corresponding quantum numbers, N^A and L^A_z, are given in Table 6.1 for different filling fractions and partition sizes.

In order to obtain a general qualitative picture of how the ES changes as a function of the finite layer thickness, we calculate the "entanglement gaps" in each ES and plot it as a function of d/ℓ. An entanglement gap[147] is defined as the difference between the low-lying levels (i.e., those levels displaying the Haldane statistics counting structure discussed in section 6.1.2) and the generic levels for a given value of L^A_z in the spectrum. According to the Li and Haldane conjecture, the state has a non-trivial topology if the entanglement gaps are finite in the thermo-

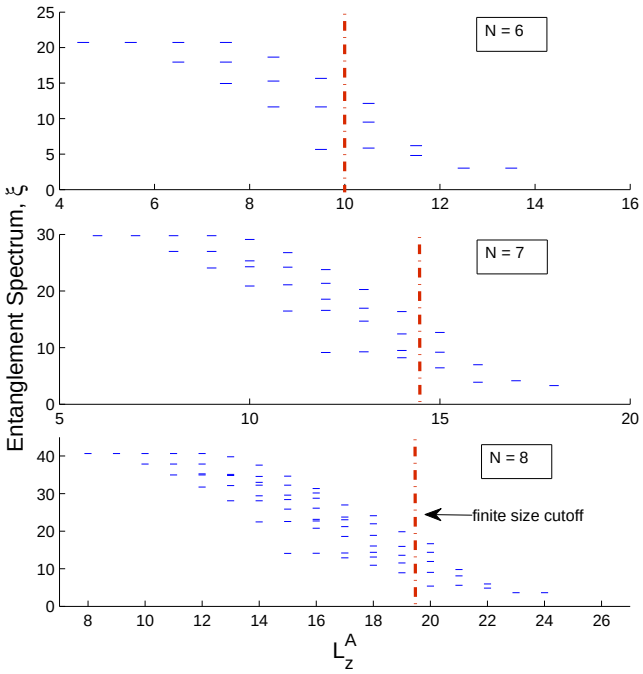

Figure 6.6: Entanglement spectrum of the $\nu = 1/3$ filled Laughlin model state for particle number $N = 6$ (top panel), 7 (middle panel), and 8 (bottom panel). The finite size cutoff used to examine the entanglements gaps is illustrated by the vertical line.

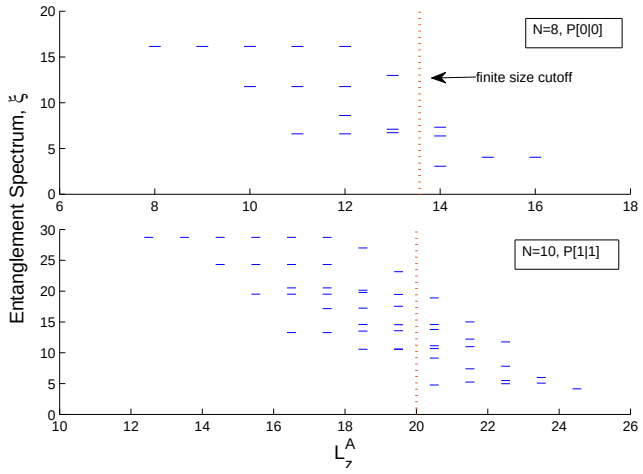

Figure 6.7: Entanglement spectrum of the $\nu = 1/2$ filled MR Pfaffian model state for particle number $N = 8$ (top panel) and 10 (middle panel). The finite size cutoff used to examine the entanglements gaps is illustrated by the vertical line and the particular partition of the Fock space is given using the Li and Haldane notation [147].

dynamic limit. However only the entanglement gaps at relatively "small" values of $\Delta L = L^A_{z,\text{root}} - L^A_z$ are relevant due to finite size effects, where $L^A_{z,\text{root}}$ is the total z-component of angular momentum of the root configuration. The finite number of LL orbitals limits the number of possible "edge excitations." Therefore only a few levels are expected to have the same counting structure as the topological edge modes. The "depth" (i.e., the max ΔL) at which the counting structure in the ES is consistent with the topological edge modes is dependent on the system size, N.

We can determine a suitable cutoff for ΔL by examining when the level counting in the ES of the model states deviate from the expected counting in the thermodynamic limit. To illustrate this finite size cutoff, we give the ES of the Laughlin state in Fig. 6.6. For the Laughlin state, the multiplicity of topological levels is given by $\text{p}(\Delta L)$ where $\text{p}(m)$ is the partition function of the integer m. The first 7 values of $\text{p}(m)$, starting with $m = 0$ are 1, 1, 2, 3, 5, 7, and 11. In Fig. 6.6, we see that for $N = 6$ and 7, the level counting begins to deviate from $\text{p}(\Delta L)$ at $\Delta L = 4$, and for $N = 8$, the deviation begins at $\Delta L = 5$. Thus, for our study we will focus on the entanglement gaps for $\Delta L = 0, 1,$ 2 and 3 for the $N = 6$ and 7 Laughlin systems, and for $N = 8$, we also examine the entanglement gap at $\Delta L = 4$.

We determine the finite size cutoff for the entanglement gaps of the half-filled FQH states in a similar manner, which we now illustrate. The ES for the MR Pfaffian model states are shown in Fig. 6.7. The counting rules for the MR Pfaffian model state depend on where the partition is made, which correspond to choosing one of the three sectors of the corresponding conformal field theory (CFT)[147]. For the case of $N = 8$, the partition along the equator is equivalent to the $P[0|0]$

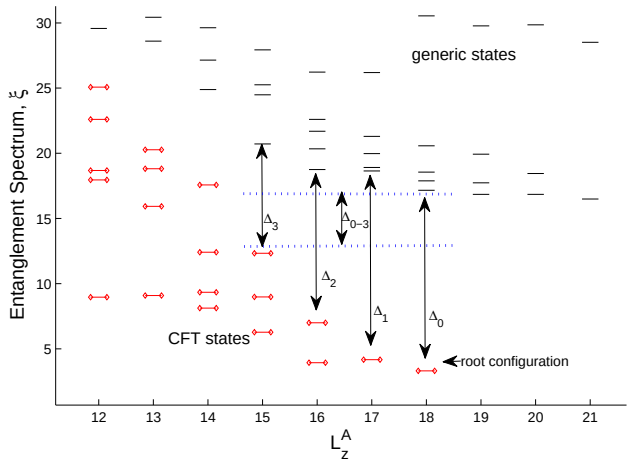

Figure 6.8: Entanglement spectrum for $\nu = 1/3$, $d = 0$, and $N = 7$ as a function of z-component of angular momentum, L_z^A. Suspected topological and generic states are labeled by red and black dashes, respectively. The entanglement gaps are given by the difference between the lowest generic state and the highest topological state for a given value of L_z^A. The minimal gap, Δ_{0-4} is given by the difference between the lowest generic state and the highest topological state for $\Delta L \leq 4$. This minimal gap is represented by the dashed lines.

partition in Li and Haldane's nomenclature (i.e., a cut between two unoccupied orbitals in the root configuration). The level counting for the first 4 levels of this partition are 1, 1, 3, and 5. The counting in the MR Pfaffian ES given in Fig. 6.7 with $N = 8$ deviates from this structure at $\Delta L = 3$. For $N = 10$, the partition along the equator corresponds to $P[1|1]$ (i.e., a cut between two occupied orbitals of the root configuration), which has a level counting of 1, 2, 4, and 7 for the first 4 levels. Examining the ES in the figure for $N = 10$, we see this spectrum also deviates from the expected counting at $\Delta L = 3$. Thus for the half-filled FQH states we examine in this study, we concern ourselves only with the entanglement gaps up to $\Delta L = 2$.

The entanglement gaps, which we denote as Δ_i for $i = \Delta L$, are calculated by finding the difference between the largest suspected topological level and the

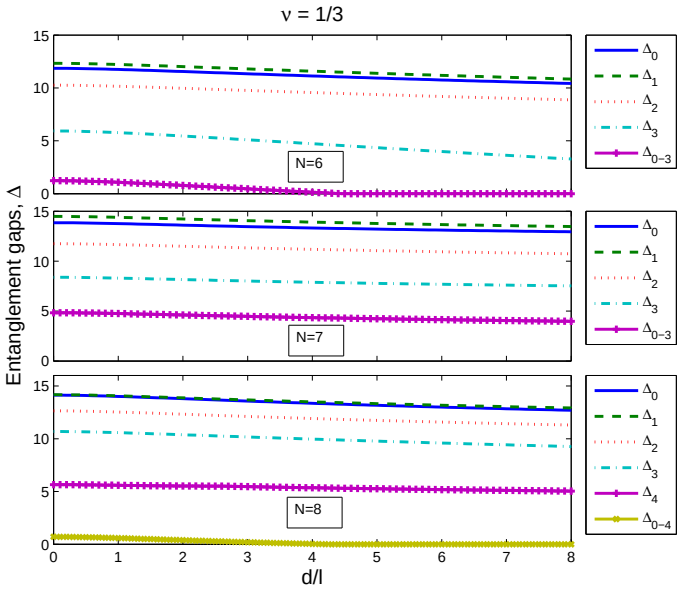

Figure 6.9: Entanglement Gaps for the Coulomb Hamiltonian as a function of finite layer thickness d/ℓ for filling fraction $\nu = 1/3$ and particle number $N = 6$ (top panel), $N = 7$ (middle panel), and $N = 8$ (bottom panel) with partition at the equator.

next highest level at the given value of L_z^A in the ES of the numerically obtained Coulomb ground states for varying d/ℓ. We also calculate the minimal gap between topological and generic levels for $\Delta L \leq m$, which we denote as Δ_{0-m} where m is the cutoff described above. The minimal gap gives us a qualitative measure of how well separated, overall, the topological levels are from the generic levels. The suspected topological levels are identified by the expected counting described above. An example of this procedure is shown in Fig. 6.8, which shows the entanglement gaps in the ES of the $\nu = 1/3$ ground state for $d = 0$ and $N = 7$. Note that throughout this work, when presenting figures showing ES, we color code the suspected topological levels with red diamonds connected by a red dash and all other ES levels with a black dash. The topological levels are chosen by calculating the ES for the model

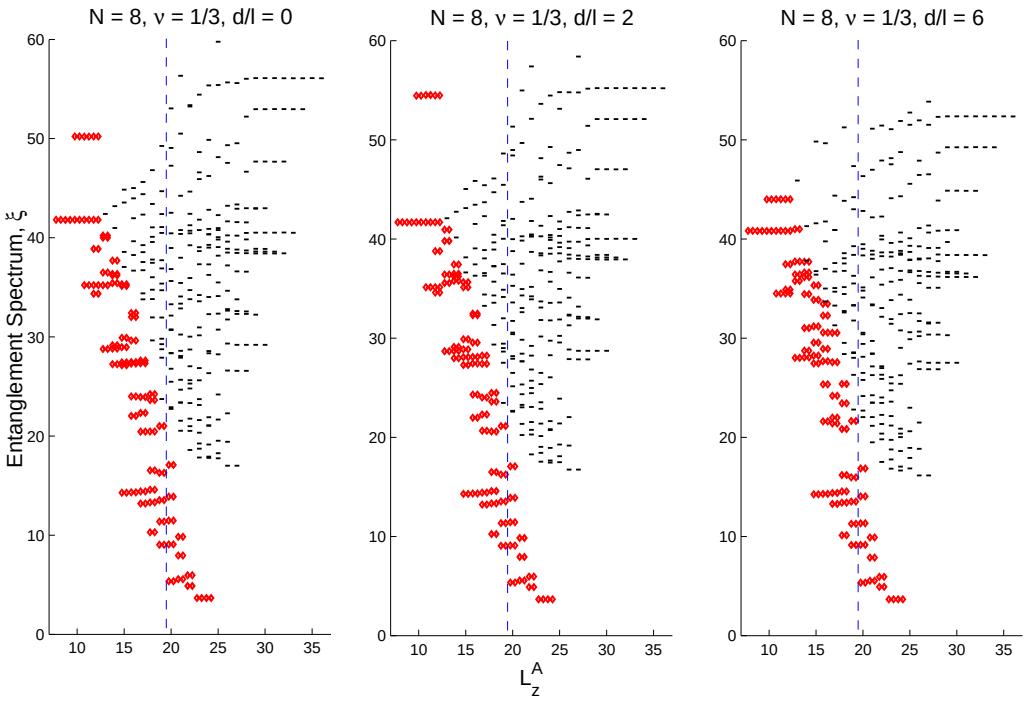

Figure 6.10: Entanglement spectrum for the Coulomb Hamiltonian as a function of z-component of angular momentum L_z^A for filling fraction $\nu = 1/3$ and particle number $N = 8$ for $d/\ell = 0$ (left panel), $d/\ell = 2$ (middle panel), and $d/\ell = 6$ (right panel). The ES levels consistent with the counting in the Laughlin model state for each L_z^A are marked by the diamonds connected by a dash.

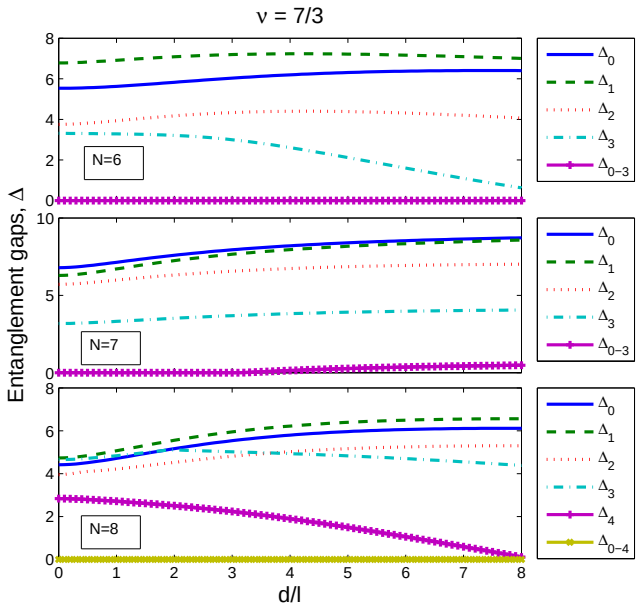

Figure 6.11: Entanglement Gaps for the Coulomb Hamiltonian as a function of finite layer thickness, d/ℓ for filling fraction $\nu = 7/3$ and particle number $N = 6$ (top panel), $N = 7$ (middle panel), and $N = 8$ (bottom panel) with partition at the equator.

state (be it the Laughlin or the MR Pfaffian) and noting how many ES levels $n(L_z^A)$ there are for each L_z^A. Then, when we consider the ES for the Coulomb Hamiltonians, we identify topological levels (and color code them) as the lowest $n(L_z^A)$ ES levels for each L_z^A.

Entanglement gaps as a function of finite layer thickness d/ℓ for the Laughlin filling fraction $\nu = 1/3$ are shown in Fig. 6.9. The entanglement gaps are slightly decreasing with d/ℓ for all cases, indicating that the states are weakening. These trends are similar to those observed in the EE at $\nu = 1/3$. Note that the minimal gap for $N = 6$ and $N = 8$ is initially small and becomes zero for $d/\ell \gtrsim 4$. This may indicate that the FQH state collapses at a finite thickness, as has been shown in previous works[127, 163] (the previous works showed the FQHE to collapse at very

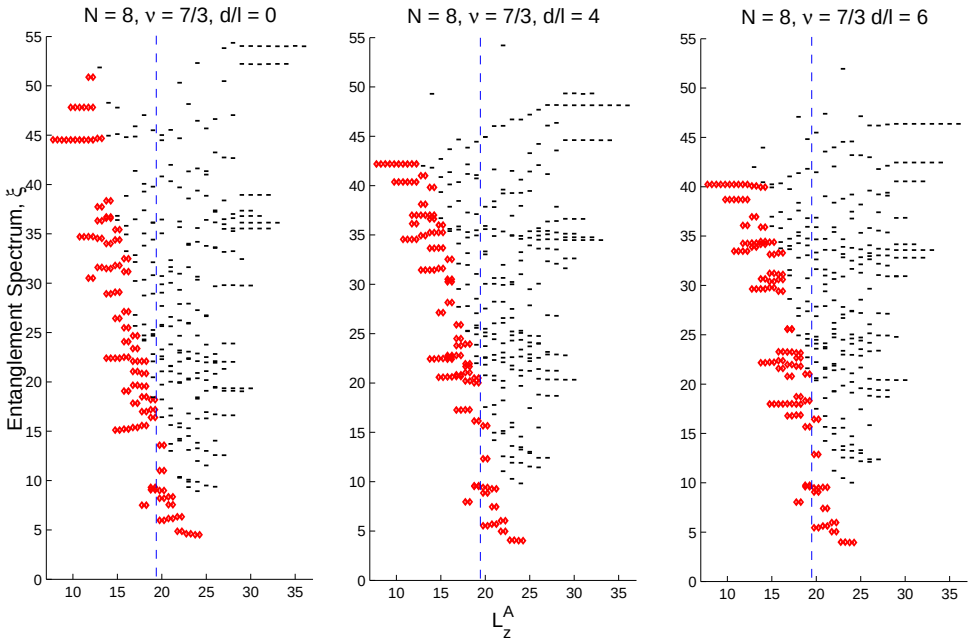

Figure 6.12: Entanglement spectrum for the Coulomb Hamiltonian as a function of z-component of angular momentum L_z^A for filling fraction $\nu = 1/3$ and particle number $N = 8$ for $d/\ell = 0$ (left panel), $d/\ell = 4$ (middle panel), $d/\ell = 6$ (right panel). The ES levels consistent with the counting in the Laughlin model state for each L_z^A are marked.

large d/ℓ). However, this effect is not seen in the minimal entanglement gap for $N = 7$. This "even-odd" finite size effect is likely due in part to a trade-off between the finite size cutoff and the number of available orbitals. Indeed, the finite size cutoff is the same for $N = 6$ and $N = 7$, but the larger Hilbert space for the $N = 7$ case allows for more "edge excitations" which strengthens each entanglement gap, not just the minimal gap, compared to $N = 6$. In all cases, however, the overall trends in the entanglement gaps (i.e., slight decrease with d/ℓ) are qualitatively similar to those seen in the EE (in particular, ΔS_E) and the overlap in Refs. [128, 129].

To illustrate this overall trend in the entanglement gaps for $\nu = 1/3$, we provide the ES of the ground states in Fig. 6.10 for $d/\ell = 0$, 2 and 6. We have marked the levels that are consistent with the counting found in the ES of the Laughlin model state shown in Fig. 6.6 for all values of ΔL and indicate our chosen finite size cutoff. We see that qualitatively, the ES is largely insensitive to finite d/ℓ. Also on the right of the finite size cutoff, except for the largest topological state at $\Delta L = 4$, the topological levels are well-separated from the higher energy generic levels.

We now examine the case when $\nu = 7/3$ in comparison. In Fig. 6.11 are the entanglement gaps as a function of finite layer thickness. For $N = 6$, the root entanglement gap, Δ_0, is generally increasing with d/ℓ. Δ_1 and Δ_2 each have a weak, local maxima near $d/\ell \sim 4$ and Δ_3 is actually decreasing with d/ℓ. Also the minimal entanglement gap is zero throughout. The entanglement gaps for $N = 7$ are are each monotonically increasing with d/ℓ, similar to Δ_0 in the $N = 6$ case. The minimal gap, which is initially zero, opens at $d/\ell \sim 3$ then gradually increases with d/ℓ in this case. The case when $N = 8$ shows trends similar to the $N = 6$

case. Here Δ_0, Δ_1, and Δ_2 increase with d/ℓ, Δ_3 has a local maxima near $d/\ell \sim 4$, and Δ_4 decreases with d/ℓ. The minimal gap for $N = 8$ is zero throughout. Again we see an "even-odd" finite size effect in the entanglement gaps as was seen with $\nu = 1/3$. However, in this case, we have entanglement gaps that increase, decrease, or have a weak maxima as a function of d/ℓ. This is in contrast to the $\nu = 1/3$ case where *all* entanglement gaps follow the same trend with finite d/ℓ. The different trends in the entanglement gaps may suggest that the topological signature of the $\nu = 7/3$ state differs from that of the Laughlin state.

Some illustrative examples of ES at $\nu = 7/3$ are given in Fig. 6.12 with $N = 8$ and $d/\ell = 0$, 4 and 6. The given ES appear to have structure similar to that seen in the $\nu = 1/3$ case, however, we see that for $\Delta L = 4$, the higher energy "topological" states are virtually indistinguishable from the "generic states". This "blending" appears to get worse for larger d/ℓ. Again, these results may suggest that the Laughlin model state is not an accurate description for the $\nu = 7/3$ state.

Results on the entanglement gaps for the even denominator filling fraction $\nu = 1/2$ are shown in Fig. 6.13. Here we see that the entanglement gaps are slightly decreasing with d/ℓ and behave similarly to the EE at this filling fraction. Also note that for $N = 8$, the minimal gap is small and decreases with d/ℓ, while for $N = 10$, the minimal gap is zero throughout. As mentioned earlier, there has been no definitive experimental observation of FQHE at $\nu = 1/2$ in monolayer systems consistent with our calculations. The ES of the ground states for $d/\ell = 0$, 2 and 6 and $N = 8$ are given in Fig. 6.14,. Qualitatively, we see that the ES is largely insensitive to the finite-thickness effect. Also, the largest suspected topological level

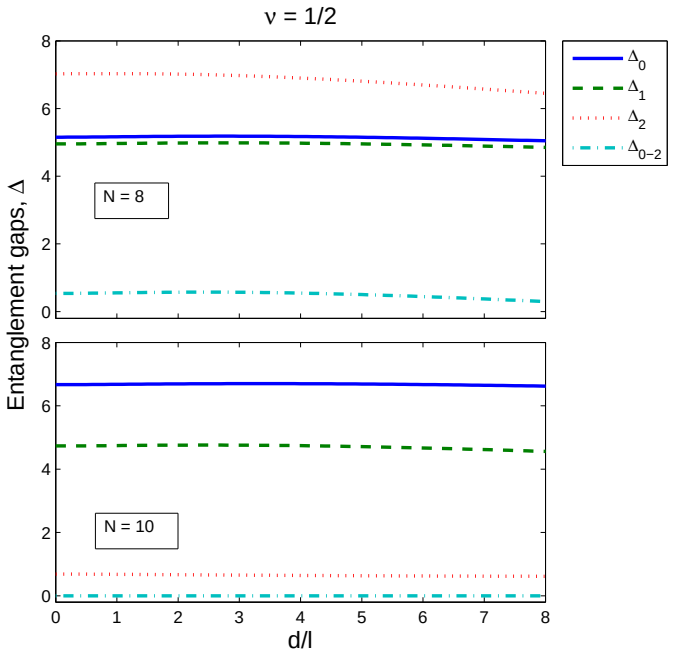

Figure 6.13: Entanglement Gaps for the Coulomb Hamiltonian as a function of finite layer thickness, d/ℓ for filling fraction $\nu = 1/2$ and particle number $N = 8$ (top panel) and $N = 10$ (bottom panel) with partition at the equator.

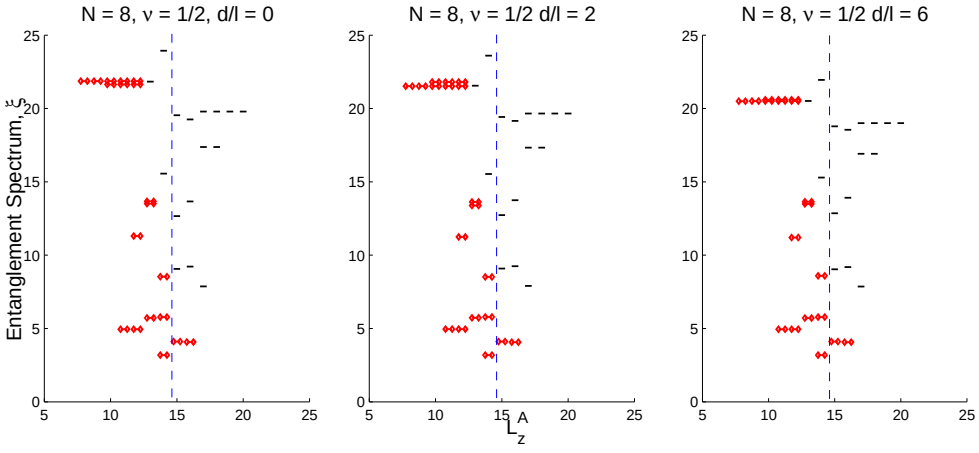

Figure 6.14: Entanglement spectrum for the Coulomb Hamiltonian as a function of z-component of angular momentum L_z^A for filling fraction $\nu = 1/2$ and particle number $N = 8$ for $d/\ell = 0$ (left panel), $d/\ell = 2$ (middle panel), $d/\ell = 6$ (right panel). The levels consistent with the MR Pfaffian model state for each L_z^A are marked.

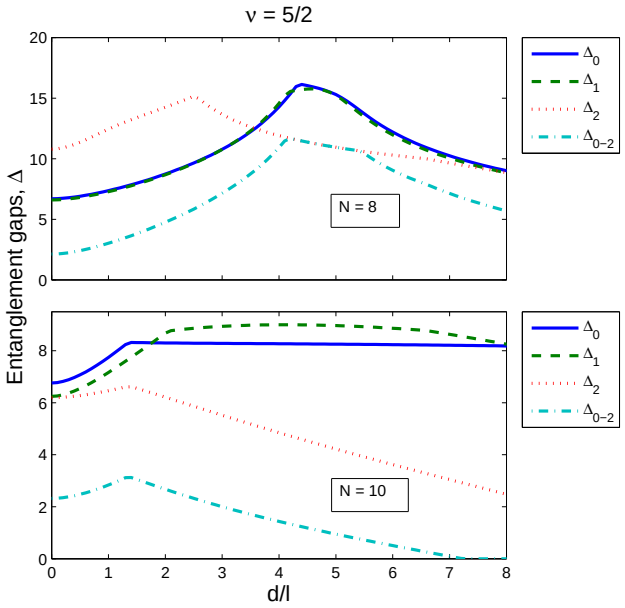

Figure 6.15: Entanglement Gaps for the Coulomb Hamiltonian as a function of finite layer thickness, d/ℓ for filling fraction $\nu = 5/2$ and particle number $N = 8$ (top panel) and $N = 10$ (bottom panel) with partition at the equator.

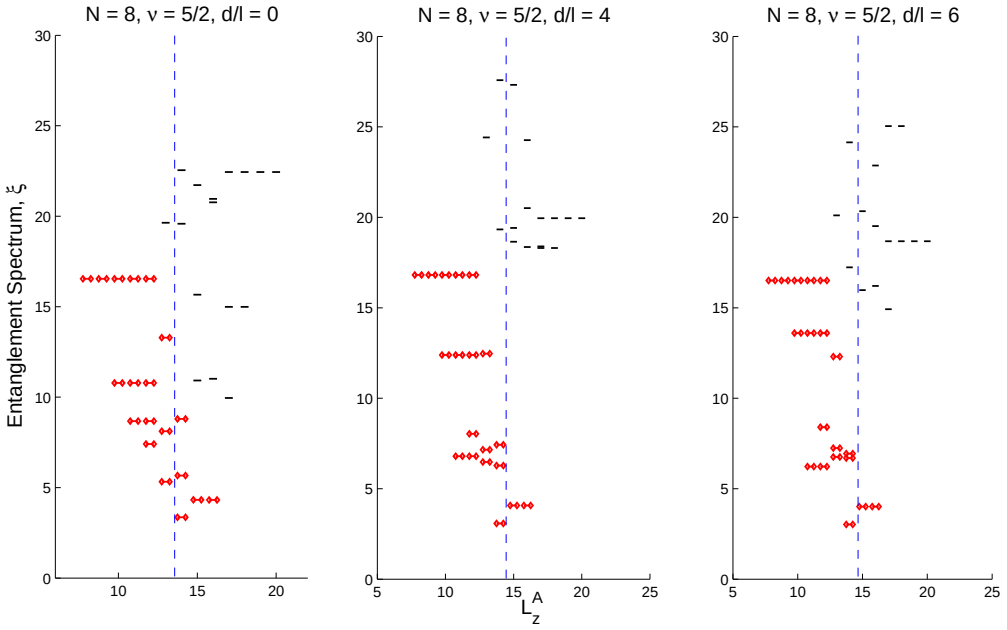

Figure 6.16: Entanglement spectrum for the Coulomb Hamiltonian as a function of z-component of angular of angular momentum L_z^A for filling fraction $\nu = 5/2$ and particle number $N = 8$ for $d/\ell = 0$ (left panel), $d/\ell = 4$ (middle panel), $d/\ell = 6$ (right panel). The levels consistent with the MR Pfaffian model state for each L_z^A are marked.

for $\Delta L = 2$ is well separated from the other CFT levels and appears to be more consistent with the generic levels. Again, this suggests that $\nu = 1/2$ is not described by the MR Pfaffian wavefunction.

In Fig. 6.15 are the entanglement gaps at filling fraction $\nu = 5/2$. For $N = 8$ each entanglement gap peaks at a certain value for d/ℓ. In particular Δ_2 peaks near $d/\ell \sim 2.5$; the other gaps peak near $d/\ell \sim 4$. We also see peaks in the entanglement gaps for the case when $N = 10$. Here, the gaps gradually rise to a local maxima near $d/\ell \sim 1.5$ then slowly decay for increasing d/ℓ. Note that the gaps in this case are generally smaller compared to those observed for $N = 8$. These results may suggest that there is a slight difference in the finite-size effect on the different MR Pfaffian sectors (i.e choice of partition in the root configuration). However, these results are qualitatively similar to the EE results and the results on the overlap in Refs. [129] (i.e., the MR Pfaffian signature of the $\nu = 5/2$ state is strengthened by the finite size effect).

We also provide the ES of the $\nu = 5/2$ state for $N = 8$ in Fig. 6.16 for $d/\ell = 0$, 4, and 6. Here, we see the ES "opens" at $d/\ell = 4$, giving a larger separation between the topological and generic levels in the spectrum compared to $d/\ell = 0$ and 6. Again, these results suggests the $\nu = 5/2$ is, indeed, described by the MR Pfaffian wavefunction, and this description is more stable at finite thickness.

In summary, the entanglement gaps in the ES have similar dependence on finite thickness as the EE, leading to similar conclusions. However finite size effects prevent us from making definitive statements. In the next section, we attempt to alleviate this problem using the conformal limit.

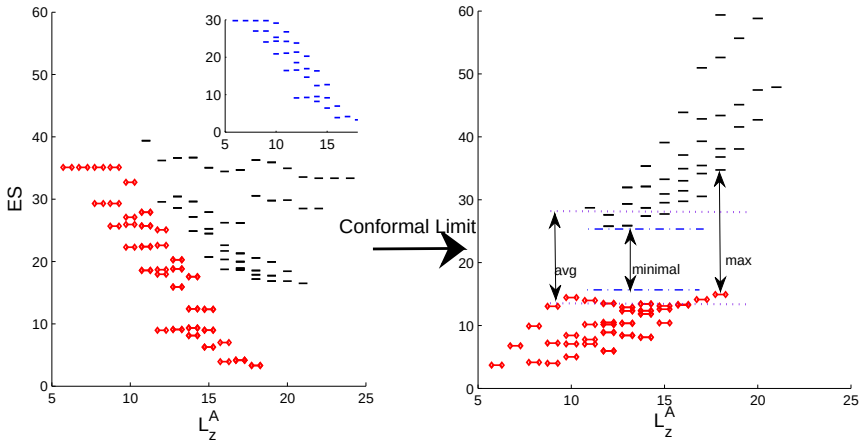

Figure 6.17: ES for the Coulomb Hamiltonian for $\nu = 1/3$, $d = 0$, and $N = 7$ as a function of L_z^A before and after taking the CL. The suspected topological states are based on the ES of the Laughlin model wave function shown (inset) and are marked in the ES. An illustrations for the minimal, maximum, and average entanglement gap is also shown.

6.2.4 The Conformal Limit

In the previous section, we used entanglement gaps in the ES to evaluate the "strength" of a state as a function of d/ℓ and we were able to confirm the MR Pfaffian signature of the $\nu = 5/2$ state and distinguish it from the (lack of) signature of the $\nu = 1/2$ state. However, we have intentionally ignored a significant part of the ES in order to avoid finite size effects, i.e., we focused on the region of the ES with small ΔL (see Fig. 6.8). We determined the size of this region by examining where the ES of the finite sized MR Pfaffian and Laughlin model states deviate from the conjectured structure in the thermodynamic limit (i.e., the edge state level counting given by Haldane statistics). Thus, we have only confirmed the MR Pfaffian and Laughlin signatures to a certain extent because, in fact, there is not an actual entanglement gap in the ES.

It has been conjectured that the *full* entanglement spectrum of the finite sized

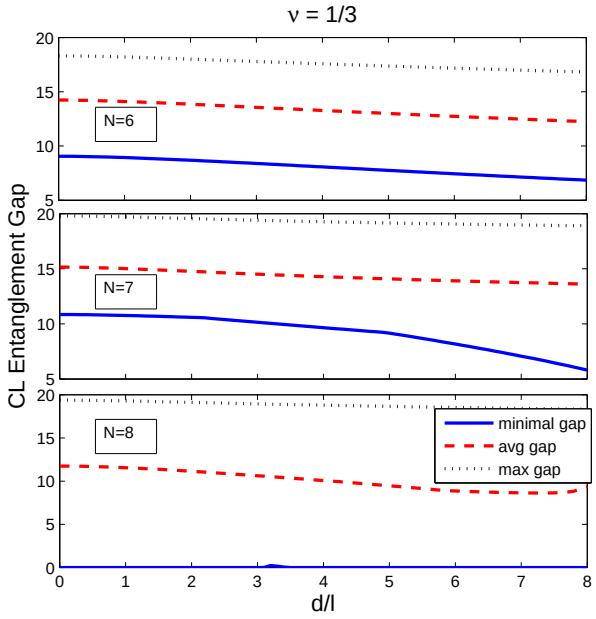

Figure 6.18: Conformal Limit Entanglement Gaps for the Coulomb Hamiltonian as a function of finite layer thickness, d/ℓ for filling fraction $\nu = 1/3$ and particle number $N = 6$ (top panel), $N = 7$ (middle panel), and $N = 8$ (bottom panel).

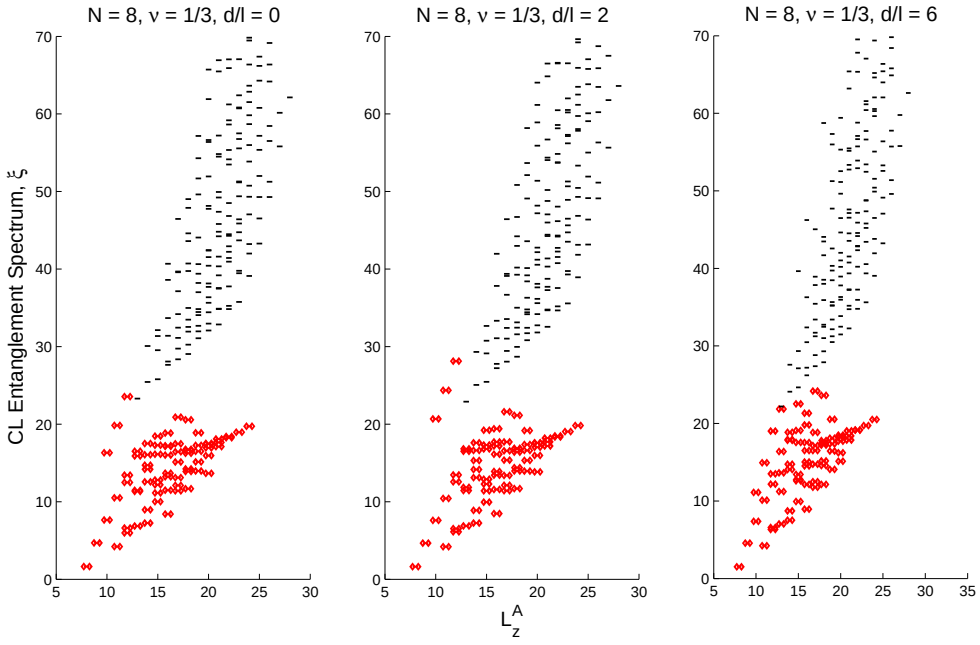

Figure 6.19: Conformal Limit Entanglement spectrum for the Coulomb Hamiltonian as a function of L_z^A for filling fraction $\nu = 1/3$ and particle number $N = 8$ for $d/\ell = 0$ (left panel), $d/\ell = 2$ (middle panel), $d/\ell = 6$ (right panel). The suspected topological levels consistent with the Laughlin model state for each L_z^A are marked.

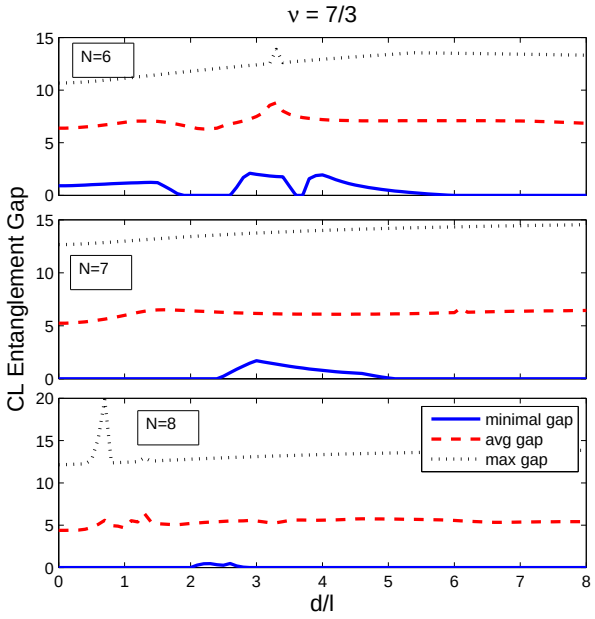

Figure 6.20: Conformal Limit Entanglement Gaps for the Coulomb Hamiltonian as a function of finite layer thickness, d/ℓ for filling fraction $\nu = 1/3$ and particle number $N = 6$ (top panel), $N = 7$ (middle panel), and $N = 8$ (bottom panel).

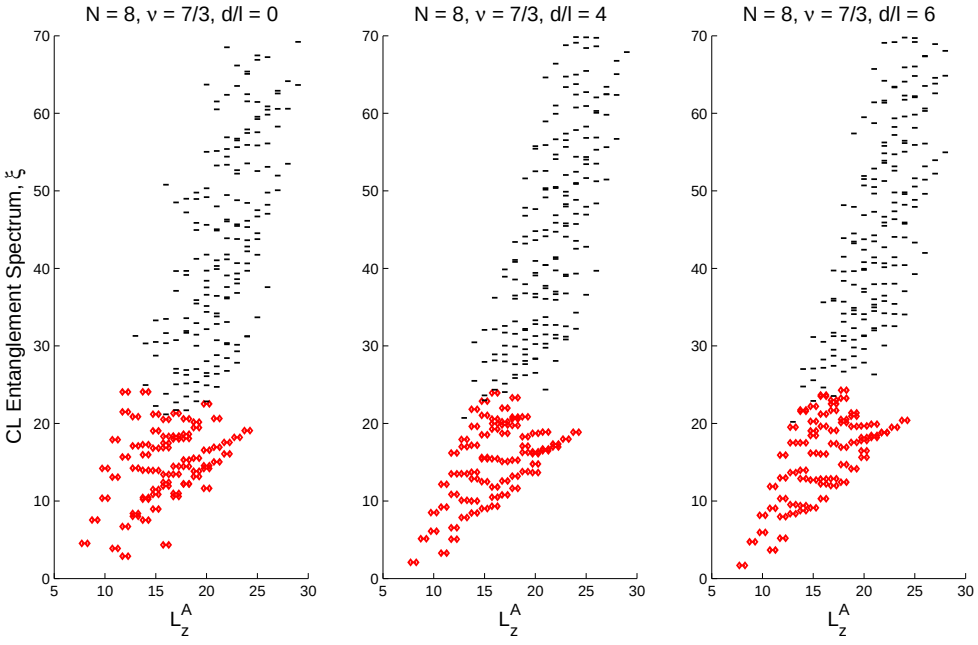

Figure 6.21: Conformal Limit Entanglement spectrum for the Coulomb Hamiltonian as a function of L_z^A for filling fraction $\nu = 1/3$ and particle number $N = 8$ for $d/\ell = 0$ (left panel), $d/\ell = 4$ (middle panel), $d/\ell = 6$ (right panel). The suspected topological levels consistent with the Laughlin model state for each L_z^A are marked.

model states contain information on the topological signature of the FQH state.[148, 149] Thus, all states in the ES can be used to identify the topological quantities. With this in mind, we now examine the entanglement spectrum of quasi-2D FQH states in the "conformal limit" (CL), which reportedly allows the use of the entire spectrum to examine the state by unambiguously defining a full entanglement gap. As discussed briefly above, and at length by Thomale *et al.* in Ref. [155], the CL works by removing finite size effects due to the curvature of the sphere and gives an ES with a "full" unambiguous entanglement gap in the spectrum for topologically ordered states. Thus the presence of an entanglement gap in the conformal limit is conjectured to be a sign of topological order. A demonstration of an ES before and after the CL is given in Fig. 6.17. After taking the CL of an ES (CLES), we determine the "minimal gap" by taking the difference between the highest suspected topological level and the lowest generic level in the entire spectrum. The suspected topological levels are determined by comparing the CLES to that of the model state with the assumption that *all* levels in the ES of the model state are topological. For comparison, we examine the entanglement gaps for each value of L_z^A and define the "average gap" as the average of the individual entanglement gaps. We also define the "maximum gap" as the maximum of the entanglement gaps. Individual gaps that are near infinite (i.e., no levels above the highest topological level) are ignored. The minimal gap, the average gap, and the maximum gap are calculated for each CLES as a function of the finite layer thickness, d/ℓ.

CLES entanglement gaps as a function of finite layer thickness d/ℓ for $\nu = 1/3$ (LLL) are shown in Fig. 6.18. For $N = 6$ and 7, the entanglement gap measures

decreases with d/ℓ but remains finite throughout. This behavior is qualitatively similar to the ES gaps for small ΔL, as well as the EE results, suggesting a weakening of the Laughlin state. The fact that the minimal entanglement gap in the ES for the $N = 6$ case (Fig. 6.9) differs from the minimal gap in the CLES may indicate that the closing of the gap in the ES is due to finite size effects related to the curvature of the geometry rather than the limited number of LL orbitals. However, the minimal gap for the case where $N = 8$ seems anomalous. Although the average and maximum gaps follow similar qualitative trends, the minimal gap is at or near 0 for all values of d/ℓ, including $d = 0$. How to interpret this result is unclear since there is a general consensus that the Laughlin state does, indeed, model the $\nu = 1/3$ state. We can shed some light on this anomaly by examining the CLES of the FQH states directly. In Fig. 6.19 are the CLES for $\nu = 1/3$, $N = 8$ FQH state at finite thickness $d/\ell = 0$, 2 and 6. The suspected topological levels are marked in each plot. In the figure, we see 3 "spurious" topological states that cross the gap, resulting in the minimal gap vanishing. The origin of these states are actually due to our choice of planar pseudopotentials. This is discussed in section 6.2.6.

We examine CLES in the SLL case ($\nu = 7/3$) in Fig. 6.20. In general, each gap measure behaves differently with varying d/ℓ. The minimal gap appears fragile and virtually disappears for larger N. The average gap has two local maxima in d/ℓ for $N = 6$. Only one of the local maxima in the average gap is preserved when we look at the $N = 7$ case, and for $N = 8$, the average gap fluctuates. The maximum gap, in general, increases with increasing d/ℓ but has a notable peak near $d/\ell \sim 0.7$ for $N = 8$. The inconsistency in these results may suggest, from the ES and EE

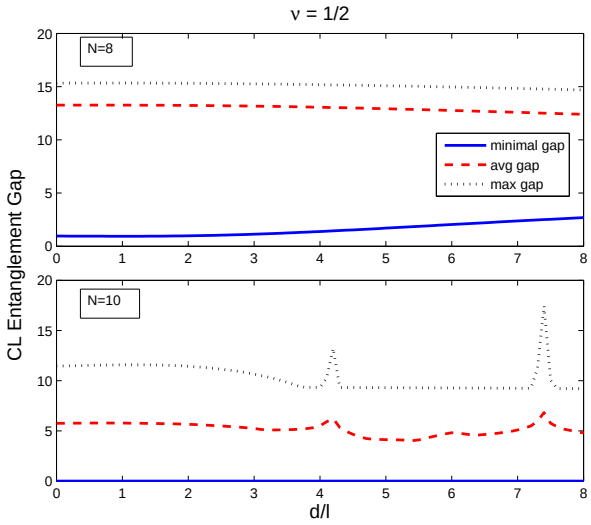

Figure 6.22: Conformal Limit Entanglement Gaps as a function of finite layer thickness, d/ℓ for filling fraction $\nu = 1/2$ and particle number $N = 8$ (top panel) and $N = 10$ (bottom panel)

results, that the Laughlin model state is not a suitable model for the $\nu = 7/3$ state, or other ignored effects are needed for the Coulomb state to be adequately described by the Laughlin state.

In Fig. 6.21 are CLES results for $\nu = 7/3$, $N = 8$ at finite thickness $d/\ell = 0$, 4, and 6. We note that for each value of d/ℓ, there is very little separation between the suspected topological levels and the generic levels. Indeed, if the suspected topological levels were not marked, there is no clear entanglement gap across the whole spectrum. However, there does appear to be structure in the CLES for small values of ΔL (i.e., near the "root" configuration). What this may imply about the topological signature of the $\nu = 7/3$ state is not clear.

Results for the CLES gap measures in the even denominator $\nu = 1/2$ FQH state are shown in Fig. 6.22. We see that the minimal gap is nonzero and gradually increases with d/ℓ for $N = 8$. However, for $N = 10$ the minimal gap is zero

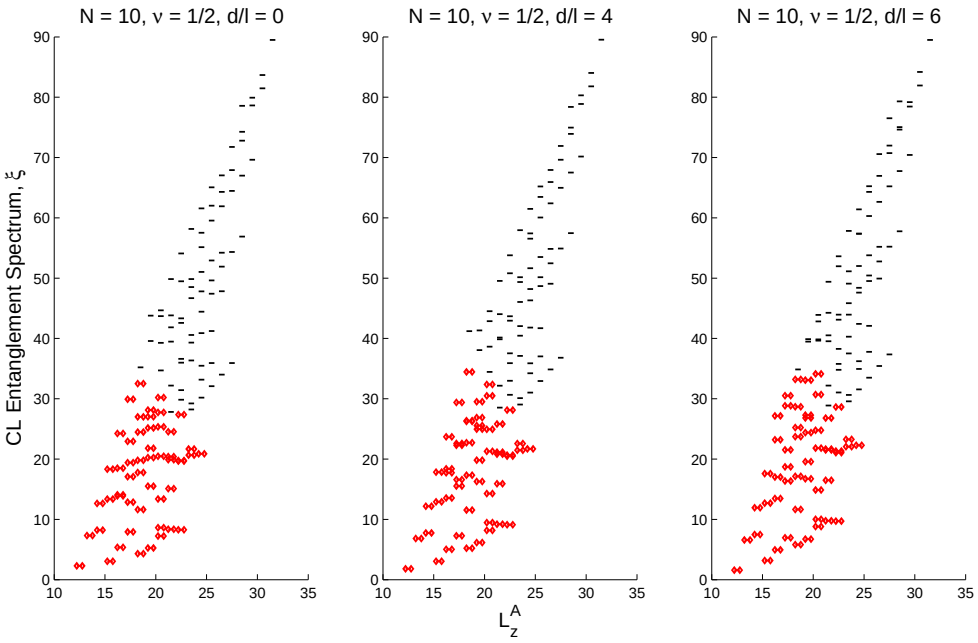

Figure 6.23: Entanglement spectrum as a function of z-component of angular momentum L_z^A for filling fraction $\nu = 1/2$ and particle number $N = 10$ for $d/\ell = 0$ (left panel), $d/\ell = 4$ (middle panel), $d/\ell = 6$ (right panel). The suspected levels consistent with the MR Pfaffian model state for each L_z^A are marked.

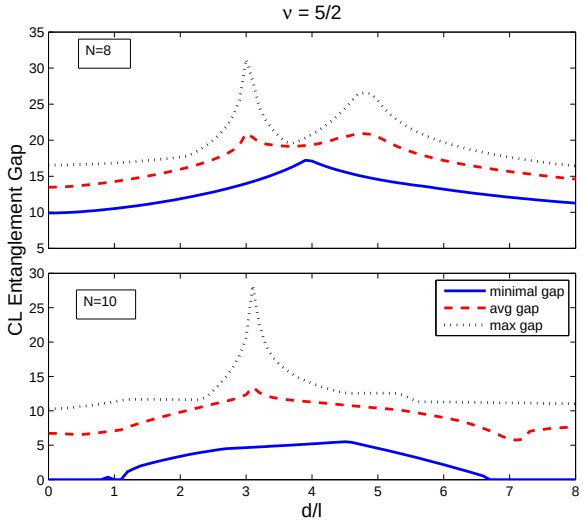

Figure 6.24: Entanglement Gaps as a function of finite layer thickness, d/ℓ for filling fraction $\nu = 5/2$ and particle number $N = 8$ (top panel) and $N = 10$ (bottom panel) with partition at the equator.

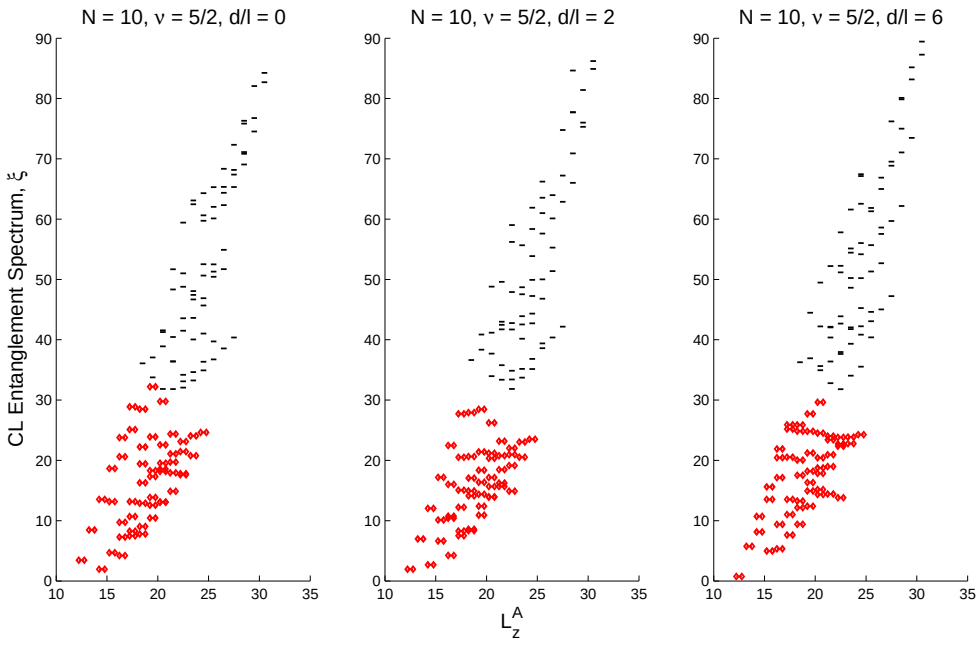

Figure 6.25: Entanglement spectrum as a function of z-component of angular momentum L_z^A for filling fraction $\nu = 5/2$ and particle number $N = 10$ for $d/\ell = 0$ (left panel), $d/\ell = 2$ (middle panel), $d/\ell = 6$ (right panel). The suspected levels consistent with the MR Pfaffian model state for each L_z^A are marked.

throughout. The maximum and average gaps decrease with d/ℓ for $N = 8$. For $N = 10$, the average gap has several local maxima, while the maximum gap decreases then suddenly becomes constant with d/ℓ with two sharp peaks. Given our results on the EE and the ES for this state and the inconsistency between the $N = 8$ and $N = 10$ in the CLES gap measures may suggest that the MR Pfaffian model state is not a suitable model for $\nu = 1/2$. We also provide the CLES of the ground states in Fig. 6.23 for $N = 10$ and $d/\ell = 0$, 4, and 6. Qualitatively, the CLES do not change very much as a function of d/ℓ, and there is no clear separation between the topological and generic levels. This, again, suggests that there is no FQH state at this filling fraction.

The CLES gap measures for $\nu = 5/2$ in the SLL are given in Fig. 6.24. For

$N = 8$, the minimal gap has a very pronounced peak near $d/\ell \approx 4$. The average and maximum gaps, however, have a local minima near where the minimal gap is maximum. These "cusps" are a result of level crossings. For $N = 10$, the minimal gap is initially zero, but becomes finite for non-zero d/ℓ and peaks near $d/\ell \approx 4.5$. The average and maximum gap in this case have similar shapes with a peak near $d/\ell \approx 3$. These results are qualitatively similar to the results of the ES, EE, and the overlap in Refs. [128, 129]. Also, the difference between $N = 8$ and $N = 10$ may suggest that finite thickness affects the partition choices differently, but larger system sizes are necessary to verify this. In the CLES plots shown in Fig. 6.25 for $N = 10$ and $d/\ell = 0$, 4 and 6 respectively, we see the entanglement gap between topological and generic levels "open" at finite $d/\ell = 4$ compared to $d/\ell = 0$ and 6. These results are consistent with results observed with the EE and the ES, indicating that MR Pfaffian signature strengthens with a finite d/ℓ.

In summary, taking the conformal limit of the entanglement spectra provides us with a full entanglement gap in most cases with a finite thickness dependence that is qualitatively similar to the results on the EE. The notable exceptions are the $\nu = 1/2$ which has little or no entanglement gap consistent with experimental observations, the $\nu = 1/3$ case at $N = 8$ which is not expected given results with other system sizes, and the $\nu = 7/3$ case which is consistent with the results on the EE and ES suggesting other physics besides the Laughlin state alone is needed to explain this FQHE. The case with $N = 8$ and $\nu = 1/3$, however, is inconsistent with most theory and experiment, but when we examine the spectra directly, there are a few "spurious" states that cross an otherwise full gap. The origin of these "spurious"

states are related to our use of planar Haldane pseudopotentials rather than spherical pseudopotentials and is discussed in section 6.2.6. However this choice should not alter the topological features of the state. Therefore, this result may suggest that a "full" quantitative entanglement gap is not necessary to identify a topological state or that the full gap is not topological in origin. In the next section, we introduce the concept of a entanglement spectral density of states where a qualitative, "soft" gap may be identified in such cases.

6.2.5 Entanglement Spectrum Density of States

In the entanglement results presented above, we require a model state wavefunction for comparison in order to systematically define and calculate the entanglement gaps. These methods have the obvious disadvantage of requiring an ansatz for comparison. In the conformal limit case, we assume the low-lying states in the entanglement spectrum should have the exact counting as seen in the model entanglement spectrum. This assumption may be premature since other finite size effects may cause the counting to deviate, even after taking the conformal limit, especially at the largest ΔL, see Fig. 6.19. With this in mind, we attempt to obtain a general qualitative sense for how the entanglement spectra vary with finite layer thickness by extending the analogy with "energy levels" a bit further by calculating the "density of entanglement spectral states." With the density of states, we can qualitatively look for entanglement gaps without relying on a model state for comparison. Also, we may be able to detect "soft" gaps where a small number of states may be present

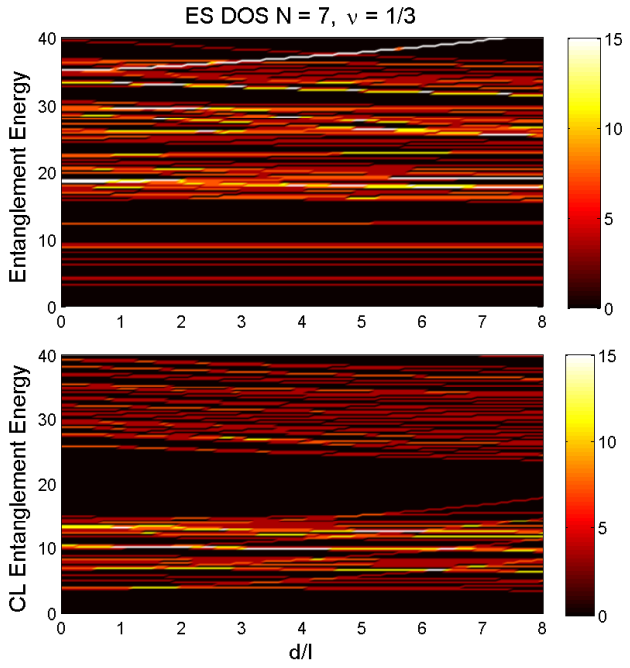

Figure 6.26: Density of entanglement energies before (top panel) and after (bottom panel) the conformal limit for $\nu = 1/3$ and particle number $N = 7$ as a function of finite layer thickness d/ℓ.

within an otherwise prominent gap between two peaks in the density of states. Thus in this section we briefly examine this extension by providing results for the density of states (DOS) of the entanglement spectrum, both with and without the conformal limit, as a function of finite layer thickness, d/ℓ.

The plots shown in Fig. 6.26 give the density of states of the ES and CLES for $\nu = 1/3$ as a function of finite layer thickness d/ℓ for $N = 7$. In the DOS for the ES before taking the CL, we see sparse low lying states that are separated from a denser cloud of higher states by a series of gaps. These low lying states are the topological states from the Li and Haldane conjecture. The states appear, largely to be insensitive to the finite layer thickness. Turning to the DOS for the CLES, a clear gap is much more evident for the $N = 7$ cases. Here the higher-energy states

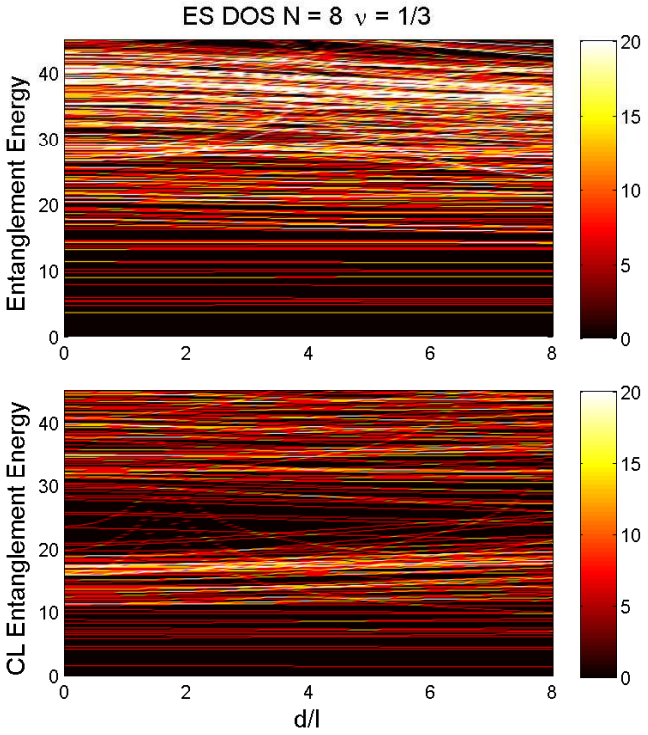

Figure 6.27: Density of entanglement energies before (top panel) and after (bottom panel) the conformal limit for $\nu = 1/3$ and particle number $N = 8$ as a function of finite layer thickness d/ℓ.

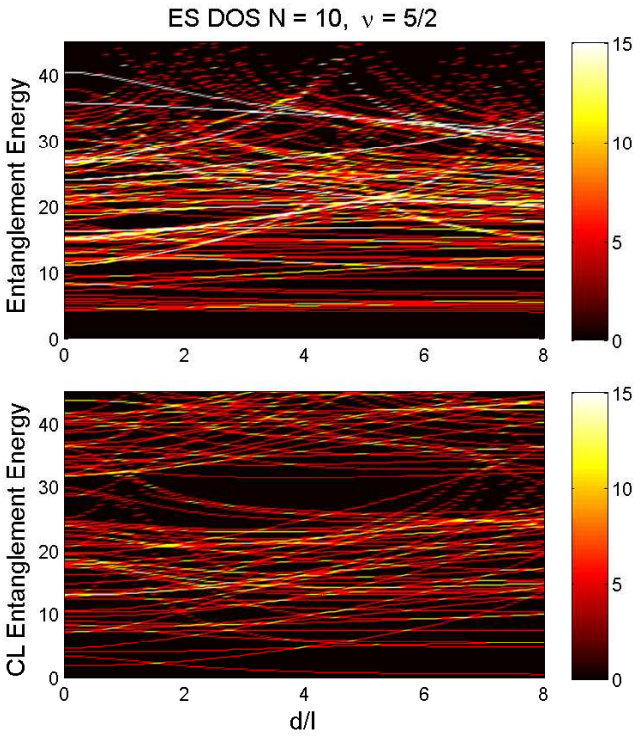

Figure 6.28: Density of entanglement energies before (top panel) and after (bottom panel) the conformal limit for $\nu = 1/3$ and particle number $N = 7$ as a function of finite layer thickness d/ℓ.

appear to makeup a wide, low-density band that is well-separated from a low, dense band of states by a gap that decreases with d/ℓ. This case seems to illustrate the effect of using the CL.

For comparison, we provide the DOS results for $N = 8$ in Fig. 6.27. Here there also appears to be low-lying topological states in the ES below a high density region of higher energy states. In the DOS of the CLES, a "clear" gap does not appear. But the low lying band in this case does appear qualitatively similar to the $N = 7$ case. One may possibly associate a "soft" gap in this case, where a few states appear to be present between two somewhat distinct regions in the DOS. This "soft" gap is qualitatively similar to the "clear" gap in the $N = 7$ case and it does appear to be slightly decreasing as a function of d/ℓ. However, it is difficult to distinguish this "soft" gap from the other small gaps in the spectrum.

In Fig. 6.28 we provide DOS plots for the $\nu = 5/2$ FQH state for $N = 10$ as a function of d/ℓ. In this case, the ES is especially sensitive to finite layer thickness. However, we still see a series of small gaps separating thin, dense bands at lower energies. After taking the CL, a clear gap at finite (non-zero) thickness has a definite peak corresponding to a level crossing. Below the gap, there appears to be some band crossings as d/ℓ is varied.

In summary, the DOS of the entanglement spectra (with and without the conformal limit) gives us a general qualitative picture of how the ES evolve with a varying parameter (i.e., the finite layer thickness d in our case). Thus we expect the DOS of the ES to be a good initial cursory tool in examining topological states with varying parameters.

6.2.6 Planar vs spherical pseudopotentials at $d = 0$

The analysis presented above is based on ground state wavefunctions obtained by diagonalizing the quasi-2D Coulomb potential in a spherical geometry. However the Haldane pseudopotentials used to construct the Hamiltonian are derived from a infinite planar geometry rather than a spherical geometry. We choose to use planar rather than spherical psuedopotentials because 1) the effective Coulomb potential in a quasi-2D system is more naturally obtained in the infinite planar geometry and 2) we expect the spherical and planar pseudopotentials to be indistinguishable in the thermodynamic limit. And given the mostly qualitative nature involved in studying entanglement spectra, we expected this choice to make little difference in the results. Nevertheless, there are cases under study where this choice matters. The goal of this section is to highlight some of these cases. We show that for $d = 0$, the low energy spectrum in the entanglement spectra are qualitatively similar between ground states obtained from either spherical or planar pseudopotentials, but higher energy spectra can differ in some cases. This difference does not change the qualitative conclusions drawn from the low energy spectra, but when we consider the conformal limit which looks for a full entanglement gap, the difference can lead to different conclusions (in particular, the case of $\nu = 1/3$ with $N = 8$). We leave the comparison of cases with $d > 0$ and larger N for future work.

In Table 6.2 we provide several overlap calculations between exact ground states at $d = 0$ obtained using either spherical or planar pseudopotentials. In column 3 of the table, we see that the overlap between the ground states from the

N	ν	$\langle\Psi_{\text{sphere}}\|\Psi_{\text{plane}}\rangle$	$\langle\Psi_{\text{sphere}}\|\Psi_{\text{model}}\rangle$	$\langle\Psi_{\text{plane}}\|\Psi_{\text{model}}\rangle$
6	1/3	0.9988	0.9964	0.9921
6	7/3	0.9480	0.5285	0.7369
7	1/3	0.9999	0.9964	0.9952
7	7/3	0.8648	0.6071	0.8737
8	1/3	0.9996	0.9954	0.9954
8	7/3	0.9675	0.5719	0.7441
8	1/2	0.9978	0.9213	0.8953
8	5/2	0.9688	0.8674	0.9639
10	1/2	0	0.8891	0
10	5/2	0.9720	0.8376	0.9342

Table 6.2: Overlap integrals between 1) the exact ground state wavefunction using spherical ($|\Psi_{\text{sphere}}\rangle$) and planar Haldane pseudopotentials ($|\Psi_{\text{plane}}\rangle$), and 2) the overlap between the Laughlin or Pfaffian wavefunction ($|\Psi_{\text{model}}\rangle$ and the exact ground state wavefunction using spherical or planar pseudopotentials.

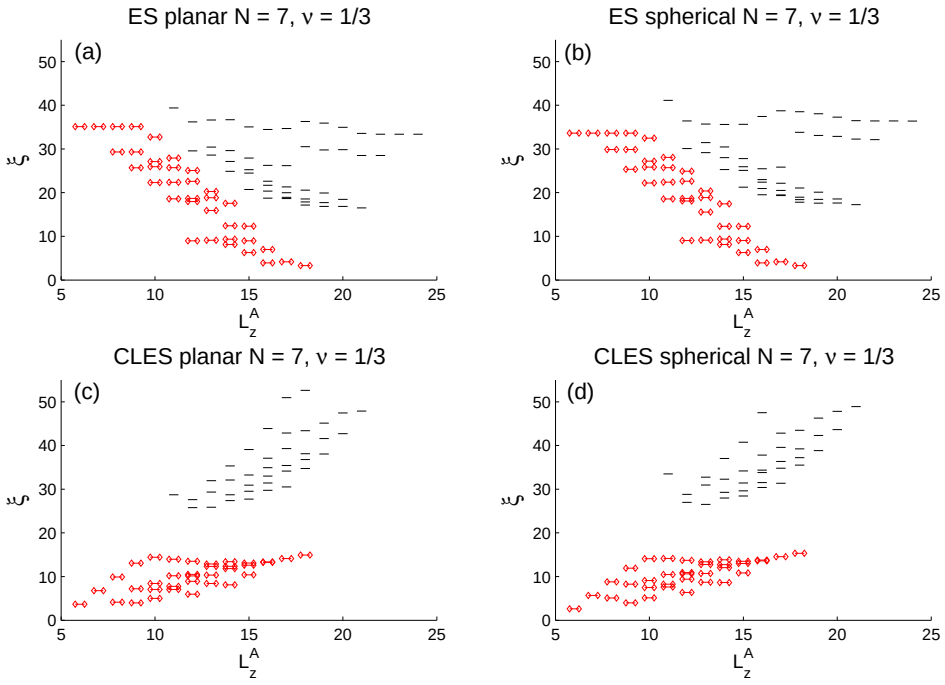

Figure 6.29: Entanglement spectra and conformal limit entanglement spectra of the exact FQHE ground state for $N = 7$ at filling fraction $\nu = 1/3$ obtained with either planar or spherical Haldane pseudopotentials at $d = 0$. Topological states associated with the Laughlin model wavefunction are marked.

spherical and planar cases is generally high. The notable exception is the case when $N = 10$ and $\nu = 1/2$ where the overlap is zero. In this case the ground state obtained with the planar pseudopotentials possesses a different symmetry compared to the ground state of the spherical case, which leads to a vanishing overlap. Excluding these, columns 4 and 5 of the table show that the overlap between the spherical and planar ground states with the model Laughlin or MR Pfaffian states are qualitatively similar.

We now turn our attention to the entanglement spectra and how they may differ with choice of pseudopotentials. ES (with and without the conformal limit) for the exact ground state of the FQHE state at $N = 7$ and $\nu = 1/3$ using spherical

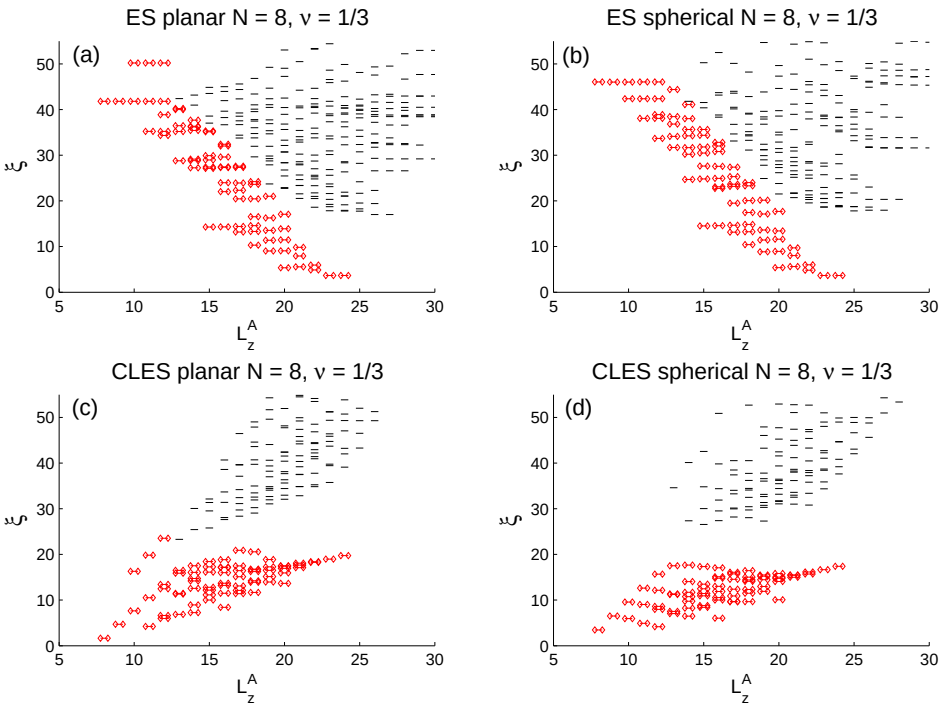

Figure 6.30: Entanglement spectra and conformal limit entanglement spectra of the exact FQHE ground state for $N = 8$ at filling fraction $\nu = 1/3$ obtained with either planar or spherical Haldane pseudopotentials at $d = 0$. Topological states associated with the Laughlin model wavefunction are marked.

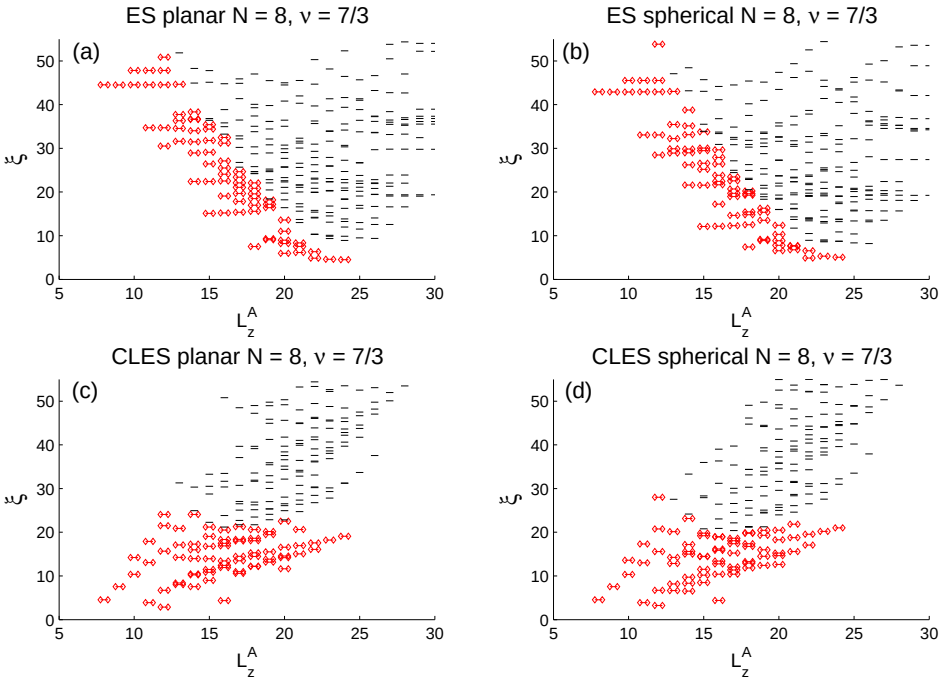

Figure 6.31: Entanglement spectra and conformal limit entanglement spectra of the exact FQHE ground state for $N = 7$ at filling fraction $\nu = 7/3$ obtained with either planar or spherical Haldane pseudopotentials at $d = 0$. Topological states associated with the Laughlin model wavefunction are marked.

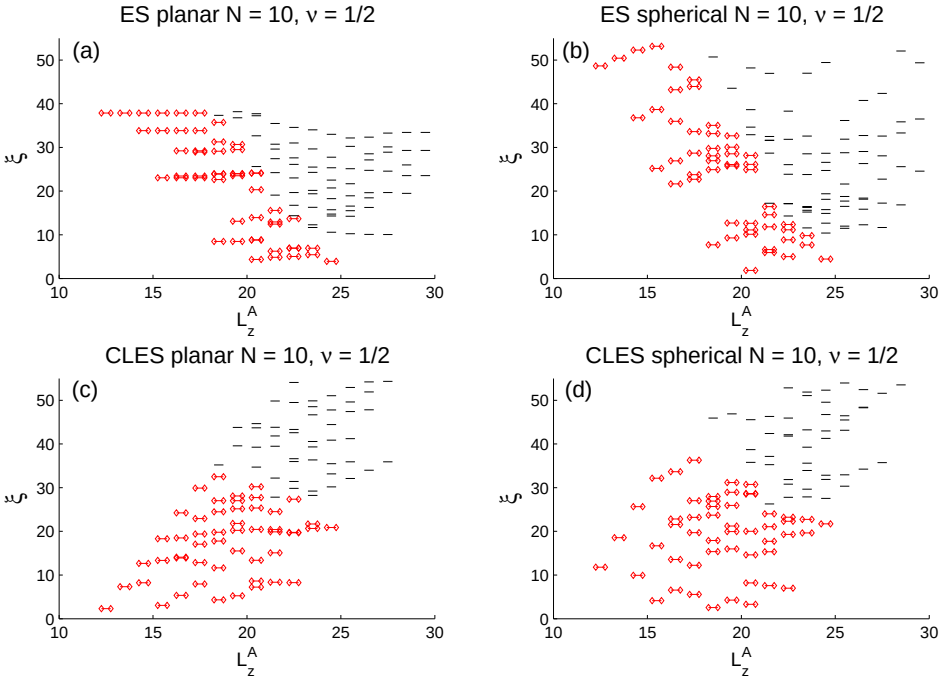

Figure 6.32: Entanglement spectra and conformal limit entanglement spectra of the exact FQHE ground state for $N = 10$ at filling fraction $\nu = 1/2$ obtained with either planar or spherical Haldane pseudopotentials at $d = 0$. Topological states associated with the MR Pfaffian model wavefunction are marked.

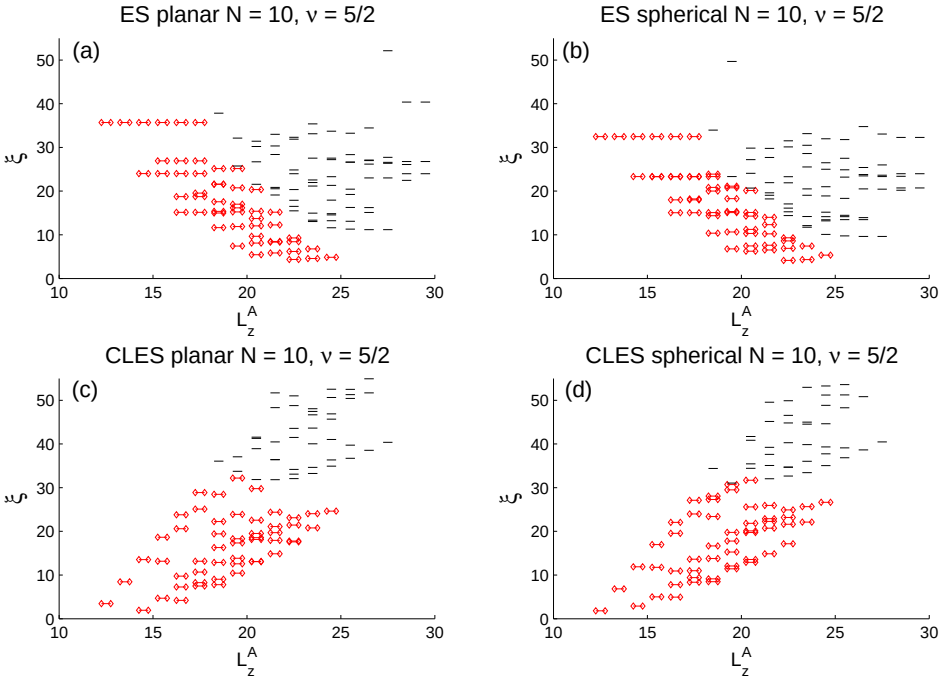

Figure 6.33: Entanglement spectra and conformal limit entanglement spectra of the exact FQHE ground state for $N = 10$ at filling fraction $\nu = 5/2$ obtained with either planar or spherical Haldane pseudopotentials at $d = 0$. Topological states associated with the MR Pfaffian model wavefunction are marked.

and planar pseudopotentials are given in fig. 6.29. In the figure, we see that the ES with planar pseudopotentials (Fig. 6.29 a) is qualitatively similar to the spectra obtained with spherical pseudopotentials (Fig. 6.29 b). The same can also be said with the ES in the conformal limit between the planar case (Fig. 6.29 c) and the spherical case (Fig. 6.29 d). Thus, given the results in Fig. 6.29, we would expect that the choice of pseudopotenials makes little difference in obtaining a qualitative understanding of the ES in this case.

Fig. 6.30 compares the ES of the FQHE state at filling fraction $\nu = 1/3$ with $N = 8$. In this case we see that in the ES before the conformal limit (Fig. 6.30 a and b), the low energy spectra are qualitatively similar between the planar and spherical cases. The higher energy spectra in the ES, however, show notable differences with the planar case having a few topological levels at much higher energy compared to the spherical case. In the conformal limit, these higher energy topological levels lead to a vanishing entanglement gap in the conformal limit for the planar case (Fig. 6.30 c) compared to the spherical case (Fig. 6.30 d) where there is a full entanglement gap. These are the same "spurious" levels identified earlier in section 6.2.4. These results suggest that the vanishing minimal gap seen in Fig. 6.18 is due to our choice of planar rather than spherical Haldane pseudopotentials. This may seem surprising given the large overlaps seen in Table 6.2. However the states associated with the the higher energy topological levels have exponentially small contributions to the ground state wavefunction, and thus contribute little to the overlap. Also we might expect these states to be more sensitive to certain quantitative details of the potential that do not affect the qualitative picture of the FQHE ground state (e.g.

values of V_m for "large" m). Thus when taking the conformal limit, the choice of pseudopotential may matter in some cases in order to observe a full entanglement gap. But a qualitative understanding can still be gleaned from the planar case since there does appear to be two distinct regions in the CLES that we can identify, at least qualitatively, as topological and generic levels.

We now compare the spherical and planar pseudopotentials in the SLL with $\nu = 7/3$. Fig. 6.31 gives the ES (6.31 a and b) and CLES (6.31 c and d) for the $\nu = 7/3$ FQHE state obtained with either planar or spherical pseudopotentials with $N = 8$. The planar and spherical cases are qualitatively similar in both the ES and CLES and both suggest that the Laughlin wavefunction may not describe this state, as discussed in sections 6.2.2, 6.2.3 and 6.2.4.

Results for the even denominator filling fraction $\nu = 1/2$ with $N = 10$ is given in Fig. 6.32. In this case, the planar results (6.30 a and c) differ considerably to that of the spherical case (6.30 b and d). This is not surprising since the overlap between these two states given in table 6.2 vanishes. However, it appears that neither state is consistent with the MR Pfaffian.

Comparison of FQHE ground states obtained with planar and spherical pseudopotentials for the $\nu = 5/2$ state with $N = 10$ is given in Fig. 6.33. Similar to the $\nu = 1/3$ case, the low energy spectra in the ES (6.33 a and b) are qualitatively similar between the two cases. The higher energy levels in the spectra do differ, but the CLES (6.33 c and d) does appear to give the same qualitative picture. Recall that in section 6.2.4, the minimal gap for this case becomes non-zero only at finite d for the planar case. We would expect a similar result to occur using the spherical

psuedopotentials. Verification of this is left for a future work.

6.3 Conclusions

In this chapter we study entanglement in finite sized, quasi-2D FQH states via the entanglement entropy and the entanglement spectrum as a function of the finite layer thickness of the transverse dimension in a realistic FQH system and compare them to the entanglement signatures of the Laughlin and MR Pfaffian model states. For the Laughlin filling fractions, we find that the EE increases (decreases) with finite layer thickness for $\nu = 1/3$ ($\nu = 7/3$) in the LLL (SLL) with increasing (decreasing) deviation from the EE of the Laughlin model state. However the EE in the SLL reaches an asymptotic value larger than the EE of the Laughlin state, possibly suggesting the $\nu = 7/3$ state is modeled by different physics than the Laughlin state. Similar behavior is also seen in the entanglement gaps of the ES for the Laughlin filling fractions. Here we find that the entanglement gaps decrease with finite layer thickness for the Laughlin filling fractions in the LLL. But in the SLL, the behavior of the entanglement gaps depend on the "depth" of the gap. These results suggest that the Laughlin FQH states "weaken" with increasing thickness in the LLL, which is consistent with previous work on quasi-2D FQH states [128, 129], but in the SLL, other physics beyond just the Laughlin state alone is needed to describe the FQH state. The LL dependence of the finite thickness effect at half-filling is slightly different. The EE of the $\nu = 1/2$ state in the LLL is largely insensitive to the finite layer thickness in contrast to that of the SLL $\nu = 5/2$ state

where the EE has a local minima that approaches the EE of the MR Pfaffian at finite d/ℓ. This qualitative behavior is also seen in the entanglement gaps of the ES for half-filled LLs. For $\nu = 5/2$ in the SLL, we see peaks (local maxima) in the entanglement gaps at finite thickness, suggesting the $\nu = 5/2$ is more "MR Pfaffian-like" at an optimal thickness, which, again is consistent with previous work[128, 129] and strongly suggests the $\nu = 5/2$ state is, indeed, MR Pfaffian. In contrast the entanglement gaps of the ES for the $\nu = 1/2$ state suggest that it is not modeled by the MR Pfaffian. Thus, the entanglement gaps in the ES allows us to differentiate the $\nu = 1/2$ and $\nu = 5/2$ states, which we could not definitively establish with the EE or the overlap calculations. Of course, we must be cautious with these results since the calculated entanglement gaps only made use of a few levels in the low-lying spectra due to finite-size effects.

We also investigate the conformal limit of the entanglement spectrum which is conjectured to remove curvature in the spectrum due to finite size effects and allow the use of the entire spectrum to determine the topological signature of the state. Our results on the conformal limit, however are inconsistent between varying system sizes and are difficult to interpret. This appears to be due to our choice of using planar pseudopotentials rather than spherical pseudopotentials in obtaining the FQHE ground states. With this in mind, we examine this choice by comparing the entanglement spectra of ground states obtained by using either spherical or planar pseudopotentials at $d = 0$ and observe that the conformal limit can be affected by components of the ground state that have exponentially small contributions and, therefore, are sensitive to minor details in the interaction (such as the

difference between planar and spherical pseudopotentials). Thus the presence of the entanglement gap in the conformal limit is sensitive to certain details that may not be relevant in determining the topological features of the state. Further work using much larger system sizes would be necessary to resolve this issue which is well beyond the scope of the current work.

We have also introduced the notion of entanglement density of states as a method for examining the idea of an entanglement gap without an explicit reliance on a model wavefunction. Although, far from definitive, the entanglement DOS suggests itself as a powerful tool to determine the topological nature of a particular ground state. Our detailed numerical study establishes the entanglement DOS to be a useful quantity underlying topological FQHE particularly in the context of finite size numerical calculations.

It is interesting to observe that the entanglement measures give similar results to those obtained with overlaps in Refs. [128, 129]. Whereas the overlap is a simple measure of how well a numerically obtained ground state matches a particular model state (e.g. the Laughlin state or the MR Pfaffian state), the entanglement measures (in particular, the ES) is a more general measure of how well a state fits a suspected conformal field theory (i.e. universality class) that describes the model state. Therefore, it can be said that these results confirm the conclusions in Refs. [128, 129] in a more general sense in respect to the Laughlin and MR Pfaffian CFTs. However, we must be cautious in this generalization given that we have only observed the Laughlin and MR Pfaffian signature up to a certain extent in the spectra and different theories can result in the same low-level structure in the ES [164]. More work

is necessary to understand how well entanglement measures can definitely identify universality classes in finite systems.

In interpreting our results and conclusions, one may wonder about the importance of finite size effects on our numerical diagonalization. The possible limitations associated with finite-size effects are of course always present in any exact diagonalization study of any FQHE system, and the possibility that some of the conclusions are affected by finite size effects can never be ruled out even if the calculations are carried out on systems much larger than what we use in this work, since in the end any statement about an experimental system based on calculations performed on few-particle systems is always subject to an extrapolation to the thermodynamic limit. We believe that all our conclusions regarding the importance of finite quasi-2D thickness effect on the FQHE entanglement spectra are valid independent of the rather modest size of our finite system diagonalization study because earlier work [128, 129] clearly established, when compared with calculations [165, 166] carried out on much larger systems, that the system size we use in this work, namely N=8, is certainly adequate in making qualitatively correct conclusions about the SLL FQHE. Our goal in this paper has been to study as many FQHE states as feasible as a function of the quasi-2D layer thickness in depth, thus necessarily (due to the computational time restrictions) limiting our system size to N=8 which should be adequate. Nevertheless, we feel that future work should explore larger system size diagonalization in order to study the finite-thickness effect on the entanglement spectra of various FQHE states.

In conclusion, we have extended the concept of topological entanglement spec-

tra and entanglement gaps to finite-thickness FQH systems by calculating the FQHE topological properties systemically as a function of finite thickness of the quasi-2D systems, establishing in the process that the FQHE entanglement measures calculated as a function of system thickness are completely consistent with the results obtained earlier in the literature using wavefunction overlap calculations. While our work establishes various entanglement measures as important theoretical quantities classifying FQHE, more work will be necessary to understand the finite size aspects of entanglement spectra and entanglement gaps in the context of realistic fractional quantum Hall systems. Although it is gratifying that the qualitative conclusions of our entanglement-measure-based results in this work are completely consistent with earlier FQHE results obtained on the basis of wavefunction overlap calculations, it remains to be seen whether the entanglement-measure based probes have more predictive power regarding the nature of FQHE than the wavefunction-overlap based probes or it is simply a deeper way of looking at the same physics with no obvious additional implications for the experimental occurrence of FQHE.

Chapter 7

A Variational Monte Carlo study of polarization in $\nu = 5/2$

7.1 Background

In the previous chapter, we have assumed that FQHE states are completely polarized. This assumption is largely based on the fact that FQHE states are observed in very large magnetic fields. Because of this, it is usually appropriate to work in the limit of $B \to \infty$, where the Coulomb potential is the only relevant energy scale. But as was mentioned in section 5.3, the Zeeman energy can be less than the Coulomb energy for some filling fractions when the band mass and the renormalized Landé factor of an electron in a material are properly taken into account. This leads to non-trivial spin order in FQHE states that differ depending on the filling fraction. Despite this complication, spin-order in most states is well-understood in the context of composite fermion theory where polarization is seen as a result of filling Λ-levels with spinfull composite fermions following Hund's rule[56]. A notable exception, however, is the case of $\nu = 5/2$. Since it was first discovered in 1987, studies on spin order in this state have been either inconclusive or seemingly contradictory. One of the earliest experiments on this matter, for example, reported the collapse of the $\nu = 5/2$ FQHE state in a tilted magnetic field, suggesting an unpolarized FQHE state[167]. But this experiment was followed by a seminal numerical study by Morf which showed that even in the limit of zero Zeeman energy, a polarized

state is lower in energy than a fully unpolarized state at $\nu = 5/2$[133]. Subsequent theoretical studies reported similar results[168, 169], and it is now understood that the collapse in the original "tilt" experiments was likely due to the appearance of compressible "striped" phases [170] or from orbital coupling of the in-plane magnetic field[129]. To avoid these issues, Liu et al. [171] performed an "altered" tilt experiment where the in-plane magnetic field is kept small by varying the charge density and showed that the $\nu = 5/2$ state remains stable for relatively large tilt angles. Recent rather impressive experiments performed by Tiemann et al. [172] and Stern et al. [173] provide strong evidence supporting a fully spin polarized 5/2 FQHE state. But a notable exception is an earlier experiment by Stern et al. [174] using photoluminescence spectroscopy to probe polarization, suggesting that the $\nu = 5/2$ state is actually unpolarized. A similar result was also seen in a study by Rhone et al. [85] where spin-order is probed via resonant light scattering. It is possible that the signatures seen in these optical experiments [174, 85] are due to local spin order near a charge impurity[175, 176] and are, therefore, inconclusive, but such results still leave some doubt to the actual nature of spin-order in this state [177]. The most convincing measurement to date are those by Tiemann et al. and Stern et al. [172, 174], which do indicate a spin-polarized 5/2 FQHE. Our goal in the current work is to provide a reasonably complete study of spin-polarization comparing the candidate states MR Pfaffian versus 331 with respect to the 5/2 FQHE using direct numerical techniques in reasonably realistic theoretical models to see if one or the other can be ruled out purely on the basis of numerical studies.

Resolving the spin order of $\nu = 5/2$ may have implications on the possibil-

ity of using FQHE states for topological quantum computing. The MR Pfaffian description for $\nu = 5/2$, which predicts non-Abelian anyons, is fully spin-polarized and is the leading theory to date. But there are alternative descriptions that do not require non-Abelian statistics, and one of the leading alternatives is the unpolarized Halperin 331 state [178]. Part of the Halperin (m,m,n) family of Abelian fractional quantum Hall states [178], the 331 state is observed in half filled quantum hall bilayers where even denominator fractions are common and well understood. Thus determining the spin polarization of the state can rule-out either the MR Pfaffian or the unpolarized 331 description for $\nu = 5/2$.

A possible explanation that may resolve the seemingly conflicting evidence on spin-order and that we briefly explore in this chapter is the possibility that the $\nu = 5/2$ FQHE state is not unique[175]. In other words there may be more than one incompressible FQHE state, each with different spin polarizations, that satisfy conditions to be experimentally observed at $\nu = 5/2$. Which FQHE state that is finally observed in an experimental sample may depend on certain details of the sample or where on the $\nu = 5/2$ plateau the experiment is being carried out. In this chapter, we briefly explore this possibility by comparing the energy of two trial FQHE wavefunctions with respect to small deviations: the spin-polarized Moore Read (MR) Pfaffian, and the unpolarized Halperin 331 state. To examine the possibility of a phase change between spin polarized and unpolarized incompressible FQHE states within the $\nu = 5/2$ plateau, we focus entirely on the MR Pfaffian and the Halperin 331 state and examine how their respective energies change with respect to small alterations to the effective interacting potential. We alter the 2D

Coulomb potential in two ways: 1) through the finite thickness effect, and 2) by directly perturbing the first two Haldane pseudopotentials. By appealing to the variational theorem, whichever state has the lowest ground state energy (strictly speaking, the lowest free energy) is a better physical description of the physics–of course, the variational theorem cannot rule out the possibility of a lower energy ground state that we are not investigating (in fact, this is the likely scenario in the nu=1/2 state in the lowest Landau level where experimentally an FQHE has never been observed indicating that some kind of a compressible non-FQH state is likely to be lower in energy than either the MR Pfaffian or the Halperin 331 state in the lowest Landau level). To achieve this goal we alter the 2D Coulomb potential in two ways: i) through the finite thickness effect, and ii) by directly perturbing the first two Haldane pseudopotentials [116] (see below).

In the finite thickness effect, the non-zero thickness of the quasi-2D electron system provides an effective potential slightly modified from the purely ideal 2D Coulomb potential, which we refer to as the "Coulomb point" in this work. Since polarized FQHE states have been shown to be sensitive to this finite thickness effect (see Chapter 6) and the thickness is expected to vary for different experimental samples, the finite thickness effect is a natural area to investigate [128, 129]. Although our results do not suggest a direct quantum phase transition between the MR Pfaffian and the Halperin 331 in the second Landau Level (SLL) induced by tuning the finite thickness, the energy difference between the two states decreases with sample thickness, implying that other perturbations may make either state energetically favorable for very deep wells; some of these other perturbations could

be Landau level mixing, disorder, effect of nearby gates, self-consistency of the confining potential itself, etc., which are not considered in our work since they are far too sample-specific to be treated theoretically at this stage.

Our second approach to altering the 2D Coulomb potential – directly perturbing the first two Haldane pseudopotentials [116] – provides us a general theoretical probe that can identify areas of interest which may be reached experimentally via other effects. The Haldane pseudopotentials, V_m, parametrize the effective interaction potential in terms of the relative angular momenta m between two particles, and thus, perturbing the first two pseudopotentials (i.e. m = 1,2) alters the short range interactions between electrons (note that in this study, we leave the $m = 0$ term fixed). The method of altering pseudopoentials is a common approach taken in FQHE exact diagonalization numerical studies aimed at probing sensitivities to different moments in the interaction strength, however, this approach has not yet been attempted in VMC studies to the best of our knowledge. We note that our two alternative ways of introducing 'small deviations' or tuning away from the pure Coulomb point (realistic finite thickness effect and varying the lowest pseudopotentials) are complementary theoretical methods of tuning the system Hamiltonian since the finite thickness correction modifies all the Coulomb pseudopotentials in a complex manner which cannot simply be simulated by changing the two lowest pseudopotentials.

We also examine the lowest Landau level (LLL) (i.e. $\nu = 1/2$) in addition to the second Landau level (SLL) (i.e. $\nu = 5/2$) for comparison. In the LLL, no incompressible even-denominator FQHE has been experimentally observed in

mono-layer systems to date, but there are several theoretical proposals to engineer certain experimental conditions in such a way that even-denominator states are energetically favorable [179]. In these cases the Halperin 331 state and the MR Pfaffian are likely possibilities. In our study of the LLL, we find that either state may be energetically favorable in the LLL depending on the pseduopotential deviations. This is in contrast to our results in the SLL where we find that the MR Pfaffian is generally lower in energy than the Halperin 331 state for most deviations examined, suggesting that the MR Pfaffian description is, indeed, better suited for the half-filled SLL, i.e., $\nu = 5/2$. This is of course also consistent with the most recent experimental status of the subject where the SLL 5/2 FQHE appears to be spin-polarized. Our work, however, indicates that the corresponding LLL situation is more delicate, and if an incompressible FQHE is ever observed at the LLL $\nu = 1/2$ filling in a monolayer 2D system, it could either be a MR spin-polarized Pfaffian or a Halperin spin-unpolarized 331 state.[180].

We add a theoretical subtlety here which has sometimes caused some confusion in the literature. The Halperin 331 state in general does not obey the full SU(2) symmetry (specifically, the so-called Fock condition necessary for a spin-independent many-body Hamiltonian which must conserve the total spin of the system), and cannot therefore be a true eigenstate of the single-layer Coulomb Hamiltonian since by definition this Hamiltonian obeys the full SU(2) symmetry because the Coulomb interaction is spin-independent– the 331 state was originally conceived for the double-layer 2D system where the Coulomb interaction does indeed depend on the layer index and is in general not SU(2) invariant in the layer index. This is, however, not

a problem for our VMC analysis since we are only interested in comparing energies between variational ground states (which do not care about the symmetry of the Hamiltonian) and are not trying to obtain the exact theoretical eigenstate of the system (which would be an impossible task any way, even the MR Pfaffian can at best be a good variational state for the system and by no means the exact eigenstate). In the end, the best theory we can hope for is to obtain a variational ground state (MR Pfaffian or 331) which is adiabatically connected to the exact ground state of the experimental system without any intervening quantum phase transition so that the spin-polarization status of the variational ground state and the exact ground state remains the same. Thus, for our purpose, both the MR Pfaffian and the 331 are perfectly (and equally) legitimate variational choices, and which ever has lower VMC energy could be construed as the "correct" ground state of the system (at least within the narrow, but very reasonable, restricted variational choice of only two candidate wavefunctions).

We also mention that all our work leaves out the trivial Zeeman energy of the system arising from the applied magnetic field creating the Landau levels in the first place, which helps the spin-polarized state over the spin-unpolarized state. Since the applied field is typically rather small for the $\nu = 5/2$ FQHE, leaving out the Zeeman energy (which is trivial to include for any given field) is probably a reasonable approximation, but it is helpful to remember that even if a spin-unpolarized ground state arises from our VMC analysis, the Zeeman energy could in principle eventually win over, leading to the experimental state being spin-polarized. The reverse, however, is not true, i.e. if the zero-Zeeman splitting situation has a (spon-

taneously symmetry-broken) spin-polarized ground state, it is unlikely that finite Zeeman splitting will change the ground state to a spin singlet.

7.2 Variational Monte Carlo Evaluation of the Energies Using Effective Potentials

We use variational Monte Carlo (VMC) methods in the same spirit as Refs [75] and [168] to estimate the energy per particle of the Halperin 331 state and the MR Pfaffian state for altered Coulomb potentials in the lowest and second Landau level with up to $N = 120$ electrons and extrapolate to the thermodynamic limit, (i.e. $1/N \to 0$). To examine the finite thickness effect, we use the potential derived for the infinite square well potential given in Eq. (5.50).

We also examine the effect of directly perturbing the Haldane pseudopotentials [116] V_m for the Coulomb potential in LLL and SLL. In particular, we examine the effect of the perturbations $\tilde{V}_1 \to V_1 + \Delta V_1$ and $\tilde{V}_2 \to V_2 + \Delta V_2$ for pseudopotentials derived from the Coulomb potential (i.e. $V(k) = 1/k$). In order to use VMC methods to estimate wavefunction energies, we require an effective potential in real space, $V_{\text{eff}}(r)$, such that the application of Eq. (5.47) results in our perturbed pseudopotentials, $\tilde{V}_m$ on the LHS. The immediate difficulty we run into is that there is no clear procedure to invert Eq. (5.47) to obtain $V_{\text{eff}}(r)$ for arbitrary $\tilde{V}_m$–it is a one-to-many mapping. Also, even in the unperturbed case, estimating energies in the SLL is not straight-forward since most FQHE trial wavefunctions under study do not have a closed-form expression in the SLL. To get around these difficulties,

we chose a variable effective potential with fitting parameters, c_i, and set these parameters such that the result of applying Eq. (5.47) on the effective potential very closely matches the perturbed pseudopotentials. And when examining the SLL, we "simulate" the SLL in the LLL by fitting the effective potential within the LLL to the perturbed SLL pseudopotentials [75], that is, we project the SLL into the LLL. Several forms for the effective potential have been used for previous Monte Carlo studies of the FQHE [75, 181, 182]. For our study, we use the following form for the effective potential (in units of $e^2/\epsilon l$):

$$V_{\text{eff}}(r) = \frac{1}{r} + \sum_{i=1}^{M} c_i r^{2i} e^{r^2}. \tag{7.1}$$

We choose this form because for large enough M, the potential fits both even and odd pseudopotentials to a reasonable degree – only odd pseudopotentials are important when fully polarized or spinless wavefunctions are under investigation – and the fits to V_m for large m (i.e. $m > M$) are generally consistent across different perturbations, ΔV_1 and ΔV_2, allowing us to make fair comparisons between different perturbations. In choosing the number of terms, M, in the effective potential, there is a trade-off between tighter fits to the pseudopotentials for larger M and ease with which the Monte Carlo converges – the addition of terms in Eq. (7.1) leads to an oscillatory potential that takes, in general, more iterations to reach convergence. For our study, we use $M = 6$. As an example, we show in Fig. 7.1 perturbed pseudopotentials $\tilde{V}_m$ for $\Delta V_1 = -0.06$ and $\Delta V_2 = 0.02$ in the SLL and the corresponding fitted pseudopotentials resulting from a non-linear least squares fit of Eq. (7.1) to $\tilde{V}_m$ via Eq. (5.47). It is worth noting that the V_m's calculated from the effective

potential for $m > M = 6$ are very good approximations to the actual values and only differ at the level of a fraction of a percentage point ($\sim 0.6\%$ on average)

Throughout this work we make use of the spherical geometry where electrons are confined to a two dimensional (2D) spherical surface of radius R with a magnetic monopole of magnetic charge Q at the center of the sphere[116, 117]. The radius of the sphere is determined by the magnetic charge Q: $R^2 = Q$. The magnetic charge for a quantum Hall state with N electrons at filling factor ν is given by $2Q = N/\nu + \chi$ where χ is the topological shift[183] and depends on the FQHE state under investigation. Lastly, the distance between two electrons on the spherical surface is taken to be the cord distance.

In the spherical geometry, the unpolarized Halperin 331 and polarized MR Pfaffian states are given by

$$\begin{aligned}\psi_{331} &= \hat{\mathcal{A}} \prod_{i<j} (u_i^{\uparrow} v_j^{\uparrow} - v_i^{\uparrow} u_j^{\uparrow})^3 \prod_{k<l} (u_k^{\downarrow} v_l^{\downarrow} - v_k^{\downarrow} u_l^{\downarrow})^3 \\ &\quad \times \prod_{r,s} (u_r^{\uparrow} v_s^{\downarrow} - v_r^{\uparrow} u_s^{\downarrow}) \end{aligned} \tag{7.2}$$

and

$$\psi_{\text{Pfaff}} = \prod_{i<j} (u_i^{\uparrow} v_j^{\uparrow} - v_i^{\uparrow} u_j^{\uparrow})^2 \text{Pf}[M] \tag{7.3}$$

where $u_i = \cos(\theta_i/2)\exp(i\phi_i/2)$ and $v_i = \sin(\theta_i/2)\exp(-i\phi_i/2)$, and $u_i^{\sigma} = u_i \otimes |\sigma\rangle$ and $v_i^{\sigma} = v_i \otimes |\sigma\rangle$, $|\sigma\rangle$ is the spin ket, $\hat{\mathcal{A}}$ is the antisymmetrization operator, and Pf$[M]$ is the Pfaffian of the matrix $M_{i,j} = (u_i^{\uparrow} v_j^{\uparrow} - v_i^{\uparrow} u_j^{\uparrow})^{-1}$. The magnetic charge for both states is given by $2Q = 2N - 3$.

To evaluate the energy of some wavefunction Ψ via variational Monte Carlo

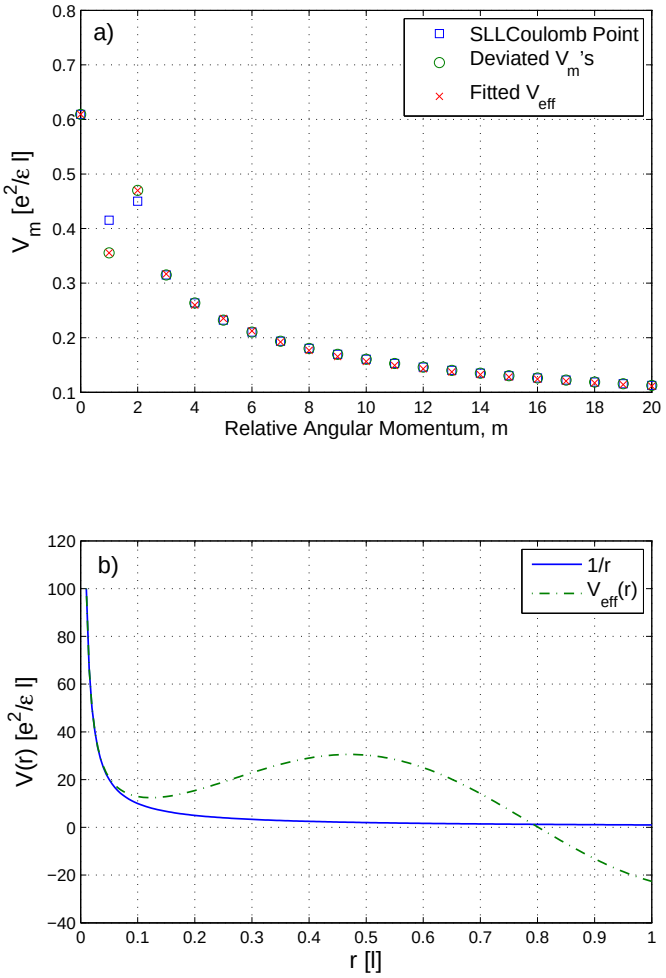

Figure 7.1: a) Perturbed pseudopotentials $\tilde{V}_m$ for $\Delta V_1 = -0.06$ and $\Delta V_2 = 0.02$ in the SLL (the Coulomb point is the Coulomb interaction in the SLL) and the corresponding fitted pseudopotentials from Eq. (7.1). Note that any difference between the pseudopotentials calculated from the real space effective potential corresponding to the deviated pseudopotentials and the deviated pseudopotentials themselves is smaller than the symbols on the figure. b) The resulting $V_{\text{eff}}(r)$ compared to the Coulomb potential $V(r) = 1/r$

we calculate the Hamiltonian expectation value

$$\begin{aligned} E_\psi &= \frac{\int d\Omega_1 \dots d\Omega_N \psi^*(\Omega_1, \dots, \Omega_N) \hat{H} \psi(\Omega_1, \dots, \Omega_N)}{\int d\Omega_1 \dots d\Omega_N |\psi(\Omega_1, \dots, \Omega_N)|^2} \\ &= \frac{\int d\Omega_1 \dots d\Omega_N |\psi(\Omega_1, \dots, \Omega_N)|^2 \hat{H}}{\int d\Omega_1 \dots d\Omega_N |\psi(\Omega_1, \dots, \Omega_N)|^2} \end{aligned} \tag{7.4}$$

where $\Omega = (\theta, \phi)$ is the particle position on the sphere and $\hat{H} = \sum_{i<j}^{N} V^{\text{eff}}(|\mathrm{r}_i - \mathrm{r}_j|)$. In the above, we make use of the identity $\det M = |\mathrm{Pf}[M]|^2$.

Before presenting the effects of finite-thickness and directly perturbing Haldane pseudopotentials we briefly discuss the background energy. It is assumed that there is a uniform distribution of positive charge on the spherical surface so that the total energy is negative and the electron's state represents a stable phase of matter. That is, we place N positive charges on the surface of the sphere and calculate the interaction energy between an electron and the background E_{el-bg} and the interaction energy of the background with itself E_{bg-bg}. For a pure Coulomb interaction this works out to be

$$E_{el-bg} = -\frac{N^2 e^2}{\sqrt{Q}\epsilon l} , \tag{7.5}$$

$$E_{bg-bg} = \frac{N^2 e^2}{2\sqrt{Q}\epsilon l} , \tag{7.6}$$

yielding $E_{bg} = E_{el-bg} + E_{bg-bg} = -\frac{N^2 e^2}{2\sqrt{Q}\epsilon l}$. Remember that the radius of the sphere is $R = \sqrt{Q}$. Now, strictly speaking, this energy comes about by doing a rather trivial integral over the surface of the sphere with the distance between particles defined as the cord distance instead of the arc distance–in the thermodynamic limit both choices are equivalent.

For our calculations it is a little bit more subtle. We are considering elec-

trons projected into the LLL with effective potentials that take into account finite thickness, electrons completely confined to the SLL, and potentials produced by small deviations away from the Coulomb point through the direct manipulation of V_1 and V_2. We find this effective potential through Eq. (7.1) and to get the proper background energy we calculate

$$E_{el-bg} = -\frac{e^2N^2}{2}\int_0^\pi d\theta \sin(\theta)V_{\text{eff}}(r(\theta)) \,, \tag{7.7}$$

$$E_{bg-bg} = -\frac{1}{2}E_{el-bg} \,, \tag{7.8}$$

where $r(\theta) = 2R\sin(\theta/2)$. While there is no deep physics hidden in the background energy, it is needed to ensure that the ground state energy per particle has a well-defined and finite thermodynamic limit. Further, since we are comparing two ground state energies, this background energy cancels out in a sense.

7.3 Ground state energies for effective potentials in the LLL and SLL

As a thorough numerical check, we first list our results for MR Pfaffian and the Halperin 331 state at the Coulomb point with no perturbation in Table 7.1 and find that we are in agreement with Refs. [75] and [168]. We note that other wavefunctions are also possible, for example, a Composite Fermion fermi sea (CFFS), in a polarized (P) or unpolarized (UP) variety [72, 73, 170] and the Haldane-Rezayi singlet state [184] (HR), all whose energies in the LLL and SLL are listed in Table 7.1. In the LLL, it is clear that the lowest energy state is the unpolarized CFFS which is a gapless state that does not yield the FQHE, although, the energy of the 331 state is very close. However, we know experimentally [185] that no FQHE has yet

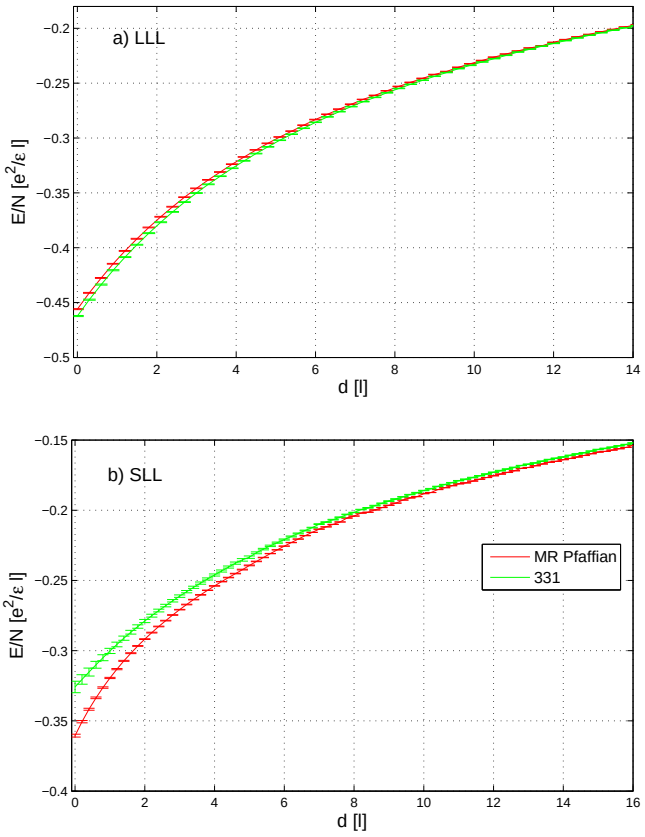

Figure 7.2: Energy per particle (in units of $e^2/\epsilon l$) as a function of finite thickness, d (in units of the magnetic length, l) for the MR Pfaffian (red) and the Halperin 331 state (green) in the LLL (a) and the SLL (b). The energy per particle increases with thickness and the difference in energy between the two states decreases. However, in the LLL, the Halperin 331 is always lower in energy than the MR Pfaffian while, in the SLL, the opposite is true. In other words, finite thickness alone does not apparently drive a spin order transition.

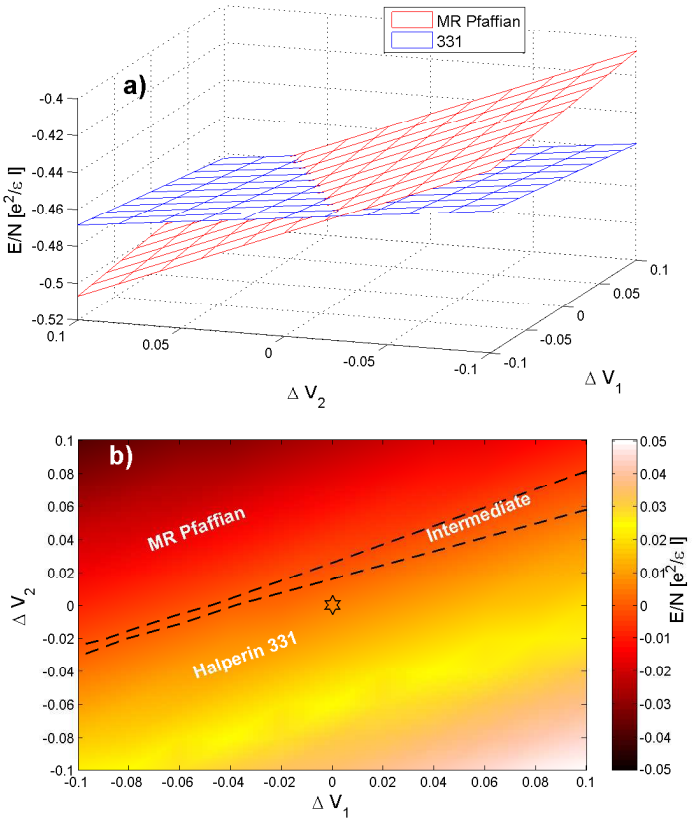

Figure 7.3: Comparison of Halperin 331 and MR Pfaffian in the LLL. a) Energy per particle as a function perturbation strengths ΔV_1 and ΔV_2. b) Energy difference $E_\Delta = E_{\text{Pfaff}} - E_{331}$ as function of ΔV_1 and ΔV_2. Regions where either Halperin 331 ($E_\Delta > 0$) or MR Pfaffian ($E_\Delta < 0$) is energetically favorable are denoted. The intermediate region denotes area where the energies are within numerical uncertainty of each other. The star designates the Coulomb point for reference. The statistical uncertainty in the energies is not indicated on these contour plots for ease of presentation. However, it is similar in magnitude to what is presented in Fig. 7.2 but the qualitative effects of the uncertainty is indicated by the "intermediate" regime where both energies are within statistical uncertainty of each other.

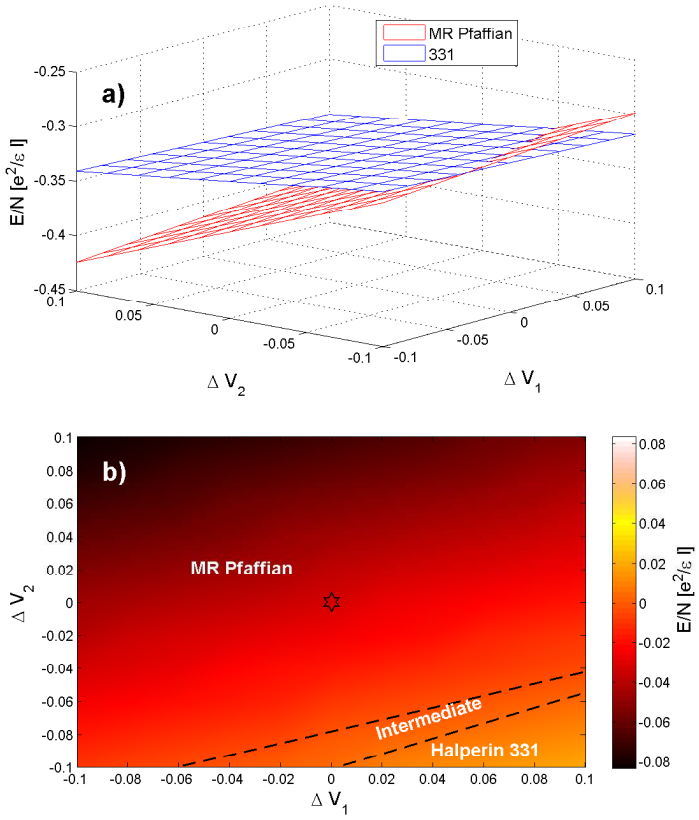

Figure 7.4: Comparison of Halperin 331 and MR Pfaffian in the SLL. a) Energy per particle as a function perturbation strengths ΔV_1 and ΔV_2. b) Energy difference $E_\Delta = E_{\text{Pfaff}} - E_{331}$ as function of ΔV_1 and ΔV_2. Regions where either Halperin 331 ($E_\Delta > 0$) or MR Pfaffian ($E_\Delta < 0$) is energetically favorable are denoted. The intermediate region denotes area where the energies are within numerical uncertainty of each other. The star designates the Coulomb point for reference.

Energy $[e^2/(\epsilon l)]$	LLL	SLL
E_{331}	-0.4631(3)	-0.329(3)
E_{Pfaff}	-0.4573(3)	**-0.361(2)**
$E_{\text{CFFS(P)}}$	-0.46557(6) [75]	-0.3492(5) [75]
$E_{\text{CFFS(UP)}}$	**-0.46953(7)** [75]	-0.2952(3) [75]
E_{HR}	-0.3147(3) [75]	-0.303(3) [75]

Table 7.1: Energy calculated via VMC of various wavefunctions. Our results for E_{331} and E_{Pfaff} agree with those of Dimov *et al.* [168] at the Coulomb point in the LLL and SLL. The results listed below for the polarized and unpolarized CFFS and the Haldane-Rezayi singlet state are given by Park *et al.* [75]. The lowest energy state at the Coulomb point in the LLL and SLL is the unpolarized CFFS and MR Pfaffian, respectively (both are indicated in bold).

been observed in single layer systems at $\nu = 1/2$. In contrast, at the Coulomb point in the SLL, the lowest energy state in Table 7.1 is the MR Pfaffian and, in fact, the MR Pfaffian has been routinely experimentally observed at $\nu = 5/2$ albeit at low temperatures and in very high-quality samples, indicating that the $\nu = 5/2$ FQHE is rather fragile with a very small gap and possibly with competing states with comparable energetics.

Since the purpose of this work is to investigate the spin polarization of the half-filled lowest and second Landau levels via VMC, we will focus exclusively on the Halperin 331 versus the MR Pfaffian wavefunctions. A full investigation including all possible ansatz and more realistic effective potentials that include finite thickness *and* Landau level mixing [186] is beyond the scope of this work and will have to await future works. Our work is in the spirit of a restricted variational study which makes

sense for this problem since the two candidates we use (i.e. MR Pfaffian and Halperin 331) are essentially the "only game in town" for incompressible even-denominator FQHE states in single-layer 2D systems. In fact, part of the motivation of this work is to establish the feasibility of this sort of VMC investigation of Hamiltonians described by effective potentials.

Next, we examine the finite thickness effect and how it changes the expected ground state energy of the MR Pfaffian and the Halperin 331 state. In Fig. 7.2(a) are the numerically calculated energies in units of $e^2/\epsilon l$, as a function of thickness (in units of the magnetic length, l) in the LLL. The Halperin 331 state is consistently lower in energy but the gap between the energies of the MR Pfaffian and the Halperin 331 state decreases with thickness. Similar results are seen in Fig. 7.2(b) for the SLL where the MR Pfaffian is energetically favorable, but the energy difference between the two states again decrease with thickness. Part of this likely stems from the fact that the overall energy scale is shrinking due to the finite thickness effect. Fig. 7.2 hides the complexity of the calculation. For each point on both (rather the four) curves the following procedure was carried out: (1) for each value of thickness d the pseudopotentials were calculated, (2) a real space effective potential $V_{\text{eff}}(r)$ was found from these pseudopotentials, (2) many VMC evaluations of the energy of either Ψ_{331} or Ψ_{Pfaff} for N electrons were carried out, and finally (4) these energies were extrapolated to the thermodynamic limit ($1/N \to \infty$) to generate a single point.

We now examine the effect of directly perturbing the first two Haldane pseudopotentials in the LLL and the SLL. Fig. 7.3(a) gives the energy estimates for the

MR Pfaffian and the Halperin 331 state with respect to ΔV_1 and ΔV_2 in the LLL. Here we see that the energy of the MR Pfaffian is more sensitive to ΔV_m compared to the Halperin 331 state. Also the MR Pfaffian decreases in energy with decreasing ΔV_1 or increasing ΔV_2, whereas the Halperin 331 energy shows opposing trends. Figure 7.3 (b) shows the energy difference between the MR Pfaffian and the Halperin 331 state and an estimated phase diagram–the phase is determined by whichever wavefunction has the lowest ground state energy per particle. The "intermediate" phase indicates where the energies are within numerical uncertainty of each other. Here we see that the MR Pfaffian can be energetically favorable for relatively small deviations from the Coulomb point for $\Delta V_2 > 0$.

Results for perturbations about the SLL Coulomb point are given in Fig. 7.4(a). Here we see the same energy versus ΔV_1 and ΔV_2 has similar trends as was found in the LLL , but the MR Pfaffian is consistently lower in energy in the SLL for the majority of perturbations under investigation. Fig. 7.4(b) gives the difference in energy and an estimated phase boundary between the MR Pfaffian and the Halperin 331. Again, the "intermediate" area indicates where the energies are within numerical uncertainty of each other. Unlike in the LLL case, the MR Pfaffian is generally favored for any perturbation in the SLL. In the region where the Halperin 331 state is favorable in the SLL, the perturbations result in $V_2 < V_1$, which is a qualitative feature of the Coulomb point in the LLL. If the effect of $V_{m>2}$ are minimal, then we can argue that this region is qualitatively similar to the Coulomb point of the LLL and therefore, the Halperin 331 state is energetically favorable in this region given the results on the LLL.

7.4 Conclusions

Our results show that through the finite thickness effect, the energies of the Halperin 331 and the MR Pfaffian state increase with increasing sample thickness in either LL. The energy difference between the two states decreases with increasing sample thickness, but there is no crossing between the two states in either LL, i.e., finite thickness apparently does not drive a spin polarization quantum phase transition at least for the situation with vanishing Zeeman energy considered in our work. It is possible, in fact quite likely for the LLL, that a finite Zeeman splitting will induce a transition from the Halperin 331 to the MR Pfaffian state, but neither may be the true ground state in the LLL since no $\nu = 1/2$ FQHE has ever been observed experimentally. Additionally, our results show that the energy of the MR Pfaffian is more sensitive to changes in the pseudopotentials than the Halperin 331 state, where the MR Pfaffian energy decreases with increasing ΔV_2 and decreasing ΔV_1. The energy of the Halprin 331 state, in contrast, is generally insensitive (in comparison to that of the MR Pfaffian) with slight decreases for $\Delta V_1 > 0$ and $\Delta V_2 < 0$, cf. Figs. 7.3(a) and 7.4(a). In the LLL, the MR Pfaffian becomes energetically favorable for small increases in V_1 above the Coulomb point. In the SLL, the Halperin 331 state becomes favorable for relatively large deviations from the Coulomb point, (i.e. $\Delta V_1 \gtrsim 0$ and $\Delta V_2 \lesssim -0.06$), again in the absence of the Zeeman energy – given the small difference between the two VMC energies, it is quite likely that the MR Pfaffian state has lower energy than the Halperin 331 state for all thickness values and all deviations from the Coulomb point once the

Zeeman energy is taken into account since the Zeeman energy would always prefer the spin-polarized state.

Our study adds to the growing body of evidence[133, 169, 173, 171, 172] supporting the spin polarized MR Pfaffian description for FQHE at $\nu = 5/2$. Of course, conclusive verification of the MR Pfaffian description requires the direct experimental observation of non-Abelian anyons. But given the difficulty in conclusively detecting non-Abelian signatures [80, 81, 187], novel experimental techniques will be needed for definitive verification.

Lastly, we emphasize that our study additionally serves as a "proof of principle" for VMC studies of various FQH systems that are described by effective potentials. Effective potentials are needed when considering certain realistic effects such as finite thickness, Landau level mixing, higher Landau level FQHE, disorder, etc., or by simply artificially manipulating various Haldane pseudopotentials. Our work establishes that the VMC technique is a viable alternative to the exact diagonalization method in theoretically studying the ground state properties of FQHE including various realistic effects which are often hard to do using the finite size diagonalization method.

Bibliography

[1] F. Bloch. Über die Quantenmechanik der Elektronen in Kristallgittern. *Zeitschrift fur Physik*, 52:555–600, July 1929.

[2] Charles Kittel. *Introduction to Solid State Physics*. Wiley, 1996.

[3] Neil W. Ashcroft and N. David Mermin. *Solid State Physics*. Wiley, 1996.

[4] Michael E. Peskin and Daniel V. Schroeder. *An Introduction to Quantum Field Theory*. Addison-Wesley, 1995.

[5] Alexander L. Fetter and John Dirk Walecka. *Quantum Theory of Many-Particle Systems*. McGraw-Hill, 1971.

[6] L.L.D. Landau, E.E.M. Lifshits, and L.L.P. Pitaevskii. *Statistical Physics: Theory of the Condensed State*. Course of theoretical physics ; v. 5, 9. Butterworth-Heinemann, 1980.

[7] P. W. Anderson. Absence of Diffusion in Certain Random Lattices. *Physical Review*, 109:1492–1505, 1958.

[8] N. F. Mott and W. D. Twose. The theory of impurity conduction. *Advances in Physics*, 10:107–163, 1961.

[9] RE Borland. The nature of the electronic states in disordered one-dimensional systems. *Proceedings of the Royal Society of London. Series A. Mathematical and Physical Sciences*, 274(1359):529–545, 1963.

[10] K. v. Klitzing, G. Dorda, and M. Pepper. New method for high-accuracy determination of the fine-structure constant based on quantized hall resistance. *Physical Review Letters*, 45:494–497, 1980.

[11] D. J. Thouless, M. Kohmoto, M. P. Nightingale, and M. den Nijs. Quantized hall conductance in a two-dimensional periodic potential. *Physical Review Letters*, 49(6):405–408, 1982.

[12] D. C. Tsui, H. L. Stormer, and A. C. Gossard. Two-dimensional magnetotransport in the extreme quantum limit. *Physical Review Letters*, 48(22):1559–1562, 1982.

[13] B. I. Halperin. Statistics of quasiparticles and the hierarchy of fractional quantized hall states. *Physical Review Letters*, 52(18):1583–1586, 1984.

[14] J. Leinaas and J. Myrheim. On the theory of identical particles. *Il Nuovo Cimento B (1971-1996)*, 37:1–23, 1977. 10.1007/BF02727953.

[15] Frank Wilczek. Quantum mechanics of fractional-spin particles. *Physical Review Letters*, 49(14):957–959, 1982.

[16] Daniel Arovas, J. R. Schrieffer, and Frank Wilczek. Fractional statistics and the quantum hall effect. *Physical Review Letters*, 53(7):722–723, 1984.

[17] Dieter Jaksch, Ch Bruder, Juan Ignacio Cirac, Crispin W Gardiner, and Peter Zoller. Cold bosonic atoms in optical lattices. *Physical Review Letters*, 81(15):3108–3111, 1998.

[18] Oliver Morsch and Markus Oberthaler. Dynamics of bose-einstein condensates in optical lattices. *Reviews of Modern Physics*, 78(1):179, 2006.

[19] Leonardo Fallani, Chiara Fort, and Massimo Inguscio. Bose–einstein condensates in disordered potentials. *Advances In Atomic, Molecular, and Optical Physics*, 56:119–160, 2008.

[20] Gregory Moore and Nicholas Read. Nonabelions in the fractional quantum hall effect. *Nuclear Physics B*, 360(2-3):362 – 396, 1991.

[21] Chetan Nayak and Frank Wilczek. 2n-quasihole states realize 2n-1-dimensional spinor braiding statistics in paired quantum hall states. *Nuclear Physics B*, 479(3):529 – 553, 1996.

[22] Parsa Bonderson, Victor Gurarie, and Chetan Nayak. Plasma analogy and non-abelian statistics for ising-type quantum hall states. *Physical Review B*, 83(7):075303, 2011.

[23] Sankar Das Sarma, Michael Freedman, and Chetan Nayak. Topologically protected qubits from a possible non-abelian fractional quantum hall state. *Physical Review Letters*, 94(16):166802, 2005.

[24] Chetan Nayak, Steven H. Simon, Ady Stern, Michael Freedman, and Sankar Das Sarma. Non-abelian anyons and topological quantum computation. *Reviews of Modern Physics*, 80(3):1083–1159, 2008.

[25] Patrick A. Lee and T. V. Ramakrishnan. Disordered electronic systems. *Reviews of Modern Physics*, 57:287–337, 1985.

[26] Dieter Vollhardt and PETER Wölfle. Self-consistent theory of anderson localization. *Electronic phase transitions*, 1, 1992.

[27] Bernhard Kramer and Angus MacKinnon. Localization: theory and experiment. *Reports on Progress in Physics*, 56(12):1469, 1999.

[28] Elihu Abrahams, PW Anderson, DC Licciardello, and TV Ramakrishnan. Scaling theory of localization: Absence of quantum diffusion in two dimensions. *Physical Review Letters*, 42(10):673–676, 1979.

[29] D.J. Thouless. Electrons in disordered systems and the theory of localization. *Physics Reports*, 13(3):93 – 142, 1974.

[30] FranzJ. Wegner. Electrons in disordered systems. scaling near the mobility edge. *Zeitschrift fr Physik B Condensed Matter*, 25:327–337, 1976.

[31] DJ Thouless. Ill-condensed matter. *Ams¬ terdam: North Holland*, 1979.

[32] Nevill Francis Mott and Edward A Davis. *Electronic processes in non-crystalline materials*. OUP Oxford, 2012.

[33] S Aubry and G André. Analyticity breaking and anderson localization in incommensurate lattices. *Annals of the Israel Physical Society*, 3:133–164, 1980.

[34] S. Das Sarma, Song He, and X. C. Xie. Localization, mobility edges, and metal-insulator transition in a class of one-dimensional slowly varying deterministic potentials. *Physical Review B*, 41(9):5544–5565, 1990.

[35] S. Das Sarma, Song He, and X. C. Xie. Mobility edge in a model one-dimensional potential. *Physical Review Letters*, 61(18):2144–2147, 1988.

[36] D. J. Thouless. Localization by a potential with slowly varying period. *Physical Review Letters*, 61(18):2141–2143, 1988.

[37] J. B. Sokoloff. Unusual band structure, wave functions and electrical conductance in crystals with incommensurate periodic potentials. *Physics Reports*, 126(4):189 – 244, 1985.

[38] Immanuel Bloch, Jean Dalibard, and Wilhelm Zwerger. Many-body physics with ultracold gases. *Reviews of Modern Physics*, 80(3):885, 2008.

[39] J Billy et al. Direct observation of anderson localization of matter waves in a controlled disorder. *Nature*, 453:891, 2008.

[40] G Roati et al. Anderson localization of a non-interacting boseeinstein condensate. *Nature*, 453:895, 2008.

[41] Steven Chu. Nobel lecture: The manipulation of neutral particles. *Reviews of Modern Physics*, 70:685–706, 1998.

[42] Claude N. Cohen-Tannoudji. Nobel lecture: Manipulating atoms with photons. *Reviews of Modern Physics*, 70:707–719, 1998.

[43] William D. Phillips. Nobel lecture: Laser cooling and trapping of neutral atoms. *Reviews of Modern Physics*, 70:721–741, 1998.

[44] Harold J Metcalf and Peter Van der Straten. *Laser cooling and trapping*. Springer Verlag, 1999.

[45] D. Durfee W. Ketterle and D. M. Stamper-Kurn. Bose-einstein condensation in atomic gases. In Massimo Inguscio, Sandro Stringari, and Carl Edwin Wieman, editors, *Proceedings of the International School of Physics Enrico Fermi, Course CXL*, page 67176. IOS Press, 1999.

[46] E. A. Cornell and C. E. Wieman. Nobel lecture: Bose-einstein condensation in a dilute gas, the first 70 years and some recent experiments. *Reviews of Modern Physics*, 74:875–893, 2002.

[47] Wolfgang Ketterle. Nobel lecture: When atoms behave as waves: Bose-einstein condensation and the atom laser. *Reviews of Modern Physics*, 74:1131–1151, 2002.

[48] G. Grynberg and C. Robilliard. Cold atoms in dissipative optical lattices. *Physics Reports*, 355(5-6):335 – 451, 2001.

[49] S Inouye, MR Andrews, J Stenger, H-J Miesner, DM Stamper-Kurn, and W Ketterle. Observation of feshbach resonances in a bose–einstein condensate. *Nature*, 392(6672):151–154, 1998.

[50] Cheng Chin, Rudolf Grimm, Paul Julienne, and Eite Tiesinga. Feshbach resonances in ultracold gases. *Reviews of Modern Physics*, 82:1225–1286, 2010.

[51] Leonardo Fallani, Chiara Fort, and Massimo Inguscio. Bose-einstein condensates in disordered potentials. volume 56 of *Advances In Atomic, Molecular, and Optical Physics*, pages 119 – 160. Academic Press, 2008.

[52] K. S. Novoselov, Z. Jiang, Y. Zhang, S. V. Morozov, H. L. Stormer, U. Zeitler, J. C. Maan, G. S. Boebinger, P. Kim, and A. K. Geim. Room-temperature quantum hall effect in graphene. *Science*, 315(5817):1379, 2007.

[53] R. B. Laughlin. Anomalous quantum hall effect: An incompressible quantum fluid with fractionally charged excitations. *Physical Review Letters*, 50(18):1395–1398, 1983.

[54] S. Das Sarma and A. Pinczuk. *Perspectives in quantum Hall effects: novel quantum liquids in low-dimensional semiconductor structures*. Wiley, 1997.

[55] R. Prange and S. Girvin. *The Quantum Hall Effect*. Springer-Verlag, New York, 1990.

[56] J.K. Jain. *Composite fermions*. Cambridge University Press, 2007.

[57] JE Avron, R Seiler, and B Simon. Homotopy and quantization in condensed matter physics. *Physical Review Letters*, 51(1):51–53, 1983.

[58] Joseph E Avron and Ruedi Seiler. Quantization of the hall conductance for general, multiparticle schrödinger hamiltonians. *Physical Review Letters*, 54(4):259–262, 1985.

[59] Mahito Kohmoto. Topological invariant and the quantization of the hall conductance. *Annals of Physics*, 160(2):343–354, 1985.

[60] R. Willett, J. P. Eisenstein, H. L. Störmer, D. C. Tsui, A. C. Gossard, and J. H. English. Observation of an even-denominator quantum number in the fractional quantum hall effect. *Physical Review Letters*, 59(15):1776–1779, 1987.

[61] W. Pan, J.-S. Xia, V. Shvarts, D. E. Adams, H. L. Stormer, D. C. Tsui, L. N. Pfeiffer, K. W. Baldwin, and K. W. West. Exact quantization of the even-denominator fractional quantum hall state at $\nu = 5/2$ landau level filling factor. *Physical Review Letters*, 83(17):3530–3533, 1999.

[62] J. P. Eisenstein, K. B. Cooper, L. N. Pfeiffer, and K. W. West. Insulating and fractional quantum hall states in the first excited landau level. *Physical Review Letters*, 88(7):076801, 2002.

[63] J. S. Xia, W. Pan, C. L. Vicente, E. D. Adams, N. S. Sullivan, H. L. Stormer, D. C. Tsui, L. N. Pfeiffer, K. W. Baldwin, and K. W. West. Electron correlation in the second landau level: A competition between many nearly degenerate quantum phases. *Physical Review Letters*, 93(17):176809, 2004.

[64] G. A. Csáthy, J. S. Xia, C. L. Vicente, E. D. Adams, N. S. Sullivan, H. L. Stormer, D. C. Tsui, L. N. Pfeiffer, and K. W. West. Tilt-induced localization and delocalization in the second landau level. *Physical Review Letters*, 94(14):146801, 2005.

[65] H. C. Choi, W. Kang, S. Das Sarma, L. N. Pfeiffer, and K. W. West. Activation gaps of fractional quantum hall effect in the second landau level. *Physical Review B*, 77(8):081301, 2008.

[66] W. Pan, J. S. Xia, H. L. Stormer, D. C. Tsui, C. Vicente, E. D. Adams, N. S. Sullivan, L. N. Pfeiffer, K. W. Baldwin, and K. W. West. Experimental studies of the fractional quantum hall effect in the first excited landau level. *Physical Review B*, 77(7):075307, 2008.

[67] JP Eisenstein and HL Stormer. The fractional quantum hall effect. *Science*, 248(4962):1510–1516, 1990.

[68] Horst L Stormer, Daniel C Tsui, and Arthur C Gossard. The fractional quantum hall effect. *Reviews of Modern Physics*, 71(2):298–305, 1999.

[69] R. B. Laughlin. Nobel lecture: Fractional quantization. *Reviews of Modern Physics*, 71:863–874, 1999.

[70] Horst L. Stormer. Nobel lecture: The fractional quantum hall effect. *Reviews of Modern Physics*, 71:875–889, 1999.

[71] Daniel C. Tsui. Nobel lecture: Interplay of disorder and interaction in two-dimensional electron gas in intense magnetic fields. *Reviews of Modern Physics*, 71:891–895, 1999.

[72] J. K. Jain. Composite-fermion approach for the fractional quantum hall effect. *Physical Review Letters*, 63(2):199–202, 1989.

[73] B. I. Halperin, Patrick A. Lee, and Nicholas Read. Theory of the half-filled landau level. *Physical Review B*, 47:7312–7343, 1993.

[74] W Pan, H. L. Stormer, D. C. Tsui, L. N. Pfeiffer, K. W. Baldwin, and K Wr West. Fractional quantum hall effect of composite fermions. *Physical Review Letters*, 90(1):16801, 2003.

[75] K. Park, V. Melik-Alaverdian, N. E. Bonesteel, and J. K. Jain. Possibility of p-wave pairing of composite fermions at $\nu=\frac{1}{2}$. *Physical Review B*, 58:R10167–R10170, 1998.

[76] Vivek Venkatachalam, Amir Yacoby, Loren Pfeiffer, and Ken West. Local charge of the nu=5/2 fractional quantum hall state. *Nature*, 469(7329):6, 2010.

[77] V. Umansky A. Stern M. Dolev, M. Heiblum and D. Mahalu. Observation of a quarter of an electron charge at the $\nu = 5/2$ quantum hall state. *Nature*, 452(7189):829–834, 2008.

[78] Iuliana P. Radu, J. B. Miller, C. M. Marcus, M. A. Kastner, L. N. Pfeiffer, and K. W. West. Quasi-particle properties from tunneling in the v = 5/2 fractional quantum hall state. *Science*, 320(5878):899–902, 2008.

[79] M. Dolev, Y. Gross, Y. C. Chung, M. Heiblum, V. Umansky, and D. Mahalu. Dependence of the tunneling quasiparticle charge determined via shot noise measurements on the tunneling barrier and energetics. *Physical Review B*, 81(16):161303, 2010.

[80] R. L. Willett, L. N. Pfeiffer, and K. W. West. Measurement of filling factor 5/2 quasiparticle interference with observation of charge e/4 and e/2 period oscillations. *Proceedings of the National Academy of Sciences*, 106(22):8853–8858, 2009.

[81] R. L. Willett, L. N. Pfeiffer, and K. W. West. Alternation and interchange of e/4 and e/2 period interference oscillations as evidence for filling factor 5/2 non-Abelian quasiparticles. *arXiv:0911.0345*, 2009.

[82] Aveek Bid, Nissim Ofek, Hiroyuki Inoue, Moty Heiblum, Charles Kane, Vladimir Umansky, and Diana Mahalu. Observation of neutral modes in the fractional quantum hall regime. *Nature*, 466(7306):585–590, 2010.

[83] M. Milovanović and N. Read. Edge excitations of paired fractional quantum hall states. *Physical Review B*, 53(20):13559–13582, 1996.

[84] B. J. Overbosch and X.-G. Wen. Phase transitions on the edge of the \nu=5/2 Pfaffian and anti-Pfaffian quantum Hall state. *arXiv:0804.2087*, 2008.

[85] Trevor D. Rhone, Jun Yan, Yann Gallais, Aron Pinczuk, Loren Pfeiffer, and Ken West. Rapid collapse of spin waves in nonuniform phases of the second landau level. *Physical Review Letters*, 106(19):196805, 2011.

[86] M. Stern, P. Plochocka, V. Umansky, D. K. Maude, M. Potemski, and I. Bar-Joseph. Optical probing of the spin polarization of the $\nu = 5/2$ quantum hall state. *Physical Review Letters*, 105(9):096801, 2010.

[87] Michael A Nielsen and Isaac L Chuang. *Quantum computation and quantum information*. Cambridge university press, 2010.

[88] David P. DiVincenzo. The physical implementation of quantum computation. *Fortschritte der Physik*, 48(9-11):771–783, 2000.

[89] Peter W Shor. Proceedings of the 35th annual symposium on the foundations of computer science. *arXiv:quant-ph/9508027*, 1994.

[90] J. Preskill. Lecture notes for physics 219: Quantum computation, 2004. http://www.theory.caltech.edu/preskill/ph219/ph219_2004.html.

[91] Emanuel Knill, Raymond Laflamme, and Wojciech H Zurek. Resilient quantum computation: error models and thresholds. *Proceedings of the Royal Society of London. Series A: Mathematical, Physical and Engineering Sciences*, 454(1969):365–384, 1998.

[92] EH Rezayi and N Read. Non-abelian quantized hall states of electrons at filling factors 12/5 and 13/5 in the first excited landau level. *Physical Review B*, 79(7):075306, 2009.

[93] V. Mourik, K. Zuo, S. M. Frolov, S. R. Plissard, E. P. A. M. Bakkers, and L. P. Kouwenhoven. Signatures of majorana fermions in hybrid superconductor-semiconductor nanowire devices. *Science*, 336(6084):1003–1007, 2012.

[94] Masatoshi Sato, Yoshiro Takahashi, and Satoshi Fujimoto. Non-abelian topological order in s-wave superfluids of ultracold fermionic atoms. *Physical Review Letters*, 103:020401, 2009.

[95] Sankar Das Sarma, Chetan Nayak, and Sumanta Tewari. Proposal to stabilize and detect half-quantum vortices in strontium ruthenate thin films: Non-abelian braiding statistics of vortices in a $p_x + ip_y$ superconductor. *Physical Review B*, 73:220502, 2006.

[96] Sumanta Tewari, S. Das Sarma, Chetan Nayak, Chuanwei Zhang, and P. Zoller. Quantum computation using vortices and majorana zero modes of a $p_x + ip_y$ superfluid of fermionic cold atoms. *Physical Review Letters*, 98:010506, 2007.

[97] Benoit Douçot, Lev B. Ioffe, and Julien Vidal. Discrete non-abelian gauge theories in josephson-junction arrays and quantum computation. *Physical Review B*, 69:214501, 2004.

[98] Yaacov E Kraus, Yoav Lahini, Zohar Ringel, Mor Verbin, and Oded Zilberberg. Topological states and adiabatic pumping in quasicrystals. *Physical Review Letters*, 109(10):106402, 2012.

[99] J. Bellissard, A. van Elst, and H. Schulz-Baldes. The noncommutative geometry of the quantum Hall effect. *Journal of Mathematical Physics*, 35:5373–5451, 1994.

[100] B Kramer and A MacKinnon. Localization: theory and experiment. *Reports on Progress in Physics*, 56(12):1469–1564, 1993.

[101] A Saul, A M Llois, and M Weissmann. Wavefunctions of one-dimensional incommensurate hamiltonians: the fractal dimension and its relationship with localisation. *Journal of Physics C: Solid State Physics*, 21(11):2137–2151, 1988.

[102] P G Harper. Single band motion of conduction electrons in a uniform magnetic field. *Proceedings of the Physical Society. Section A*, 68(10):874, 1955.

[103] Douglas R. Hofstadter. Energy levels and wave functions of bloch electrons in rational and irrational magnetic fields. *Physical Review B*, 14(6):2239–2249, 1976.

[104] J. Biddle, B. Wang, Jr. D. J. Priour, and S. Das Sarma. Localization in one-dimensional incommensurate lattices beyond the aubry-andr[e-acute] model. *Physical Review A*, 80(2):021603(R), 2009.

[105] J. Biddle and S. Das Sarma. Predicted mobility edges in one-dimensional incommensurate optical lattices: An exactly solvable model of anderson localization. *Physical Review Letters*, 104(7):070601, 2010.

[106] J Biddle, DJ Priour Jr, B Wang, and S Das Sarma. Localization in one-dimensional lattices with non-nearest-neighbor hopping: Generalized anderson and aubry-andré models. *Physical Review B*, 83(7):075105, 2011.

[107] D J Thouless. A relation between the density of states and range of localization for one dimensional random systems. *Journal of Physics C: Solid State Physics*, 5(1):77, 1972.

[108] Gregory H. Wannier. The structure of electronic excitation levels in insulating crystals. *Physical Review*, 52(3):191–197, 1937.

[109] W. Kohn. Analytic properties of bloch waves and wannier functions. *Physical Review*, 115(4):809–821, 1959.

[110] H.A. Kramers. Das eigenwertproblem im eindimensionalen periodischen kraftfelde. *Physica*, 2(1-12):483 – 490, 1935.

[111] Milton Abramowitz and Irene A. Stegun. *Handbook of Mathematical Functions with Formulas, Graphs, and Mathematical Tables*. Dover, New York, ninth dover printing, tenth gpo printing edition, 1964.

[112] J. Biddle and S. Das Sarma. *unpublished*.

[113] Hideo Aoki. The quantum hall effect in anomalous band structures. *Surface Science*, 263(13):137 – 140, 1992.

[114] E. Prodan. Disordered topological insulators: a non-commutative geometry perspective. *Journal of Physics A Mathematical General*, 44(11):113001, 2011.

[115] A. H. MacDonald. Introduction to the Physics of the Quantum Hall Regime. *arXiv:cond-mat/9410047*, 1994.

[116] F. D. M. Haldane. Fractional quantization of the hall effect: A hierarchy of incompressible quantum fluid states. *Physical Review Letters*, 51(7):605–608, 1983.

[117] G. Fano, F. Ortolani, and E. Colombo. Configuration-interaction calculations on the fractional quantum hall effect. *Physical Review B*, 34(4):2670–2680, 1986.

[118] Tai Tsun Wu and Chen Ning Yang. Concept of nonintegrable phase factors and global formulation of gauge fields. *Physical Review D*, 12(12):3845–3857, 1975.

[119] Tai Tsun Wu and Chen Ning Yang. Dirac monopole without strings: monopole harmonics. *Nuclear Physics B*, 107(3):365–380, 1976.

[120] Tai Tsun Wu and Chen Ning Yang. Some properties of monopole harmonics. *Physical Review D*, 16(4):1018, 1977.

[121] Jun John Sakurai, San-Fu Tuan, and Eugene D Commins. Modern quantum mechanics. *American Journal of Physics*, 63:93, 1995.

[122] N. d'Ambrumenil and R. Morf. Hierarchical classification of fractional quantum hall states. *Physical Review B*, 40:6108–6119, 1989.

[123] Martin Greiter, Xiao-Gang Wen, and Frank Wilczek. Paired hall state at half filling. *Physical Review Letters*, 66(24):3205–3208, 1991.

[124] Tsuneya Ando, Alan B. Fowler, and Frank Stern. Electronic properties of two-dimensional systems. *Reviews of Modern Physics*, 54(2):437–672, 1982.

[125] Frank Stern and Sankar Das Sarma. Electron energy levels in GaAs-$Ga_{1-x}Al_xAs$ heterojunctions. *Physical Review B*, 30(2):840–848, 1984.

[126] S. Das Sarma and B. A. Mason. Optical phonon interaction effects in layered semiconductor structures. *Annals of Physics*, 163(1):78 – 119, 1985.

[127] F. C. Zhang and S. Das Sarma. Excitation gap in the fractional quantum hall effect: Finite layer thickness corrections. *Physical Review B*, 33(4):2903–2905, 1986.

[128] Michael. R. Peterson, Th. Jolicoeur, and S. Das Sarma. Finite-layer thickness stabilizes the pfaffian state for the 5/2 fractional quantum hall effect: Wave function overlap and topological degeneracy. *Physical Review Letters*, 101(1):016807, 2008.

[129] Michael R. Peterson, Th. Jolicoeur, and S. Das Sarma. Orbital landau level dependence of the fractional quantum hall effect in quasi-two-dimensional electron layers: Finite-thickness effects. *Physical Review B*, 78(15):155308, 2008.

[130] R De-Picciotto, M Reznikov, M Heiblum, V Umansky, G Bunin, and D Mahalu. Direct observation of a fractional charge. *Nature*, 389(6647):162–164, 1997.

[131] Jens Martin, Shahal Ilani, Basile Verdene, Jurgen Smet, Vladimir Umansky, Diana Mahalu, Dieter Schuh, Gerhard Abstreiter, and Amir Yacoby. Localization of fractionally charged quasi-particles. *Science*, 305(5686):980–983, 2004.

[132] F. E. Camino, Wei Zhou, and V. J. Goldman. Realization of a laughlin quasiparticle interferometer: Observation of fractional statistics. *Physical Review B*, 72:075342, 2005.

[133] R. H. Morf. Transition from quantum hall to compressible states in the second landau level: New light on the $\nu = 5/2$ enigma. *Physical Review Letters*, 80(7):1505–1508, 1998.

[134] Steven H. Simon, E. H. Rezayi, N. R. Cooper, and I. Berdnikov. Construction of a paired wave function for spinless electrons at filling fraction $\nu = 2?5$. *Physical Review B*, 75(7):075317, 2007.

[135] N. Regnault, B. A. Bernevig, and F. D. M. Haldane. Topological entanglement and clustering of jain hierarchy states. *Physical Review Letters*, 103(1):016801, 2009.

[136] Martin B. Plenio and S. Virmani. An introduction to entanglement measures. *Quantum Information and Computation*, 7:1, 2007.

[137] Luigi Amico, Rosario Fazio, Andreas Osterloh, and Vlatko Vedral. Entanglement in many-body systems. *Reviews of Modern Physics*, 80(2):517–576, 2008.

[138] J. Eisert, M. Cramer, and M. B. Plenio. Colloquium: Area laws for the entanglement entropy. *Reviews of Modern Physics*, 82(1):277–306, 2010.

[139] Alexei Kitaev and John Preskill. Topological entanglement entropy. *Physical Review Letters*, 96(11):110404, 2006.

[140] Michael Levin and Xiao-Gang Wen. Detecting topological order in a ground state wave function. *Physical Review Letters*, 96(11):110405, 2006.

[141] J. Biddle, Michael R. Peterson, and S. Das Sarma. Entanglement measures for quasi-two-dimensional fractional quantum hall states. *Physical Review B*, 84:125141, 2011.

[142] Michael Levin, Bertrand I. Halperin, and Bernd Rosenow. Particle-hole symmetry and the pfaffian state. *Physical Review Letters*, 99(23):236806, 2007.

[143] O. S. Zozulya, M. Haque, K. Schoutens, and E. H. Rezayi. Bipartite entanglement entropy in fractional quantum hall states. *Physical Review B*, 76(12):125310, 2007.

[144] B. A. Friedman and G. C. Levine. Topological entropy of realistic quantum hall wave functions. *Physical Review B*, 78(3):035320, 2008.

[145] B. A. Friedman and G. C. Levine. *International Journal of Modern Physics B*, 24:4707, 2010.

[146] N. Read and E. Rezayi. Beyond paired quantum hall states: Parafermions and incompressible states in the first excited landau level. *Physical Review B*, 59(12):8084–8092, 1999.

[147] Hui Li and F. D. M. Haldane. Entanglement spectrum as a generalization of entanglement entropy: Identification of topological order in non-abelian fractional quantum hall effect states. *Physical Review Letters*, 101(1):010504, 2008.

[148] M. Hermanns, A. Chandran, N. Regnault, and B. A. Bernevig. Haldane Statistics in the Finite Size Entanglement Spectra of Laughlin States. *arXiv:1009.4199*, 2010.

[149] A. Chandran, M. Hermanns, N. Regnault, and B. A. Bernevig. Bulk-Edge Correspondence in the Entanglement Spectra. *arXiv:1102.2218*, 2011.

[150] Jize Zhao, D. N. Sheng, and F. D. M. Haldane. Fractional quantum hall states at 1/3 and 5/2 filling: Density-matrix renormalization group calculations. *Physical Review B*, 83(19):195135, 2011.

[151] A. Sterdyniak, N. Regnault, and B. A. Bernevig. Extracting excitations from model state entanglement. *Physical Review Letters*, 106(10):100405, 2011.

[152] Z. Papić, B. A. Bernevig, and N. Regnault. Topological entanglement in abelian and non-abelian excitation eigenstates. *Physical Review Letters*, 106(5):056801, 2011.

[153] X.-L. Qi, H. Katsura, and A. W. W. Ludwig. General Relationship Between the Entanglement Spectrum and the Edge State Spectrum of Topological Quantum States. *arXiv:1103.5437*, 2011.

[154] F. D. M. Haldane. "fractional statistics" in arbitrary dimensions: A generalization of the pauli principle. *Physical Review Letters*, 67:937–940, 1991.

[155] R. Thomale, A. Sterdyniak, N. Regnault, and B. Andrei Bernevig. Entanglement gap and a new principle of adiabatic continuity. *Physical Review Letters*, 104(18):180502, 2010.

[156] A. H. MacDonald and G. C. Aers. Inversion-layer width, electron-electron interactions, and the fractional quantum hall effect. *Physical Review B*, 29(10):5976–5978, 1984.

[157] Parsa Bonderson and J. K. Slingerland. Fractional quantum hall hierarchy and the second landau level. *Physical Review B*, 78(12):125323, 2008.

[158] Csaba Töke, Michael R. Peterson, Gun Sang Jeon, and Jainendra K. Jain. Fractional quantum hall effect in the second landau level: The importance of inter-composite-fermion interaction. *Physical Review B*, 72(12):125315, 2005.

[159] E. H. Rezayi and F. D. M. Haldane. Incompressible paired hall state, stripe order, and the composite fermion liquid phase in half-filled landau levels. *Physical Review Letters*, 84(20):4685–4688, 2000.

[160] Andreas M. Läuchli, Emil J. Bergholtz, Juha Suorsa, and Masudul Haque. Disentangling entanglement spectra of fractional quantum hall states on torus geometries. *Physical Review Letters*, 104(15):156404, 2010.

[161] Andreas M Läuchli, Emil J Bergholtz, and Masudul Haque. Entanglement scaling of fractional quantum hall states through geometric deformations. *New Journal of Physics*, 12(7):075004, 2010.

[162] B. Andrei Bernevig and F. D. M. Haldane. Model fractional quantum hall states and jack polynomials. *Physical Review Letters*, 100(24):246802, 2008.

[163] Song He, F. C. Zhang, X. C. Xie, and S. Das Sarma. Destruction of fractional quantum hall effect in thick systems. *Physical Review B*, 42(17):11376–11379, 1990.

[164] A. M. Turner, Y. Zhang, and A. Vishwanath. Band Topology of Insulators via the Entanglement Spectrum. *arXiv:0909.3119*, 2009.

[165] M. Storni, R. H. Morf, and S. Das Sarma. Fractional quantum hall state at $\nu = \frac{5}{2}$ and the moore-read pfaffian. *Physical Review Letters*, 104(7):076803, 2010.

[166] A. E. Feiguin, E. Rezayi, C. Nayak, and S. Das Sarma. Density matrix renormalization group study of incompressible fractional quantum hall states. *Physical Review Letters*, 100(16):166803, 2008.

[167] J. P. Eisenstein, R. Willett, H. L. Stormer, D. C. Tsui, A. C. Gossard, and J. H. English. Collapse of the even-denominator fractional quantum hall effect in tilted fields. *Physical Review Letters*, 61:997–1000, 1988.

[168] Ivailo Dimov, Bertrand I. Halperin, and Chetan Nayak. Spin order in paired quantum hall states. *Physical Review Letters*, 100:126804, 2008.

[169] A. E. Feiguin, E. Rezayi, Kun Yang, C. Nayak, and S. Das Sarma. Spin polarization of the $\nu = 5/2$ quantum hall state. *Physical Review B*, 79:115322, 2009.

[170] E. H. Rezayi and F. D. M. Haldane. Incompressible paired hall state, stripe order, and the composite fermion liquid phase in half-filled landau levels. *Physical Review Letters*, 84:4685–4688, 2000.

[171] Guangtong Liu, Chi Zhang, D. C. Tsui, Ivan Knez, Aaron Levine, R. R. Du, L. N. Pfeiffer, and K. W. West. Enhancement of the $\nu = 5/2$ fractional quantum hall state in a small in-plane magnetic field. *Physical Review Letters*, 108:196805, 2012.

[172] L. Tiemann, G. Gamez, N. Kumada, and K. Muraki. Unraveling the spin polarization of the $\nu = 5/2$ fractional quantum hall state. *Science*, 335(6070):828–831, 2012.

[173] M. Stern, B. A. Piot, Y. Vardi, V. Umansky, P. Plochocka, D. K. Maude, and I. Bar-Joseph. Nmr probing of the spin polarization of the $\nu = 5/2$ quantum hall state. *Physical Review Letters*, 108:066810, 2012.

[174] M. Stern, P. Plochocka, V. Umansky, D. K. Maude, M. Potemski, and I. Bar-Joseph. Optical probing of the spin polarization of the $\nu = 5/2$ quantum hall state. *Physical Review Letters*, 105:096801, 2010.

[175] Jainendra K. Jain. The 5/2 enigma in a spin? *Physics*, 3:71, 2010.

[176] Arkadiusz Wójs, Gunnar Möller, Steven H. Simon, and Nigel R. Cooper. Skyrmions in the moore-read state at $\nu = \frac{5}{2}$. *Physical Review Letters*, 104:086801, 2010.

[177] S. Das Sarma, G. Gervais, and Xiaoqing Zhou. Energy gap and spin polarization in the 5/2 fractional quantum hall effect. *Physical Review B*, 82:115330, 2010.

[178] B.I. Halperin. Theory of the quantized Hall conductance. *Helv.Phys.Acta*, 56:75–102, 1983.

[179] V. W. Scarola, C. May, M. R. Peterson, and M. Troyer. Subband engineering even-denominator quantum hall states. *Physical Review B*, 82:121304, 2010.

[180] J. Biddle, M. R. Peterson, and S. Das Sarma. Variational Monte Carlo study of spin polarization stability of fractional quantum Hall states against realistic effects in half-filled Landau levels. *arXiv:1304.1174*, 2013.

[181] V. W. Scarola, Kwon Park, and J. K. Jain. Excitonic collapse of higher landau level fractional quantum hall effect. *Physical Review B*, 62:R16259–R16262, 2000.

[182] Csaba Töke, Michael R. Peterson, Gun Sang Jeon, and Jainendra K. Jain. Fractional quantum hall effect in the second landau level: The importance of inter-composite-fermion interaction. *Physical Review B*, 72:125315, 2005.

[183] Xiao-Gang Wen. Topological orders and edge excitations in fractional quantum hall states. *Advances in Physics*, 44(5):405–473, 1995.

[184] F. D. M. Haldane and E. H. Rezayi. Spin-singlet wave function for the half-integral quantum hall effect. *Physical Review Letters*, 60:956–959, 1988.

[185] R. L. Willett, R. R. Ruel, K. W. West, and L. N. Pfeiffer. Experimental demonstration of a fermi surface at one-half filling of the lowest landau level. *Physical Review Letters*, 71:3846–3849, 1993.

[186] M. R. Peterson and C. Nayak. More Realistic Hamiltonians for the Fractional Quantum Hall Regime in GaAs and Graphene. *arXiv:1303.1541*, 2013.

[187] S. An, P. Jiang, H. Choi, W. Kang, S. H. Simon, L. N. Pfeiffer, K. W. West, and K. W. Baldwin. Braiding of Abelian and Non-Abelian Anyons in the Fractional Quantum Hall Effect. *arXiv:1112.3400*, 2011.